Investigation of Optical Properties in InAs/GaAs Coupled Quantum Dots

Shohgo YAMAUCHI

February 2007

Investigation of Optical Properties in InAs/GaAs Coupled Quantum Dots

Shohgo YAMAUCHI

Submitted to the Graduate School of
Pure and Applied Sciences
in Partial Fulfillment of the Requirements
for the Degree of Doctor of Philosophy in
Science

at the
University of Tsukuba

数理物質科学研究科審査　博士論文概要

氏　　名　山内　掌吾

学 位 名　博士(理学)

論文題目

Investigation of Optical Properties in InAs/GaAs Coupled Quantum Dots

(InAs/GaAs 結合量子ドットの光物性研究)

論文審査委員:

主査:

筑波大学	物理学系	舛本　泰章	教授

副査:

筑波大学	物理学系	野村　晋太郎	助教授
筑波大学	物理学系	白石　賢二	助教授
筑波大学	物理工学系	浅川　潔	教授
筑波大学	物理工学系	服部　利明	助教授
産業技術総合研究所	光技術研究部門	小森　和弘	グループリーダー

【論文概要】

量子ドットとは電子・正孔あるいはそれらの複合体である励起子の Bohr 半径に対して数分の一から数倍程度の大きさを持つ nm サイズの微結晶である。量子ドットでは0次元的な量子閉じ込め効果によって、キャリアはその運動が全方位で自由度を奪われ、原子様の離散化した固有状態を採る。この固有状態がもたらす特異な状態密度分布を利用して、量子ドットレーザー等の量子ドット集合体デバイスがこれまで活発に研究されてきた。最近では、単一量子ドットが量子状態の単一性を保持し得る事から、量子力学的重ね合わせや量子もつれ合い(エンタングル)を利用する量子情報処理デバイスの媒体として注目を集めるようになった。単一量子ドット中のキャリアが単一量子状態を採り、それを人為的に制御し得る事がこれまでに報告されてきたが、一方で量子情報処理、特に量子演算で不可欠と考えられている複数の量子ドットを近接させた結合量子ドット系の物性理解は未だ不十分である。

本研究では、この結合量子ドット系における電子状態と量子ドット間相互作用の理解を得る事に主眼を置いている。そこで本研究では、先ず結合量子ドット構造の試料作製技術から検討を行い、単一結合量子ドット観測に堪え得る良好な結合量子ドット構造を実現した。作製された試料を用いて、初めに非共鳴結合量子ドット集合体のキャリアトンネル過程を観測した。続いて、単一結合量子ドットの電子状態観測を行い、それを基に、強結合量子ドット、中間結合量子ドット、弱結合量子ドットの各結合

系におけるドット間相互作用の観測を行った。

＜量子ドットの結晶成長＞

本論文第4章では量子ドットの結晶成長について述べている。作製した量子ドットは分子線エピタキシー（MBE）結晶成長技術を用いた自己組織化InAs/GaAs 量子ドットである。

自己組織化量子ドットは格子ミスマッチによる歪をその形成起源としている。4-3節では、母材結晶の歪を利用した位置制御量子ドット成長の可能性を示した。GaAs結晶歪上に整列成長したInAs量子ドットの光学特性を評価し、この量子ドットが従来成長法によるドットと同等な結晶品質を担持している事を明らかにした。

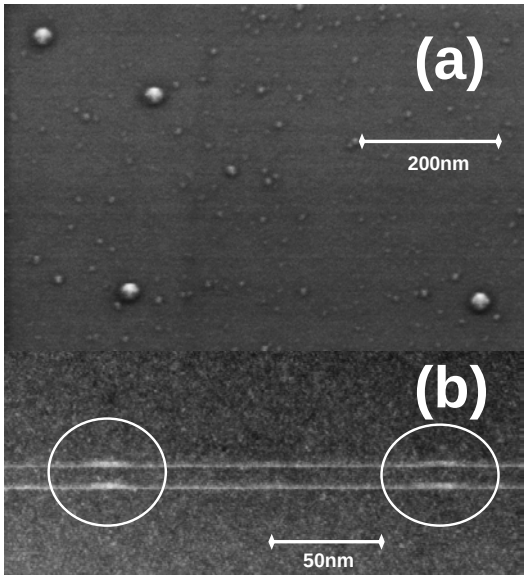

(a) 量子ドットの走査電子顕微鏡写真
(b) 結合量子ドットの断面透過電子顕微鏡写真

結合量子ドット構造の作製には、成長方向に量子ドットを積層させた縦結合量子ドット構造を採用した。そこでは、1層目量子ドットに由来するバリア層内の結晶歪によって2層目量子ドットの整列成長が実現される。4-4節では、InAs 膜厚条件を変える事で1層目/2層目量子ドットのサイズ（発光波長）を制御出来る事を示した。また、Indium-Flush 法を適用する事で狭バリア厚においても良好な結合量子ドット構造が得られる事を示した。

単一結合量子ドットの光物性評価においては、単一の結合量子ドットのみを抜き出して観測出来る様な試料構造を作製する事が重要である。4-1節では、成長基板温度、InAs 成長膜厚を最適化する事で、量子ドットの面内密度と発光波長をほぼ独立に制御出来る事を示し、単一ドット分光に不可欠な低面内ドット密度を実現出来る事を示した。また4-5節では、この低面内密度試料の表面に金属細孔マスクを施す事で、単一ドット分光を可能にする試料を提供出来る事を示した。

＜結合量子ドットの光学特性＞

本論文第5章では、上述の良好な試料を用いて行った光学実験結果を基に、結合量子ドット系の電子状態とドット間相互作用について議論した。

先ず、5-1節では、マクロスコピックな測定によって非共鳴結合量子ドットを集合体として観測し、ドット間の相互作用を議論した。そこには、隣接ドットへの波動関数染み出しによる実効的量子閉じ込め

の減少が存在し、ドット間距離に依存したキャリア移動が観測された。発光時間分解分光法によってドット間のキャリア移動時間を見積もると、発光再結合時間を上回る 1nsec 以上の長いトンネル時間が観測され、フォノン・ボトルネック効果が電子のトンネル移動を抑制している事を指摘した。

量子情報処理素子の実現に際しては、単一の結合量子ドットが持つ電子状態を詳しく調べる必要がある。5-2節では、ドット間距離に依存した単一結合量子ドット系の電子状態について議論した。単一結合ドットの PL スペクトルより、電子の波動関数結合によって結合(X^+)/反結合(X^-)準位が形成され、バリア厚"d"の変化によって量子力学的結合の強さが変化する様子が確認された。また、PLE 測定によって結合量子ドット系の励起状態を観測し、波動関数結合によるX^+/X^-準位間での共有励起準位系列と、正孔の励起状態に起因した個別の励起準位系列が存在する事を明らかにした。これらの結果より、d=3, 5nm 結合ドットを量子力学的結合系、d=7nm 結合ドットを電磁気学的結合系と分類出来る事を指摘した。

5-3節では、5-2節で挙げた結合ドットのうち d=3nm の量子力学的強結合量子ドット系におけるドット間相互作用について議論した。結合(X^+)/反結合(X^-)準位を同時に励起する事によって、X^+/X^-の2つの励起子から成る exciton-molecule 状態(XX^{+-})が形成される事を明らかにした。また、この exciton-molecule 状態の形成に X^+/X^-キャリアが優先的に消費され、励起子分子よりも高い生成率を示す事を明らかにした。

5-4節では、量子力学的結合の残る中間結合量子ドットでのドット間相互作用について述べた。d=5nm 結合量子ドットでは結合(X^+)/反結合(X^-)準位の独立励起が実現される。X^+/X^-準位の同時励起によって、X^+準位の低エネルギー側に新しい発光ピークが出現し、これが5-3節で議論した exciton-molecule 状態である事を示した。この様に、2量子ドット間の量子力学的結合は2つの結合準位から成る exciton-molecule 状態を引き起こす事が明らかと成った。これら exciton-molecule 状態は結合量子ドット系における量子ゲートの可能性を示すものである。

5-5節では、d=7nm 電磁気学的弱結合量子ドットにおけるドット間相互作用について議論した。d=7nm 結合ドットでは量子ドット間のキャリア移動が無視出来る為、2台の励起光源を用いて各ドットを個別/同時に励起が出来る。2波長励起 PL/PLE 実験において、2つのドットへのキャリア同時生成によって発光強度の異常増大効果が観測された。これはドット間の双極子相互作用によってキャリアのエネルギー緩和が促進された為と考えられる。

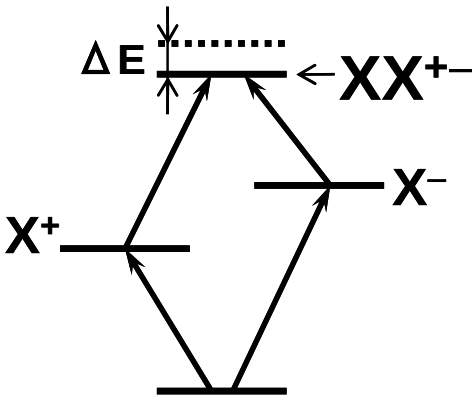

Exciton-molecule(XX^{+-})の形成

最後5-6節では、時間相関光子計数法を用いて d=7nm 結合量子ドットのドット間相互作用をさらに調べた。結合ドットを構成する2つの量子ドットは、単一量子ドットと同様に各々が単一光子を放出している事が確認された。この光子放出過程ではキャリアーフォノン相互作用が重要であり、残留する音響フォノンによってエネルギー緩和が促進される事を明らかにした。2量子ドット間の光子相互相関スペクトルにはアンチバンチング構造が観られ、5-5節で議論した双極子間相互作用によるエネルギー緩和の促進に起因している可能性がある事を示唆した。

以上の様に、本研究では結晶成長・試料加工の最適化による良好な結合量子ドット試料を以って、結合量子ドット系における電子状態とドット間相互作用について議論した。中でも重要な知見として、量子力学的結合が exciton-molecule 状態を引き起こす事を明らかにした。しかし残念ながら、結合ドットの物理が完全に解明された訳では無く、未だ不明な部分が数多く残されている。本論文でも理論的な検討が不十分である事は否めないが、本研究が量子情報処理素子への発展が期待される結合量子ドット系の物性理解に幾ばくかの寄与をし得るものと考える。

具体的なデバイス動作を実現し得る物性の抽出と理解には、さらに多くの様々な角度からの実験データを蓄積する事が必須と考えられる。今後の研究進展に期待する。

Table of Contents

1. Introduction

A quantum dot (QD) is a nanocrystalline particle whose size ranges from a fraction to several times the Bohr radius of an electron, a hole, or an exciton consisting of both an electron and a hole. While nanosized particles have been investigated in various material systems,[1,2] the nominal designation of the "quantum dot" often indicates the semiconductor nanoparticle. A quantum well or wire provides a one- or two-dimensional quantum confinement system for the carriers in crystals; whereas, the QD provides a three-dimensional quantum confinement system (zero-dimensional system) that induces an atomic-like discrete eigenstate.[3,4,5] In the early days of QD investigation for about 20 years, its physical properties were the chief objects of interest.[6] This is because it was considered that the atomic-like eigenstate in a QD, which was artificially controllable, had the potential to provide the platform for verification of quantum mechanical properties. In the latter, an ultralow-threshold laser consisting of QDs was proposed on the basis of the peculiar distribution of state density originating from the zero-dimensional system,[7,8] and subsequently the QD has been under intense study from both fundamental and applied perspectives. While experiments in the early stages made use of nanoparticles segregated in large bandgap materials such as glass matrices and polymers,[3] applied research has been significantly accelerated by the finding that the island-shaped nanocrystal epitaxially grown in the Stranski-Krastanow growth mode comported itself as a QD.[9] In recent years, optical devices with an active layer consisting of QDs are close to practical use. In these devices, the QD laser oscillates at a telecommunication wavelength band of 1.3 μm with high-speed modulation up to 10 GHz and temperature independence of oscillation wavelength.[10] Furthermore, the QD optical amplifier actualized a 40 GHz operation in the 1.55 μm wavelength band.[11]

In other research fields, the demand for the intensification of information processing ability and a secure communication system has recently encouraged investigations of the quantum information processing technology using the quantum mechanical superposition principle and quantum entanglement.[12,13] Both quantum computing and cryptographic transmission essentially require maintaining and controlling a single quantum state [quantum bit (qubit)]. At the same time, a controllable interaction between two qubits, which enables an intended superposition state to be

induced, is needed for the quantum calculation. The nuclear magnetic resonance (NMR) experiment has made unprecedented progress in experimental demonstration of the fundamental principles of quantum computing, in which the basic algorithm of quantum logic operations has already been verified.[14] However, for the future integration of circuits, it is necessary to realize a quantum device with solid state materials. In the quantum cryptographic transmission experiment, a very weak laser pulse had been used as a single photon. However, this is insufficient as a single photon source, because the laser pulse cannot eliminate the probability of including multiple photons in a pulse.[15,16]

The QD has recently attracted more attention than ever as a medium for quantum information processing devices. This is because the atomic-like discrete eigenstate in a QD can be regarded as a two-level system (qubit) that maintains a single quantum state,[17,18] and is expected to easily obtain a single photon from this two-level system, which is utilized as a carrier for quantum information transmission.[19] Based on such a background, the recent interest in QD research has made progress from the application of QD ensembles to the physical properties of a single QD.[20] In previous studies, P. Borri *et al.* suggested that the excitons in QDs have the potential to play a role in qubit, based on the observation of long exciton coherence times up to several hundred picoseconds.[21] It has also been reported that the phase of the transition dipole induced by an exciton is coherently controlled in a single QD,[22,23] and that the population of an exciton is coherently operated by means of Rabi oscillation.[24,25,26,27,28,29,30] Furthermore, the controlled rotation quantum gate between two qubits has been demonstrated using the exciton–biexciton correlation in a single QD.[31] At the same time, the application study of quantum communication has also been developed, in which the single photon emission from a QD has been observed.[32,33,34,35] Thus, QD investigation for quantum information devices has made significant progress. However, there remains a limited understanding of physical properties in a coupled QD (CQD) system, consisting of several adjacent QDs, which has been considered to be essential for the scalability into a large number of qubits and for signal transduction between qubits.[17,36,37,38]

This thesis focuses mainly on understanding the electronic state and interdot interaction in a CQD system. Initially, we consider the fabrication of a CQD structure. In this study, we produced an InAs/GaAs self-organized QD sample by the molecular beam epitaxy (MBE) crystal growth technique. In sample fabrications, the subject for analysis is the optical property of QD ensembles,

which reflect the structural parameters and growth conditions. Next, we present the detailed optical properties of a non-resonant CQD ensemble, in which the coupling effect and carrier tunneling will be discussed. Then, we detail the electronic state and interdot interaction in a single CQD that exhibits different optical properties with a change in the interdot spacing.

Thus, this study makes a meaningful contribution to the understanding of the physical properties of a CQD system which is expected to be applied in quantum information devices.

2. Overview of Quantum Dot

In this chapter, the basic features of a quantum dot are reviewed. The characteristics of actual QDs samples will be presented in chapter 4 or later.

2-1. Electronic Structures in Low-Dimensional Systems

The carrier confinement system is classified according to the allowed energy structure, as is schematically shown in Fig. 2-1.[3] Carriers in a bulk crystal can move uninhibitedly in 3D space, and consequently their density of states $N(E)$ shows a parabolic curve as a function of energy, in which the carriers can take arbitrary energy states continuously (shaded area in the figure). In a quantum well (2D system), the motion of carriers is quantized in a single axial direction, which leads to a step-like function of the state density $N(E)$. In a quantum wire (1D system), the motion of carriers is only allowed in a single axial direction, which causes an reduction of the state density. However, there still remains a continuous energy state in a quantum wire. On the other hand, the QD confines carriers in a zero-dimensional dot, in which they are no longer allowed to move freely in any direction. Accordingly, all carrier motion are quantized, and the allowed eigenstate becomes completely isolated as a δ function (the bottom of Fig. 2-1). This atomic-like discrete eigenstate is the essential characteristic of QDs, which can be applied to a quantum bit with a view to quantum information device applications.[17] Concerning QD ensemble

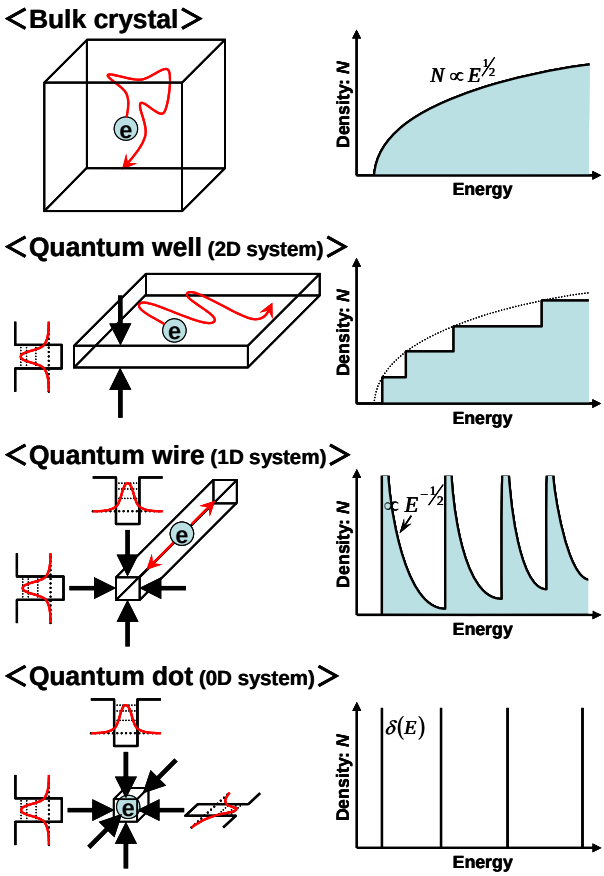

Fig. 2-1. Variation of low-dimensional systems.

devices, we can obtain a large non-linearity and gain derived from the carrier concentration to the lowest excited level.[4]

2-2. Electronic States in Spherical Confinement Potential

As a simple example, let us consider the energy states of a carrier confined in a spherical QD with radius *R*. When we assume infinite potential outside the sphere for simplicity, we only need to consider the following formulae:[39]

$$H = -\frac{\hbar^2}{2m}\nabla^2 + V(r) \qquad \textbf{…Eq. 2-1}$$

$$V(r) = 0\,(r < R),\ V(r) = \infty\,(r > R). \qquad \textbf{…Eq. 2-2}$$

The solution of this equation is a spherical Bessel function. In the boundary condition of $j(kR) = 0$ at $r = R$, the eigenvalue becomes discrete, described as

$$E_{n,l} = \frac{\hbar^2}{2m}\left(\frac{\phi_{n,l}}{R}\right), \qquad \textbf{…Eq. 2-3}$$

where n and l indicate the main and angular momentum quantum number, and $\phi_{n,l}$ is the root of the Bessel function satisfying $j(\phi_{n,l}) = 0$; for example, $\phi_{1,0} = \pi$ (1s state), $\phi_{1,1} = 4.49$ (1p state), and $\phi_{1,2} = 5.76$ (1d state). As seen in this formula, the eigenenergy of carriers in a QD increases with a reduction in the radius *R*, *i.e.*, the quantum confinement becomes stronger with a reduction in the QD size. The electronic state of the actual QDs is far more complex than this model; this is because the potential is finite, deformation and piezo potential arise from the crystal strain, and the QD shape is not spherical.[4] Nevertheless, the carrier energy generally increases with a reduction in QD volume.

2-3. Classifications of Confinement Variations

Another crucial point in a QD is the relationship between QD size and the Bohr radius of the electron and the hole. The effective mass of a hole is, generally, one order of magnitude larger than that of the electron; this indicates a difference in the Bohr radius between electron and hole. Accordingly, the effective strength of quantum confinement differs between electron and hole. In addition, it is necessary to pay attention to the Bohr radius of an exciton, a boundstate of electron and hole, which plays a significant role in the physical properties of QDs. Furthermore, the Bohr

radii of electron and hole vary depending on the material. Therefore, we cannot judge the physical properties only from the QD size. Consequently, the quantum confinement derived from the QD is briefly classified into the following three cases, according to the relative sizes of the Bohr radius of electron, hole, and exciton (a_e , a_h , $a_B = a_e + a_h$) and the QD radius (R) (Fig. 2-2).[3]

(1) Weak Confinement Region ($R > a_B , a_e , a_h$)

The Hamiltonian for electron and hole in the effective mass approximation is given as

$$H_0 = -\frac{\hbar^2}{2m_e^*}\nabla_e^2 - \frac{\hbar^2}{2m_h^*}\nabla_h^2 - \frac{e^2}{\varepsilon\left|r_e - r_h\right|^2}, \quad \text{…Eq. 2-4}$$

and the eigenvalue is given by

$$E_n(k) = E_g - \frac{\mu e^4}{2n^2\hbar^2\varepsilon^2} + \frac{\hbar^2 k^2}{2(m_e + m_h)}, \quad 1/\mu = 1/m_e^* + 1/m_h^*. \quad \text{…Eq. 2-5}$$

Here, E_g indicates the band-gap energy and n indicates the main quantum number of the exciton internal level. In Eq. 2-5, the second term on the right-hand side indicates the binding energy of an electron-hole pair (exciton) arising from the Coulomb interaction (third term in Eq. 2-4), and the third term indicates the translational motion of an exciton in a QD. A weak confinement is the case in which the exciton is regarded as a carrier in a QD. This means that the electron-hole pair can maintain the form of an exciton originating from the condition $R > a_B$. In this confinement region, the translational motion of the exciton is quantized. In other words, this corresponds to the case where the Coulomb interaction in an electron-hole pair is sufficiently larger than the quantum confinement energy of electron and hole individually confined in a QD.

(2) Strong Confinement Region ($R < a_e , a_h$)

On the other hand, in the strong confinement region, where the QD radius is smaller than the Bohr radii of electron and hole, the electron-hole pair can no longer maintain the form of an exciton. In this case, it is reasonable to treat the electron and hole as individually confined in a QD, where the Coulomb interaction between electron and hole is treated as a

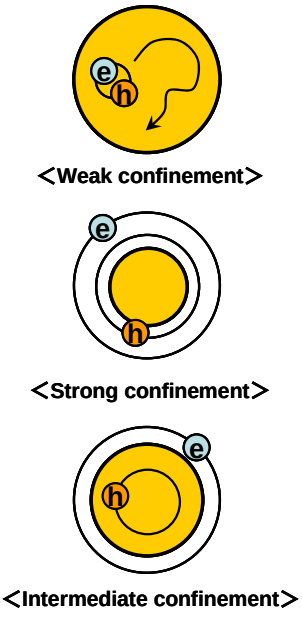

Fig. 2-2. Classification of quantum confinement.

perturbation. In other words, this region corresponds to the case where the confinement energy is sufficiently larger than the Coulomb interaction in an electron-hole pair.

(3) Intermediate Confinement Region ($a_h < R < a_e$)

An intermediate confinement is the medium region between the above two cases. In this region, while the electron is strongly quantized with large confinement energy, the hole does not take a larger confinement energy than the Coulomb interaction energy. This means that the hole is significantly affected by the Coulomb interaction, in contrast to the electron. Most of the III-V compound semiconductors in which the exciton Bohr radius is large and the exciton binding energy is small, fall in this category.

2-4. InAs/GaAs Quantum Dot

The samples used in this study were InAs self-organized QDs grown in a GaAs crystal using the molecular beam epitaxy (MBE) technique. Table 2-1 presents the physical parameters of the InAs and GaAs bulk crystals.[40] The lateral size of QDs is about 20 nm (see Chapter 4), and therefore, the InAs QDs are classified into the intermediate confinement region. Accordingly, in InAs/GaAs QDs, it is expected that the wavefunction of the electron penetrates deeply into the GaAs barrier matrix because of the strong quantum confinement, whereas the wave function of the hole remains almost in the QD crystal because of the weak confinement. In this case, the electron and hole make a pair through the Coulomb interaction, but cannot be called an “exciton” in the strict sense. However, for convenience sake, we describe the electron-hole pair in InAs QDs as an exciton in this thesis.

Many attempts have been made to theoretically calculate the energy states in InAs/GaAs QDs, because of its potential for applications. However, it is very difficult to quantitatively reproduce the actual emission spectra of QDs. This originates from the fact that we are unable to quantitatively estimate the actual QD shape, strain distribution, and mixture of indium and gallium molecules near the QD surface. Diverse calculation methods have been proposed by many research groups; for example, the effective mass approximation,[41,42] the k·p perturbation theory,[43,44] the pseudo-potential theory,[45,46] the tight-binding approximation,[47] and so on. We are not concerned with the detailed theoretical treatment in this thesis. But, based on any method, the energy

difference between the ground level and the 1st excited level of electron and hole can be calculated as 50–100 meV and just over 10 meV, respectively. The difference between the electron and hole energies in these calculations originates from the difference in the effective mass. Although these calculated values approximate to the observed results for the excited level emissions in the QD ensembles,[48,49,50,51,52,53,54,55,56] the luminescence in a single QD has not yet been emulated precisely. At any rate, it may safely be considered in the case of the coupled QD system that the electron can tunnel into the neighboring QD whereas the hole remains in the QD.

On the other hand, the crystal growth technique has revealed that the strain on a QD plays a significant role in defining the energy states in InAs/GaAs QDs. In these, the strain close to the QD boundary surface modulates the confinement potential and results in a change in the energy state in the QD.[57] This will be discussed in detail in Chapter 4.

Table 2-1. Physical parameter in bulk crystal.

		InAs	GaAs
Band gap energy, E_g [eV]		0.418	1.52
Band gap energy, λ_g [nm]		2965	815
Lattice const., a_0 [nm]		0.606	0.565
Effective mass	Electron, m_e*	0.023	0.067
	Heavy hole, m_{hh}*	0.41	0.48
	Light hole, m_{lh}*	0.025	0.087
Bohr radius [nm]	Electron, a_e	35.03	9.89
	Heavy hole, a_{hh}	1.96	1.38
	Light hole, a_{lh}	32.2	7.61
	Exciton, a_B	36.8	11.3
Exciton binding energy [meV]		1	4
LO-phonon [meV]		29.9	36.7
TO-phonon [meV]		27.3	33.8
Refractive index at 1μm, n		3.52	3.35
Dielectric const., ε		15.2	12.5

3. Quantum Information Devices Using Quantum Dot

In this chapter, we outline a quantum information device and discuss the expected configuration of QDs.

3-1. Quantum Computing Devices and Quantum Dot

3-1-1. Quantum Computing

Current information processing technology is based on the Turing machine as typified by the von Neumann-type computer. In this type of computing, information processing is executed by means of reading, writing, and computing the data, which is written on a storage device, in the order of events.[58] Accordingly, in some kinds of arithmetic processing such as data retrieval and factorization, we are forced to operate with a fine-tooth comb on data from the edge of the data set. As a result, the complication of computational problems immediately inflates the calculation amount and the operating time. As a means of solving this problem, quantum computing using the quantum superposition principle has recently attracted attention in the wake of the discovery of the factorization algorithm by P. W. Shor in 1994.[59]

Here, we briefly explain the concept of quantum calculation.[12] The quantum mechanical expression of a particle state at a given time, such as the electron state $|e\rangle$, is derived from the stochastic weighting summation of all allowed states $|0\rangle$, $|1\rangle$, $|2\rangle$…, and is written as $|e\rangle = a|0\rangle+b|1\rangle+c|2\rangle+\ldots$. Here, when each state ($|0\rangle$, $|1\rangle$, $|2\rangle$…) is assigned to the solution candidates for calculation, all solution candidates exist in parallel at that given time. Then, the direct operation of this superposition state enables us to reproduce the intended probability distribution state $|e'\rangle$, and the observation of this quantum state gives us the calculation result. Thus, super parallel computing with quantum calculation is expected to reduce the operation time drastically compared to the conventional calculating method. The bearer of information in quantum computing is a two-level system, the so-called “quantum bit (qubit),” which is capable of maintaining a quantum mechanical property (coherence). Primary investigations of the arithmetic algorithm have revealed that any

quantum calculation can be executed by the combination of one qubit control (unitary transformation) and the gate mechanism (control NOT gate) consisting of two qubits.[60,61]

In concert with this proposal, the study of quantum computing has made rapid progress in experimental work. Any quantum two-level system that is capable of maintaining its coherence can be basically applied to the physical subject for quantum calculation, such as the following proposals: ion trapping by laser cooling technique,[62,63] control of the atom ensemble's spin in liquid solution by nuclear magnetic resonance (NMR),[64,14] nuclear spin of Si isotope,[65] charge qubit,[66] and magnetic flux qubit[67] in the Josephson superconductive circuit, electrical control of an electron in the quantum point contacted QD,[68,69,70,71] and optical control of an exciton in a compound semiconductor QD.[36] In these studies, the NMR method has made unprecedented progress because of the long decoherence time up to 1 s in the system, in which the operating of 7 qubits has already succeeded in factorizing the number 15 in Shor's factorization algorithm scheme.[14] However, in the NMR system, the integration degree is expected to reach a maximum limit of 10 qubits, because the increasing number of qubits gives an exponential reduction in NMR signal. Furthermore, for practical use, it is desirable to realize a quantum device using solid state materials. Among the cited examples, the solid state systems are the Si isotope, the magnetic flux qubit, the charge qubit in a QD, and the exciton in a compound semiconductor QD. The Si isotope application is still under the basic research phase of a single isotopic crystal growth technique. In the magnetic flux qubit system, an easy processing technique in the micrometer order is applied to the fabrication of the devices, but the switching time of the qubit is long (up to a microsecond). The charge qubit system requires ultralow temperature of milliKelvins using the dilution refrigerator to maintain its coherence. On the other hand, the exciton in a compound semiconductor QD makes it possible to perform experiments under liquid helium temperatures, and more importantly, the ultrafast optical technique can be applied to the experiment. In the early stages, it was considered that the fast decoherence time of carriers ruled out the application of quantum computing in this system. However, the recent observations of long coherence times of an exciton in a QD,[21] up to several hundred picoseconds, have convinced us that it is possible to save sufficient time for quantum calculation in QDs using the ultrafast optical technique. Moreover, the latest report has demonstrated that the electron in a InP QD maintains a very long spin coherence time, up to the sub-millisecond range,[72] thus broadening the possibilities of application of this system to quantum

devices.

3-1-2. Control of Quantum Bit

Let us overview the qubit control method. The coherent interaction between a two-level system and an external field is well known as Rabi oscillation.[73]

The time-dependent Schrödinger equation of the two-level system is described as

$$i\hbar\frac{\partial\psi}{\partial t}=H\psi\,, \qquad \textbf{…Eq. 3-1}$$

where the wave function ψ is assumed to satisfy the following equation:

$$\psi_n(r,t)=\phi_n(r)exp(-i\omega_n t),\ H_0\psi_n(r,t)=\varepsilon_n\psi_n(r,t)\ (\omega_n=\varepsilon_n/\hbar). \qquad \textbf{…Eq. 3-2}$$

Here, H_0 is the Hamiltonian without perturbation, the suffix n (=1, 2) indicates a level in the two-level system, ε_n indicates its eigenenergy, and ϕ_n is the time-independent term of the wave function. When the probability amplitudes of two levels are expressed as $a_1(t)$ and $a_2(t)$, the wave function of the two-level system at an arbitrary state is written as

$$\psi(r,t)=a_1(t)\psi_1(r,t)+a_2(t)\psi_2(r,t). \qquad \textbf{…Eq. 3-3}$$

Next, we consider the interaction with an external field. The two-level system is assumed to interact with light through the perturbation as

$$H'(t)=-\mu E(t),\ E(t)=|E|cos\,\omega_0 t\,,\ (\omega_0=\omega_2-\omega_1), \qquad \textbf{…Eq. 3-4}$$

where μ is the transition dipole moment of the two-level system, and ω_0 is the angular frequency of the light equal to the energy separation of the two-level system. Using the revised Hamiltonian $H = H_0 + H'(t)$, from Eqs 3-2 and 3-3, the probability amplitude of level 1 is derived as

$$|a_1(t)|^2=sin^2\frac{\Omega}{2}t\,,\ \Omega=\frac{|\mu E|}{\hbar}. \qquad \textbf{…Eq. 3-5}$$

As can be seen from this expression, the occupation probability of level 1 is conrolled by the coherent interaction with external light (Fig. 3-1). This behavior is called Rabi oscillation, and Ω is called the Rabi frequency. Thus, we can coherently control a single qubit temporally during the time when the external field is induced. This corresponds to the unitary time evolution of the quantum

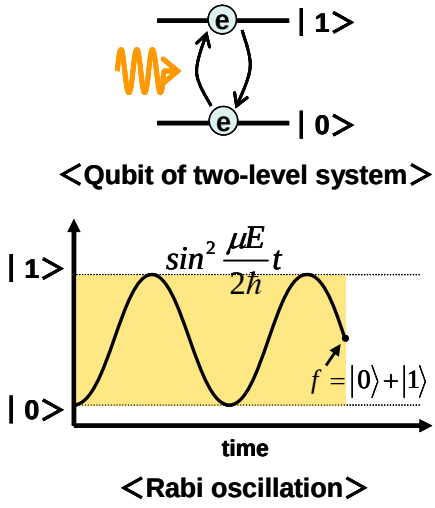

Fig. 3-1. Qubit consisting of two-level system and Rabi oscillation.

state.[12]

The two levels among the discrete electronic states in a QD can be assigned to the above mentioned two-level system. The selected two-level in a QD can be controlled by externally induced light. In fact, the observation of Rabi oscillation in a QD has been reported by a number of research groups.[24,25,26,27,28,29] Additionally, the Rabi oscillation is interpreted as a kind of resonance phenomenon between light and the two-level system producing the resonant energy $\hbar\Omega$. H. Kamada *et al*. observed splitting of the luminescence peak in a single QD arising from this resonant energy $\hbar\Omega$.[30]

3-1-3. Controlled-NOT Gate

The controlled-NOT gate is a quantum gate consisting of two qubits, which corresponds to the XOR gate on the classical calculator. The controlled-NOT gate constitutes the "universal quantum Turing machine" in combination with the unitary transform of 1 qubit. One of the two qubits is called the "control bit" and the other is called the "target bit." The target bit is controlled by the control bit. The operation of the controlled-NOT gate is schematically shown in Fig. 3-2.[12] The left side of the figure is the input port and the right side is the output port. In operation, the control bit of $|0\rangle$ does not influence the target bit state; the control bit of $|1\rangle$ triggers the transition of the state flipping in the target bit (NOT gate operation). When the control bit is given by the superimposed state as $|0\rangle + |1\rangle$, the target bit outputs the entangled state as $|0\rangle|1\rangle + |1\rangle|0\rangle$. The quantum calculation is executed by repeating this operating process. Here, we do not refer to the specific configuration of the quantum circuit because it is beyond the scope of this thesis. The important point is forming the gate device using QDs, which can provide the operation function as shown in Fig. 3-2.

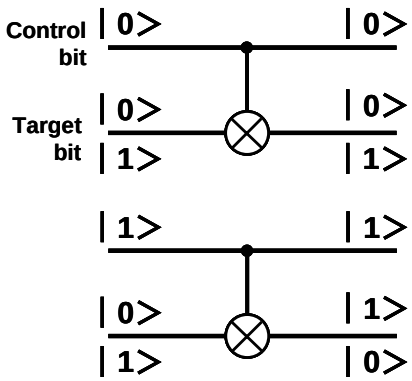

Fig. 3-2. Controlled-NOT gate operation.

3-1-4. Quantum Logic Gate and Quantum Dot

Let us consider the formation of quantum gate by QDs. A. Barenco *et al*. made the first proposal for a quantum gate consisting of QDs,[17] which is schematically shown in Fig. 3-3. Initially, the

system requires two QDs, QD A and B, whose energy levels are different. The qubits (two-level systems) in each QD are composed of ground and excited state electrons, where QD A (B) is assigned to the control (target) bit. We consider the case of a system to which an external electric field is applied. In the case without the electric field, QD A does not interact with QD B; accordingly, the system energy does not change whichever of the states $|0\rangle$ and $|1\rangle$ the electron of QD A exists in. On the other hand, in the case of application of an electric field, the wave functions of the ground and excited states are deformed, which induces the electric dipoles alternately. Consequently, the dipole-dipole interaction between QD A and B changes the system energy with ΔE interaction energy (Fig. 3-3). Here, in the case with the electric field, when we induce the light whose energy corresponds with the separation energy between $|1\rangle_A|0\rangle_B$ and $|1\rangle_A|1\rangle_B$, it causes the Rabi oscillation between $|1\rangle_A|0\rangle_B$ and $|1\rangle_A|1\rangle_B$. In other words, the transition of QD B is only allowed in the case of which QD A takes the $|1\rangle$ state: this means that a controlled-NOT gate has been achieved.

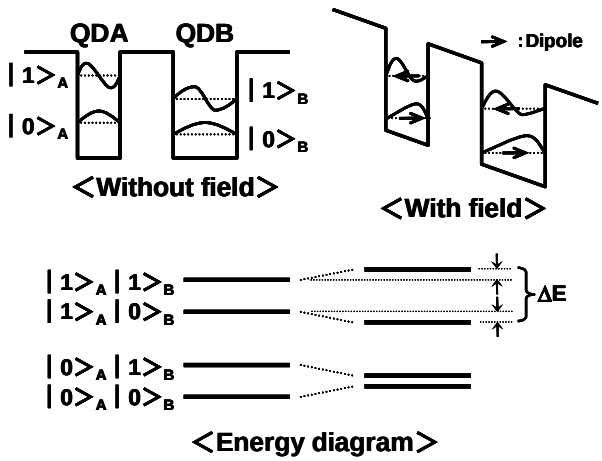

Fig. 3-3. Controlled-NOT gate consisting of QDs proposed by A. Barenco *et al*..

However, in above configuration, the rapid relaxation time in the intraband transition of an electron restricts the operating time. E. Biolatti *et al.* proposed an evolved gate system in which electron-hole pairs (excitons) with longer relaxation times are assigned to qubits (see Fig. 3-4).[36] This system also utilizes the dipole-dipole interaction between exciton dipoles induced by an applied external field. Actually, this kind of QD samples have been experimentally

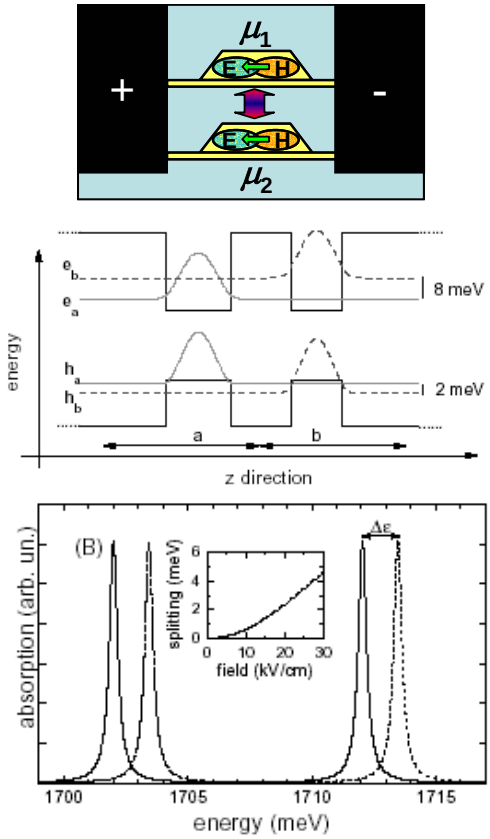

Fig. 3-4. Controlled-NOT gate using excitons in QDs proposed by E. Biolatti *et al*..

investigated,[74, 75, 38] but those efforts have not yet achieved an operating quantum gate.

The first demonstration of a quantum gate using QDs was reported by X. Li *et al.*[31] They focused on two kinds of excitons in a single QD, instead of two QDs. Although this demonstration was not a controlled-NOT gate but a controlled rotation gate, their report was the first to reveal the potential of QDs applied to a quantum gate. Its configuration is presented in Fig. 3-5. The GaAs QD used in their report has two kinds of exciton states with a slight energy separation (|01⟩ and |10⟩), which are individually controlled by selecting the polarization of excitation light (Π_x , Π_y). As shown in the energy diagram in the figure, they utilized the energy shift Δ derived from the formation of the biexciton |11⟩ consisting of |01⟩ and |10⟩ excitons: namely, the signal of biexciton |11⟩ plays the role of monitoring whether the two excitons |01⟩ and |10⟩ exist simultaneously.

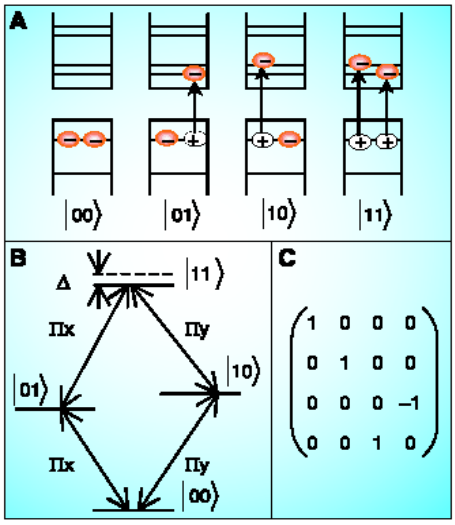

Fig. 3-5. Quantum gate configured by a single QD, reported by X. Li *et al.*.

By the way, this energy configuration does not correspond only to this physical system. For example, as can be seen in E. Biolatti's proposal above, the interaction with ΔE between two QDs makes it possible for us to provide a similar energy configuration (see Fig. 3-6). Moreover, the utilization of two QDs can give us higher controllability of the inter-qubit interaction. This is because we can control the determination factors of the interaction ΔE, the energy levels of excitons, and the distance between excitons, by adjusting the QD size and the interdot spacing. Furthermore, in these coupled QD (CQD) systems, we only need to add another QD to the system for scale up of a quantum circuit, while the single QD system restricts us to use additional qubits because of the limit on the number of excitons in a QD.[76] Thus, the CQD structure is an important physical system with potential to realize adaptable quantum operating devices, and understanding its physical properties

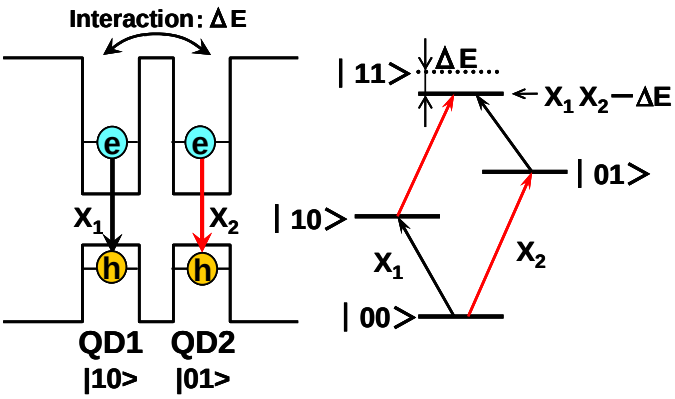

Fig. 3-6. Energy diagram of quantum gate in coupled QD system.

is the main subject of this thesis.

3-1-5. Coupled Quantum Dot

In a CQD system, there is the important consideration of how large an interspace is required between two QDs. This problem can be broken down roughly into two cases according to the kind of interactions used in the operating processes.[18] One is the strong coupling system with a very narrow interdot spacing so that penetration of the carrier wave function into the neighboring QD over the barrier layer induces the quantum mechanical coupling between the two QDs. In this case, the proximity of the two QDs induces the bonding and anti-bonding levels because of the wave function coupling and Pauli exclusion principle, as is the case with the proximity of atoms (see Fig. 3-7). The interaction for the device application is considered to be the quantum mechanical interaction, exchange interaction etc., between bonding levels.

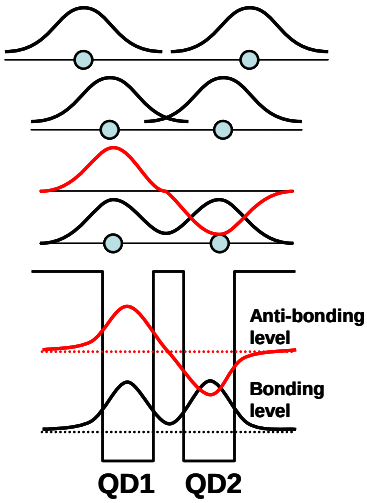

Fig. 3-7. Quantum mechanical coupling.

The other case is the weak coupling system with relatively wide interdot spacing. In this case, the coupling between the wave functions weakens, and consequently, the electromagnetic interaction between QDs becomes dominant instead of the quantum mechanical interaction. For example, the dipole-dipole interaction is supposed to be useful for quantum devices (see Fig. 3-8).

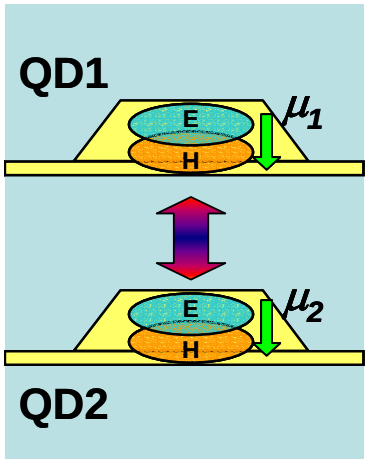

Fig. 3-8. Electromagnetic coupling.

Thus, the coupling mechanism in the CQD system changes with interdot spacing. It should also be noted that the energy difference between the two QDs affects the coupling strength of the wave functions. In this study, we focus on the observation of physical changes in the CQD samples with different interdot spacings.

3-2. Single Photon Emitter and Quantum Dot

In this section, we briefly mention the quantum cryptographic transmission device that plays a

part in quantum information processing, though it departs slightly from the main subject.

3-2-1. Quantum Cryptographic Communications

A quantum cryptographic transmission is a communication method that uses quantum mechanically correlated, "entangled," photon pairs.[13,77,78] The entangled correlation exhibits non-locality and operates remotely. For example, it is assumed that one photon of the photon pair is sent to the recipient and the other remains with the sender. In this quantum transmission, we can check wiretaps on the communication pathway by comparing the photon states between the detected photon with the recipient and the retained photon with the sender. This is because even if the wiretapper steals the sent photon on the transmission path and resends the spurious photon to the recipient, this spurious photon is no longer correlated with the sender's photon. This transmission method ensures secure communication in principle, while the security of conventional communication depends only on the complexity of the decryption code. The transmission of an entangled photon pair had already been demonstrated by the research group of Innsbruck university in 1997, and this transmission method is called "BB-84 protocol."[16] Another proposed method of quantum cryptography transmission, the so-called "Y-00 protocol." uses the quantum fluctuation of a light source,[79,80] but its security remains a matter of discussion. In the following, we outline the entangled photons used in the BB-84 protocol and the applications of QD for the entangled photon emitter device.

3-2-2. Entangled Photon Pair

It is well known that an entangled photon pair can be generated by parametric down-conversion on a non-linear optical crystal such as BBO (BaB_2O_4).[81] The signal and idler beams generated by the parametric down-conversion radiate along separate circular cone edges because of momentum conservation. These cones intersect with each other in the case of an appropriate crystal angle. Both the signal and idler beams can radiate in the direction of the two nodal lines of the intersected cones, where the polarizations of the two beams are orthogonally oriented to each other. Therefore, we cannot distinguish the photon polarization on a single nodal line. In other words, when the photon on nodal line 1 is polarized in the horizontal direction, the photon on nodal line 2 is always polarized in the vertical direction, and vice versa. Mathematically, this is described as

$$f = \frac{1}{\sqrt{2}}\left(\left|H\right\rangle_1\left|V\right\rangle_2 + \left|V\right\rangle_1\left|H\right\rangle_2\right). \quad \textbf{…Eq. 3-6}$$

Each state ($\left|H\right\rangle_1\left|V\right\rangle_2$ or $\left|V\right\rangle_1\left|H\right\rangle_2$) is unknown before the observation, *i.e.*, two photons lie in an "entangled state" with each other. This is one example of the entangled photon pair.

The characteristic of an entangled photon pair is most clearly demonstrated by the Einstein-Podolsky-Rosen (EPR) paradox experiment as shown in Fig. 3-9.[82] The experimental set-up consists of an entangled photon emitter and two polarization detection systems consisting of a polarization beam splitter and two single photon detectors. One photon of the entangled photon pair radiated from the photon emitter is transmitted to detector A, and the other is transmitted to detector B.

Let us consider the case where detector A detects x polarization (detected by A-1) and detector B detects y polarization (detected by B-2), for the first observation (top of Fig. 3-9). In this case, it can be safely deemed that the polarizations of photons have been already decided at the time of radiation from the emitter and the opposite polarization to photon A is observed in photon B. Next, we consider the case where the angles of the detectors are tilted at 45 degrees during the flight of the photons from the emitter to the detectors (middle of the figure). In this case, photon A and B can never anticipate the tilting of the detectors during the flight. But surprisingly, when photon A is detected at A-1, photon B is sure to be detected at B-2 perpendicular to photon A, in spite of the change in detection condition. It looks as if the information on polarization obtained in the detection of photon A was instantaneously transmitted to photon B in a distant place. However, photon A does not interact with photon B, and in any case, the faster transmission of polarization information than the light velocity contradicts the theory of relativity. Thus, the entangled photon pair is a non-local quantum correlation system arising from an entangled state and a reduction in wave packet.

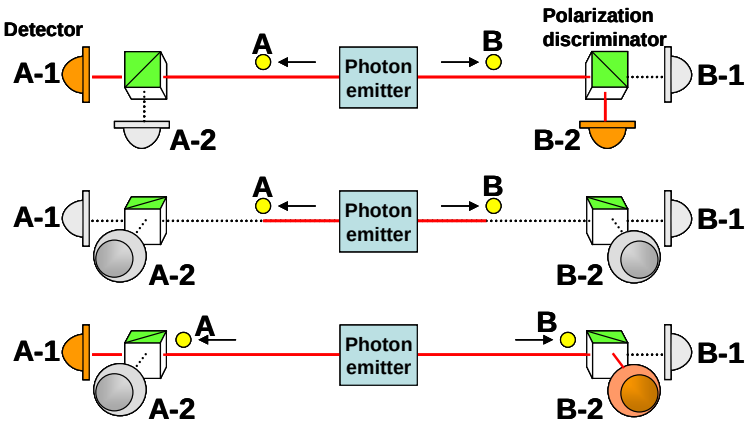

Fig. 3-9. EPR Paradox experiment.

3-2-3. Quantum Dot and Photon Entanglement

A QD provides a completely discrete electronic state; therefore, the number of excitons at the lowest excited level is only one. This suggests the single photon emission in the radiative recombination of the exciton in a QD. Here, we show that a single photon emitter can produce an entangled photon pair.[19]

First, we consider the behavior of a single photon passing through the 50:50 beam splitter. As shown in Fig. 3-10, the incident photon penetrates or is reflected by the beam splitter with a probability of 50%. What happens in the case where two photons are incident onto the beam splitter on both sides? While both photons A and B penetrate or are reflected by the beam splitter even in this case, we can no longer distinguish which photon (A and B) penetrates or is reflected by the beam splitter in the case of simultaneous photon detection on both sides of the splitter. In other words, this is described mathematically as

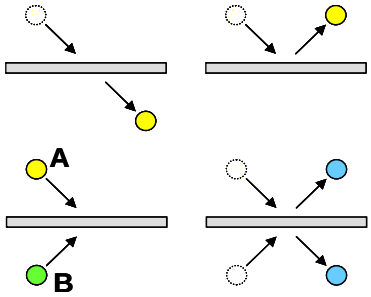

Fig. 3-10. Generation of entangled photon pair by 50:50 mirror.

$$f = \frac{1}{\sqrt{2}}\left(\left|\mathrm{Pen}\right\rangle_A\left|\mathrm{Pen}\right\rangle_B + \left|\mathrm{Ref}\right\rangle_A\left|\mathrm{Ref}\right\rangle_B\right). \quad \textbf{…Eq. 3-7}$$

While photon B must penetrate in the case of photon A penetration and must be reflected in the case of photon A reflection, these two cases cannot be distinguished, and consequently are in an “entangled state” with each other. Thus, we can generate an entangled state from a beam splitter and two photons.

Next, we mention entangled state generation using a single photon emitter.[19] Let us consider the detection of photons 1 and 2 in the system shown in Fig. 3-11, where the two photons are generated from a single photon emitter with time delay τ. These photons are transmitted to Alice and Bob through the 50:50 beam splitter. Alice and Bob detect a photon by means of the single photon detection system with time delay τ. In this system, we consider the case where Alice and Bob simultaneously detect the photons at t = 0. In this case, when Alice detects photon 1, Bob must detect photon 2. This is because the two photons passing through the beam splitter are transmitted to either Alice or Bob. In the present case, photon 1 must pass through the long delay line of Alice’s detector and photon 2 must pass through the short delay line of Bob’s detector. However, Alice can never distinguish which of photon 1 or 2 is detected. This is because the probability that Alice

detects photon 2 through the short delay pass and Bob detects photon 1 through the long delay pass is the same (see the detection sequence in the figure). This situation is described mathematically as

$$f = \frac{1}{\sqrt{2}}\left(\left|1,long\right\rangle_{Alice}\left|2,short\right\rangle_{Bob} + \left|2,short\right\rangle_{Alice}\left|1,long\right\rangle_{Bob}\right), \quad \textbf{…Eq. 3-8}$$

and these two cases are situated in an entangled state with each other. Thus, the single photon emitter enables us to generate an entangled photon pair essential for quantum cryptographic communication, and the QD can be used as a single photon emitter. In fact, there have been many reports of a single photon emitting from a single QD,[32,33,83,84,85] and the transmission of a single photon in a 1.3 μm telecommunication band has been confirmed.[35] Additionally, D. Fattal *et al.* reported the breaking of Bell's inequality using the entangled photon pair generated by a single photon emitted from a single QD.[34] Moreover, the radiation of an entangled photon pair using the exciton/biexciton complex in a single QD has recently been reported.[86]

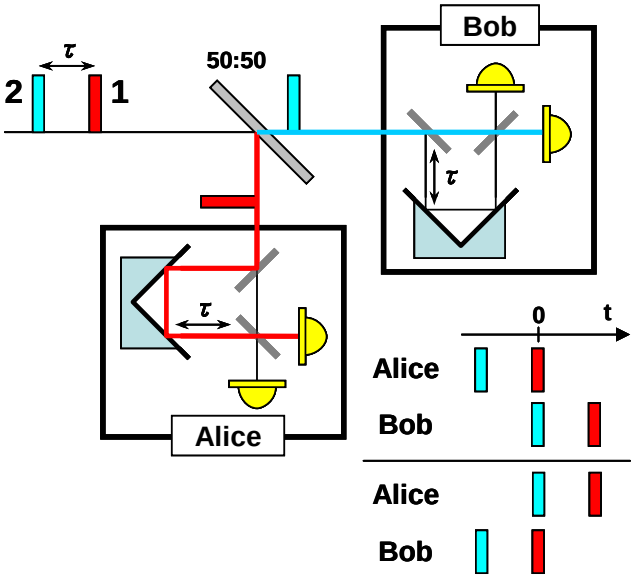

Fig. 3-11. Entangled state generation by using single photon emitter.

4. Quantum Dot Fabrication

In this chapter, the crystal growth of QDs is discussed. Many techniques have been proposed for QD fabrication,[2,4] and these are briefly categorized into top-down-like and bottom-up-like processes. The former is a method of cutting a nanostructure by the fine processing technology for semiconductor devices, and the latter is a method of building up a nanostructure by the self-organization phenomenon. In the top-down process, although the controllability of QD fabrication is comparatively good within the process error range, the error limit is about 50 nm, and more importantly, these processes carry great risks of process damage. In contrast, the bottom-up process can provide a high quality crystal of QDs, which are naturally formed (self-organized) by the fine crystal growth technique, but each QD is grown fortuitously and individually. Therefore, the controllability of the size and location of QDs remains a significant matter for development. There is an intermediate method between the above techniques, in which QDs are fabricated in the crystal structure selectively grown on the patterned substrate,[87] but this method is difficult to apply in the fabrication of a coupled QD (CQD) structure.

Among these alternatives, we employed the epitaxial growth technique of InAs QDs on a GaAs crystal on the basis of the self-organization phenomenon. The InAs/GaAs QD has been the most investigated to date because the time-proven crystal growth technology can be used. In addition, it has the potential to be applied in GaAs based telecommunication optical devices,[10] and more reasonably we can easily obtain a QD structure. The scope of this study is not the pursuit of the growth technique but the estimation of the physical characteristics of CQDs. Therefore, previous knowledge will be used for QD fabrication. The next sections deal with the fabrication of a QD.

4-1. Epitaxial Growth of InAs/GaAs Quantum Dots

4-1-1. Feature of Quantum Dot Growth

It is well known that there are three different growth modes for hetero-epitaxial growth in different materials.[4,88] These are the Frank-van der Merwe（FvdM）, Volmer-Weber（VW）, and Stranski-Krastanow（SK）modes, as shown in Fig. 4-1. The transition between growth modes

depends on the interfacial energy and the difference in lattice constants. In the lattice matching system, when the surface energy of the substrates is more than the summation of the surface and interfacial energies of the growth materials, the FvdM mode is induced. In the opposite energy conditions, the growth makes the transition to the VW mode. In the lattice mismatch system, in the case of low interfacial energy, the SK growth mode is induced. In this mode, the two-dimensional growth initially occurs layer-by-layer, and afterwards, deposition over the critical thickness induces an island-shaped three-dimensional crystal growth, which is caused by the strain relaxation with large lattice mismatch. Here, the first 2D growth layer constitutes an ultrathin quantum well in units of mono layer (ML), which is called "wetting layer (WL) ".

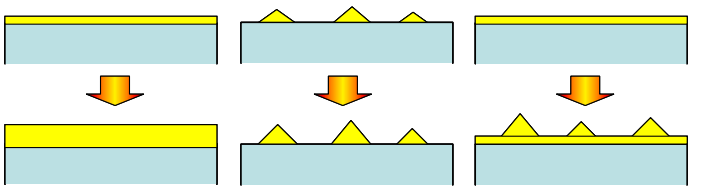

Fig. 4-1. Hetero-epitaxial growth modes.

In the early days, the 3D crystal islands in the SK growth mode were considered as dislocations. But in 1985, L. Goldstein *et al*. reported the beneficial optical properties of the InAs 3D island structure grown on GaAs crystal,[9] and recognized it as a quantum dot. Thus, the growth mechanism of InAs/GaAs self-organized QDs originates from the crystal strain. In addition, the critical thickness is crucially important in the SK growth mode of QDs. Figure 4-2 shows the in-plane QD density as a function of InAs layer thickness reported by R. Heitz *et al*.[89] As seen in the figure, deposition over the critical thickness (~1.6 ML) produces the dramatic transition of growth mode to 3D island growth. Therefore, we must pay careful attention to the deposition thickness in the growth of InAs/GaAs QDs.

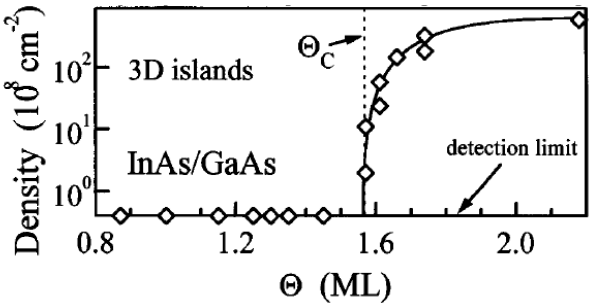

Fig. 4-2. In-plane QD density vs InAs layer thickness, reported by R. Heitz *et al*..

In this study, we employed the molecular beam epitaxy (MBE) technique as the crystal growth method. In MBE growth, the molecules of source materials are directly irradiated and deposited on a substrate crystal in an ultra high vacuum chamber (<10^{-8} Torr). Therefore, high crystal quality with lower impurity content can be obtained as long as a high cleaning level is maintained in the chamber. As an additional characteristic of MBE growth, we can estimate the precise growth rate

and surface conditions by reflection high energy electron diffraction (RHEED).[90]

The actual InAs QD growth depends significantly on the supplied amount of indium molecules and the mean free path of the molecules on the substrate surface. Therefore, the size and in-plane density of QDs is determined by the InAs thickness, the substrate temperature, and the growth rate,[91] as shown in Fig. 4-3. In the case of high substrate temperature, which gives a highly active status to the substrate surface, the supplied indium and arsenic molecules move around on the substrate with long mean free paths. This results in a low in-plane QD density. In contrast, a low substrate temperature leads to short mean free paths, which accelerates QD formation, and accordingly, results in a high in-plane QD density. At the same substrate temperature, a low amount of supplied indium molecules gives a small size QD and a low in-plane density; whereas, a thick InAs layer (high amount of indium molecules) induces a high in-plane density and a large size QD because of the increment of QD formation probability. In addition, the high substrate temperature causes a desorption of indium molecules from the substrate surface, which effectively gives a low amount of deposited indium. Furthermore, the high growth rate, which means high amount of indium molecules per unit time, yields a high in-plane QD density because of the high probability of QD formation per unit time. Thus, the QD growth is a complex mix between InAs thickness, substrate temperature, and the growth rate. In brief, a high substrate temperature can induce a low in-plane density, a low supplied amount of indium molecules can cause a low in-plane density and size reduction in QD, and a low growth rate can give a low in-plane density and size increment of QD.

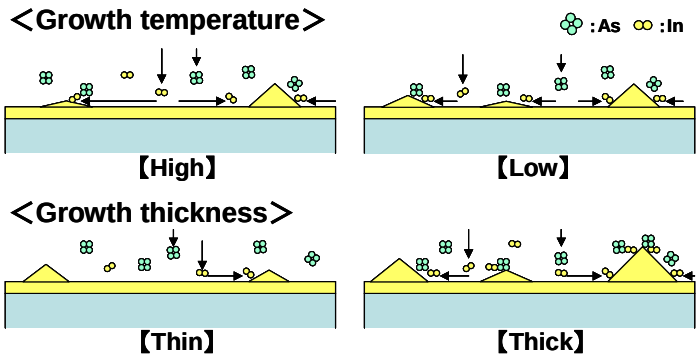

Fig. 4-3. Growth process of InAs QDs. Dependence on growth temperature and thickness.

4-1-2. Practical Examples

Here, we give some practical examples of InAs/GaAs QD growth. Figure 4-4 shows the dependence of InAs/GaAs QD growth on the InAs deposition thickness at a substrate temperature of 590°C, where the InAs thicknesses are 1.7 ML [figure (a)] and 1.6 ML [figure (b)]. The left

figures are the scanning electron microscope (SEM) images of sample surfaces and the right figures present the photoluminescence (PL) spectra of QDs. As seen in the figures, the thin InAs layer induces low in-plane QD density and QD size reduction, which enhances the quantum confinement and results in the blue shift of the PL wavelength (see Section 2-2).

On the other hand, Figure 4-5 presents the dependence of QD growth on substrate temperature at the same InAs thickness of 1.65 ML, and temperatures of 590°C [figure (a)] and 600°C [figure (b)]. As shown in the figure, the higher substrate temperature induces low in-plane QD density. The blue shift of the emission wavelength is considered to originate from the QD size reduction due to the re-evaporation of indium molecules. Thus, the optimization of growth conditions enables us to control the in-plane density and the emission wavelength of QDs (QD size).

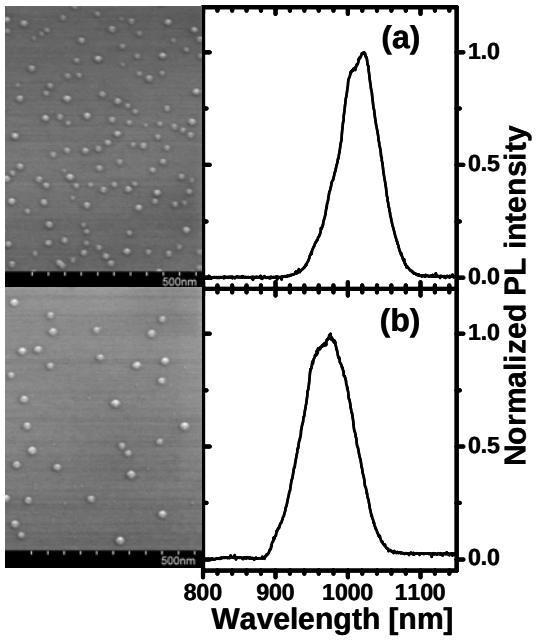

Fig. 4-4. InAs/GaAs QDs growth depending on deposition thickness: (a) 1.7 ML, (b) 1.6 ML.

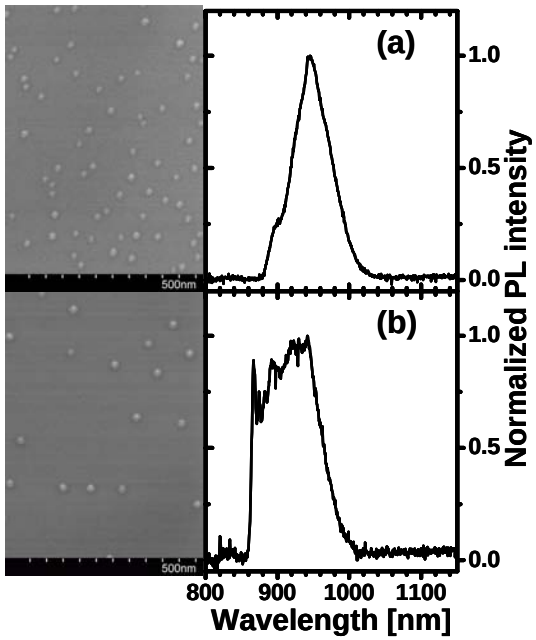

Fig. 4-5. InAs/GaAs QDs growth depending on substrate temperature: (a) 590 °C, (b) 600 °C.

4-2. Modulation of Confinement Potential by Crystal Strain

As mentioned above, the self-organized QD is the product derived from the strain originating from lattice mismatch. Therefore, the confinement potential of a QD will be deeply modulated by

the strain in and around the QD. Here, let us consider the influence of crystal strain on quantum confinement of the QD.

Previously, much effort has been made to apply the InAs/GaAs QDs to the laser source used in optical telecommunication wavelength band by producing a long wavelength emission from $In_xGa_{1-x}As$/GaAs QDs.[92] Through these investigations, it is known that relaxation of the strain around a QD produces a long wavelength emission. Relaxing the strain is commonly achieved by cladding the InAs QDs with an InGaAs layer, whose lattice mismatch is lower than that for GaAs layers.[93] Inducing these strain relaxation layers (SRL) is expected to modulate the confinement potential. T. Amano *et al*. have evaluated the variance of confinement potential originating from the crystal strain in the InAs/GaAs QDs with SRL.[57]

Figure 4-6(a–b) shows the PL spectra of the InAs/GaAs QDs with or without SRL in the high excitation condition. Because the SRL produces a long wavelength emission, the QDs without SRL were grown to a larger size than QDs with SRL in order to adjust the lowest energy emission band. In the figures, the excited state emissions (E2, E3, E4…) are observed because of the state-filling effects under the high power excitation.[94]

What has to be noted here is the energy splitting between the excited states. The sub-band energy splitting is generally derived from the confinement potential structure. For example, the harmonic oscillator potential induces the same energy difference between all sub-levels. In figure (c), the sub-band energy differences (ΔE) between the QDs with and without SRL are compared. It is very interesting to note that the variance of energy splitting in the QDs without SRL is very small and linear. On the other hand, the

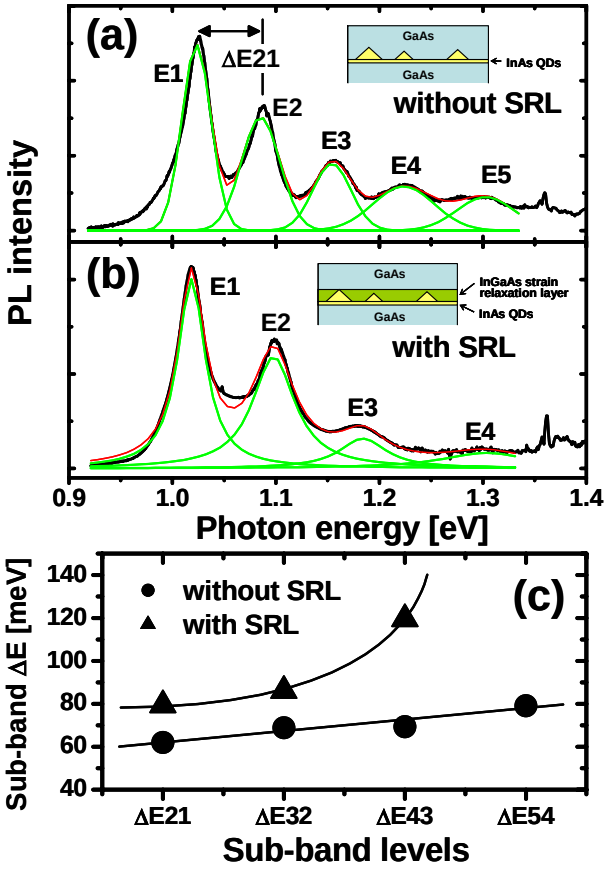

Fig. 4-6. Comparison of InAs QDs with and without SRL. (a-b) PL spectra from InAs QDs samples without SRL (a), with SRL (b). (c) Sub-band energy splitting.

variance of energy splitting in the QDs with SRL dramatically increases with higher excited states. This result indicates that the confinement potential of the QDs without SRL is similar to the harmonic oscillator potential, and that of the QDs with SRL is similar to the square-well potential. This is schematically shown in Fig. 4-7. In the case of the QD without SRL, the crystal strain induces a deformation of confinement potential in a QD, which is similar to the harmonic oscillator potential [figure (a)]. On the other hand, in the case of the QD with SRL, the relaxation of the strain yields the square-well-like potential.

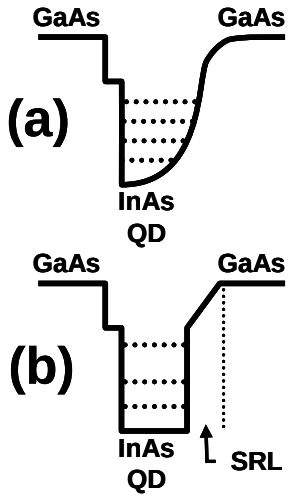

Fig. 4-7. Confinement potential. (a) Without SRL. (b) With SRL.

Thus, the crystal strain around a QD plays a significant role in the confinement potential and the electronic state in QD systems.

4-3. Crystal Strain and Ordering Growth of Quantum Dots

The quantum information device requires the operation of a single quantum two-level system. Therefore, the site-controllable fabrication technique of QDs is crucially important from a practical viewpoint. As already stated, QDs grow in the wake of a crystal strain. Consequently, based on this feature, there have been many attempts to grow self-organized QDs at arbitrary locations. For example, there have been reported that QDs were grown on a V-groove substrate,[95] a patterned holes on a substrate,[96] an atomic layer step on a buffer layer surface,[97] and a misfit dislocation.[98] Recently, the direct writing deposition of indium molecules on a substrate using the cantilever of an atomic force microscope (AFM) has been demonstrated.[99] An extreme crystal strain acceleration results in a dislocation and a defect. In the latter case, it is well known that micrometer-size defects, the so-called “oval defects,” are formed in MBE growth. Although an oval defect was previously considered as a weak crystalline region leading to the degradation of electronic devices, it has been revealed from the results of micro photoluminescence (μ-PL) measurement that such a region is not very weak.[100] Thus, the strain originating from the oval defect can possibly be used for the site alignment of QDs; therefore, the investigation of the quality of QDs in the presence of oval defects

has enormous significance. In this section, we discuss the self-alignment of InAs QDs in the strain region produced by oval defects in the GaAs matrix.

4-3-1. Self-Aligned Growth of Quantum Dots

In MBE growth, we used the surface-engineered GaAs (001) substrate to accelerate oval defect formation.[100] After a 500 nm i-GaAs buffer layer was grown on the substrate, a 1.65-monolayer (ML) InAs QD layer and a 150 nm i-GaAs cap layer were sequentially grown at 600ºC. Finally, another 1.65-ML InAs QD layer was grown on top of the surface under the same conditions to confirm QD formation.

Figure 4-8 shows SEM images of the top of the sample surface. As shown in figure (a), the QDs are orderly aligned along an oval whose typical area is 1.2 × 0.4 μm. The oval alignment of QDs is caused by the oval strain that does not evolve to form a defect. This is based on the fact that the elliptic direction of such an alignment corresponds to that of QDs aligned around a complete defect [figure (b)]. Here, the in-plane densities of the oval aligned QD group and the complete oval defect are 1.7×10^8 and 7.5×10^4 cm^{-2}, respectively. Furthermore, a remarkable feature is that QDs hardly exist outside the strain or defect region. This shows that InAs molecules are very sensitive to strain during prestack migration before QD formation.

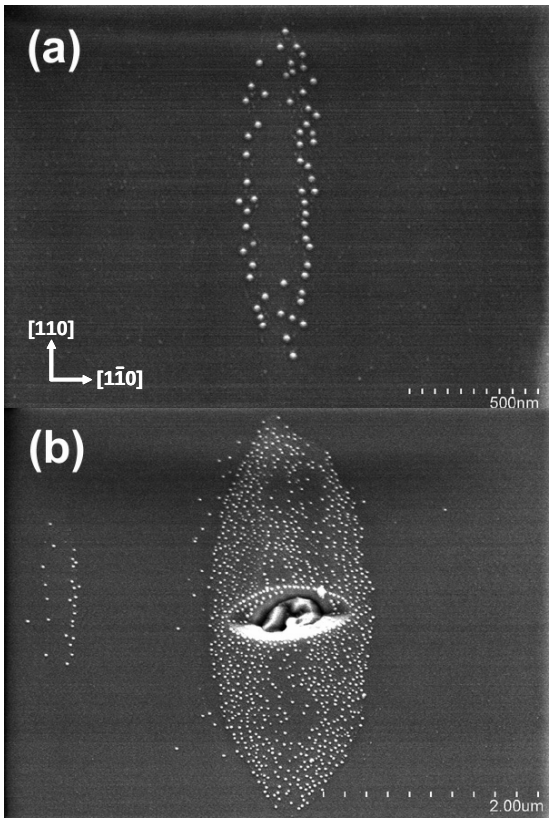

Fig. 4-8. SEM images of the sample surface. (a) Selective QDs growth in the presence of oval strain. (b) QDs growth near the oval defect.

4-3-2. Optical Characteristics

Next, we evaluated the optical properties of self-aligned QDs embedded in the GaAs matrix by means of the μ-PL experiment. The selective QD growth enables us to observe only the QDs aligned on the oval strain or defect region, because the in-plane density of the QD group on the

strain is sufficiently low compared with the spatial resolution of our measurements. The experimental set-up is schematically shown in Fig. 4-9. We used a standard microspectroscopy system with a 50× large-numerical-aperture objective lens whose spatial resolution was ~3μmϕ. The observation of emission spectra was performed using a 55 cm single monochromator and a cooled charge-coupled device (CCD) detector. The sample was cooled to 10 K in a liquid helium flow cryostat, and a semiconductor laser was used as an excitation source whose photon energy was 1.95 eV.

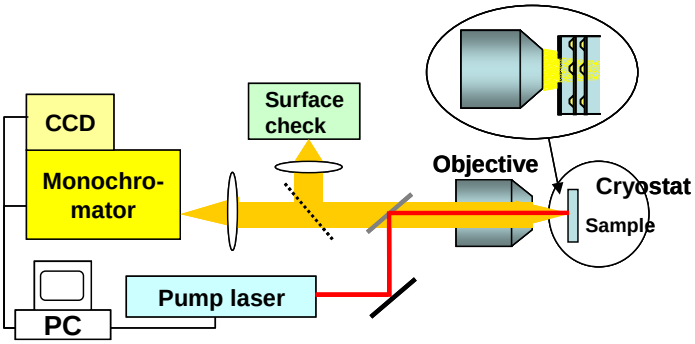

Fig. 4-9. Micro-spectroscopy experimental setup.

The μ-PL spectrum of the self-aligned QDs is presented in Fig. 4-10(a). The spectrum shows the PL peaks from the free exciton in the GaAs matrix (fX_{GaAs}), the bound exciton in GaAs defects (bX_{GaAs}),[100] and the exciton in an InAs wetting layer (WL). Furthermore, at a lower energy (1.25–1.41 eV) than the WL peak, many sharp (less than the resolution limit) peaks are observed (X_{dots}) in the spectrum. These sharp peaks are attributed to the self-aligned QDs of the first InAs layer on the GaAs strain region. The sharpness of the peaks reflects the three-dimensional confinement of carriers in QDs and the PL energies correspond to the energies of InAs QDs reported in many previous studies.[55, 101, 102] For additional evidence confirming the peaks from QDs, we only need to check the PL spectra of other observation points, because QDs do not exist outside the strain region. Figure 4-10(b) shows the PL spectrum at the different spatial

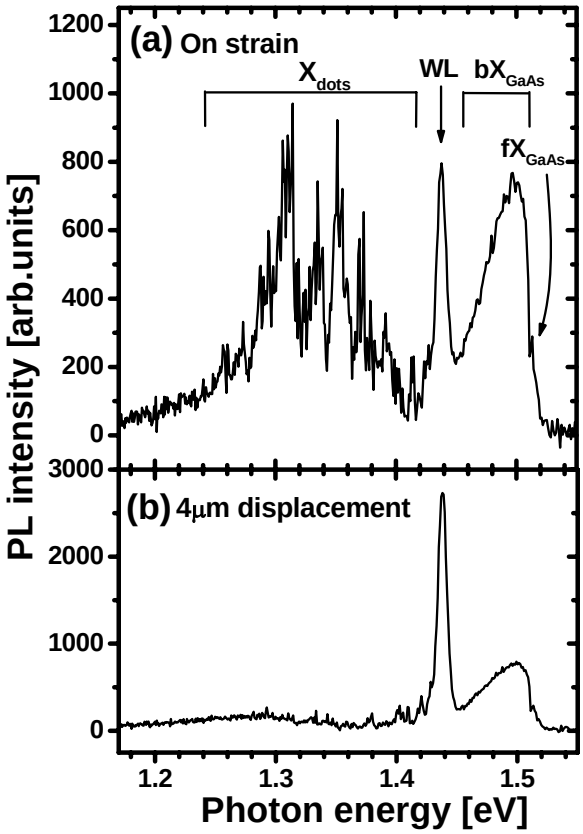

Fig. 4-10. μ-PL spectra.
(a) Near the oval defect.
(b) 4 μm displacement position from (a).

position: a 4 μm displacement from the position in figure (a). In figure (b), the sharp peaks vanish and the WL peak intensity increases. Here, based on the 3.5 × 1.5 μm location area of the oval defect QDs, the vanishing of QD emissions at the 4 μm displacement position is reasonable. In other words, the sharp peaks in figure (a) certainly originate from the QDs in the strain region. In addition, the PL intensities of the fX_{GaAs} and bX_{GaAs} peaks are similar to that in figure (a), in contrast to the increase in WL and the vanishing of X_{dots}. These observations imply that the carriers transported in the WL are effectively supplied to QDs, which indicates the few number of non-radiative recombination centers and the high quality of QDs on the strain region

To obtain more details of the emission properties, we measured the high-resolution μ-PL and μ-PLE spectra using a 1 m double monochromator and a tunable cw Ti:sapphire laser. In Fig. 4-11, we present the μ-PL and μ-PLE spectra obtained from a single self-aligned QD. The PL spectrum shows an extremely sharp PL peak from a single QD whose full width at half maximum (FWHM) is 26 μeV (the resolution limit of the system), which is similar to a conventionally grown InAs QD.[55,101,102] The width of the PL peak reflects the lifetime of an exciton, which indicates the stability of exciton states. Consequently, our observation of the sharp peaks shows the high stability of exciton states in a self-aligned QD, which indicates the few number of carrier scattering factors in a QD crystal. The inset in Fig. 4-11 shows the PLE spectrum of the single self-aligned QD indicated as “Detect.” The zero absorption region (1.350–1.376 eV) in the spectrum is the result of the discrete excited levels produced by a three-dimensional confinement. Moreover, the spectrum shows a discrete peak (indicated as “LO”) at an energy corresponding to the longitudinal optical (LO) phonon of InAs (30.1 meV).[55,102] The appearance of this LO phonon resonant peak indicates the existence of an effective carrier–LO phonon interaction in self-aligned QDs. The carrier–phonon interaction suggests the crystalline quality of QDs, because the existence of a phonon requires a certain crystalline quality level. Therefore, these observations reveal that the

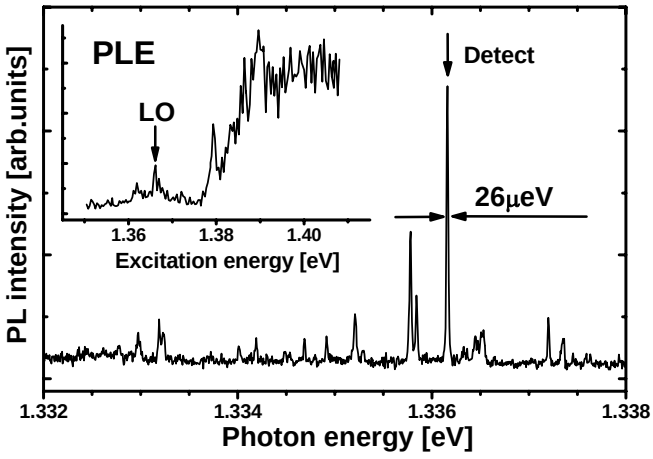

Fig. 4-11. High-resolution PL spectrum of single self-aligned QD. The inset shows the μ-PLE spectrum of the arrowed peak.

self-aligned QD in the strain region has a sufficiently high crystalline quality for preserving the carrier–LO phonon interaction.

Additionally, we investigated the excitation power dependence of the PL spectra in self-aligned QDs. If there are many non-radiative recombination centers around the strain region, the photo-generated carriers will be incorporated into these non-radiative centers at a high excitation intensity. Fig. 4-11, we present the excitation power dependence of the PL spectra in self-aligned QDs. The increase in the peak number on the high energy side (1.35–1.4 eV) with increasing excitation intensity is attributed to the luminescence from the excited states in QDs due to the state-filling effect.[103] At a high excitation intensity, the surplus carriers, which are not expended in QDs, are expected to be distributed in the WL, bX_{GaAs}, or non-radiative recombination centers. The inset in Fig. 4-11 shows the integral PL intensities of the luminescence bands of X_{dots}, WL, and bX_{GaAs} as a function of excitation intensity. As shown in the figure, the increase in the intensity of the WL is inversely proportional to the intensity of the QDs that saturate with increasing excitation intensity, in contrast to the bX_{GaAs} intensity that shows a linear increase. This observation shows that the surplus carriers are expended not in the non-radiative recombination centers but in the WL. In other words, these photo-generated carriers are radiatively recombined efficiently in the self-aligned QDs, free from the effect of the non-radiative recombination centers around the strain region.

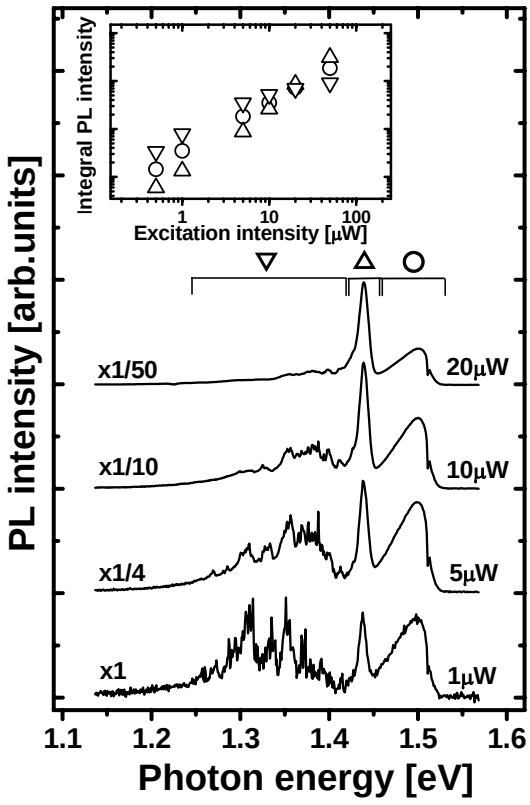

Fig. 4-12. Excitation power dependence of PL intensity.

Thus, our experimental results show that the QDs grown in the crystal strain region are of high quality, similar to a conventionally grown QD, and have a potential for site controlled QD growth.

4-4. Coupled Quantum Dot Fabrication

4-4-1. Vertically Coupled Quantum Dot

Next, we discuss the growth technique for coupled QD (CQD). As previously mentioned, the crystal strain acts effectively on the site selective QD growth. When multiple layers of QD are stacked with barrier layers, the 1st layer QD induces crystal strain in the covering barrier layer around the QD because of lattice mismatch. Therefore, this phenomenon can be used in CQD fabrication.

In multiple stacked QDs, the ordering growth of QDs in the stacking direction (vertical direction) has been closely investigated by Q. Xie *et al.*[104] The features are shown in Fig. 4-13–14. As seen in the cross-sectional transmission electron microscope (TEM) images of Fig. 4-13, the stacking growth induces the ordering growth of QDs, which are directly located above the 1st layer QDs. The bottom drawing in Fig. 4-13 indicates the mechanism of ordering of QD growth. The 1st layer QD causes a crystal strain in the barrier GaAs crystal, and the supplied InAs molecules susceptibly sense this strain and construct the next layer QDs in the strain region. Here, it is easy to predict that the thick GaAs barrier layer inhibits the coupling growth because of strain relaxation. Q. Xie *et al.* gave a detailed discussion of this point. Figure 4-14 indicates the coupling growth probability (pairing probability) between upper and lower QDs as a function of the GaAs barrier thickness. As shown in the figure, the pairing

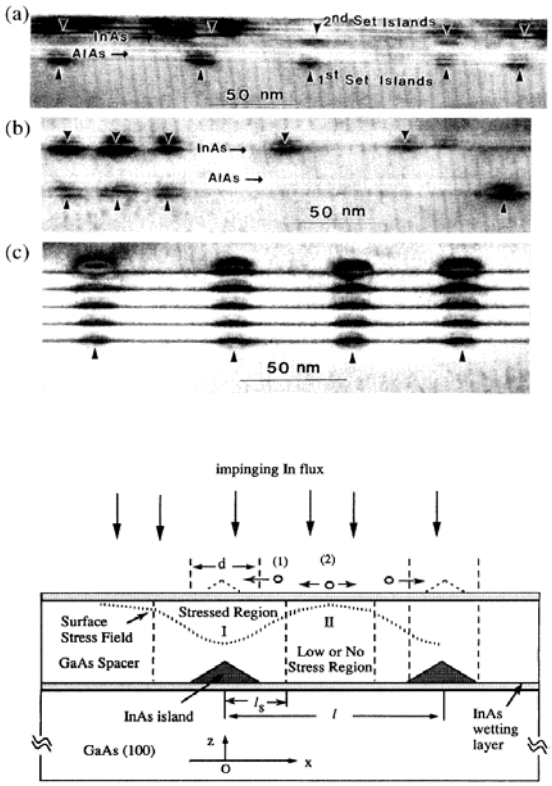

Fig. 4-13. InAs/GaAs stacking QDs. (above) Cross-sectional TEM images. (below) Stacking growth mechanism. reported by Q. Xie *et al.*.

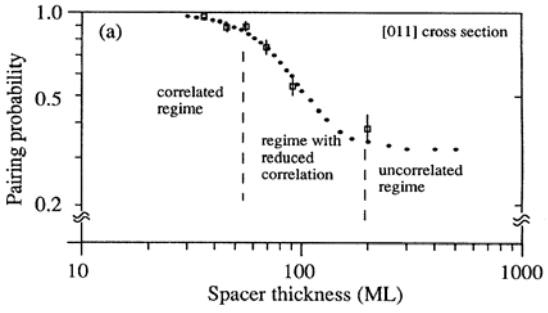

Fig. 4-14. Coupling growth probability as a function of barrier thickness, reported by Q. Xie.

probability between upper and lower QDs is more than 90% in the cases when the barrier thickness is less than 40 ML (~11 nm, 1 ML = 0.283 nm in GaAs). In our study, we fabricated the CQD samples using the growth technique of vertically stacked CQDs.

However, simple stacking growth is inadequate for our purpose, which is the observation of the physical properties of a CQD involving a quantum mechanically coupled system. Because the inter-dot distance required for quantum mechanical coupling is expected to be less than 5 nm, which is comparable to the QD height (~5 nm), such a thin barrier layer close to the QD height will induce a non-uniformity of the barrier layer. Furthermore, the 2nd layer QDs grown on the concavoconvex surface are at risk of being deformed. An example is presented in Fig. 4-15.[105] It is not easy for us to estimate the inter-dot distance because of the large deformation of barrier layers, and the upper QD shape is deformed compared to the 1st layer QD.

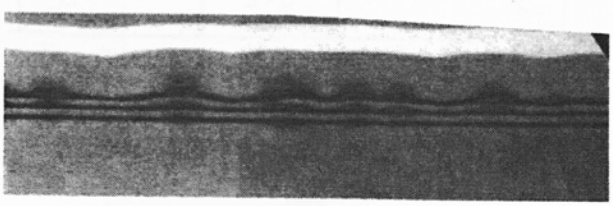

Fig. 4-15. Deformation of barrier layer and QD shape in stacking growth.

4-4-2. Indium-Flush Method

To solve this problem, we used the "Indium-Flush" growth technique proposed by Z. R. Wasilewski *et al.*[106] While they adopted this method to grow similarly sized upper and lower layer QDs, it is also useful for fabricating adjacently stacked QDs. The growth procedure of the Indium-Flush (I-F) method is shown in Fig. 4-16. First, the 1st InAs QD layer is normally grown on a GaAs buffer layer. Next, a thin GaAs layer, the so-called "partial cap layer" whose thickness is less than the QD height (<5 nm) is grown. Then, the substrate temperature is risen upto 30–40°C, and is immediately dropped to the former temperature (I-F process). Then, the GaAs barrier layer is grown with an arbitrary thickness, and the 2nd InAs QD layer is sequentially grown. The same I-F process is applied to the 2nd QD layer, and finally the QD layers are covered by the GaAs cap layer. The key point in this procedure is the

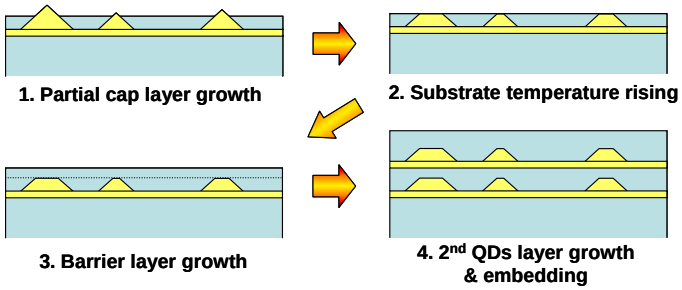

Fig. 4-16. Growth procedure of Indium-Flush method

partial cap layer and the I-F process. While there are convexoconcave features on the surface of the as-grown partial cap layer due to the existence of 1st layer QDs, the temperature rise of the substrate induces the migration and reconfiguration of the surface molecules, and provides a flat surface. Thus, the 2nd layer QDs are grown on a flat surface produced by the I-F method, and we can obtain high quality CQD samples with a homogeneous barrier layer and less deformed 2nd layer QDs.

4-4-3. Practical Examples of Coupled Quantum Dot Growth

Here, we present practical examples of InAs/GaAs QD growth with the I-F method. The effect of the I-F process is shown in the PL spectra of Fig. 4-17, where the thicknesses of the InAs and the partial cap layer were 1.65 ML and 4 nm, and the temperatures of the substrate and the I-F process were 600 and 630°C, respectively. As seen in the figure, the PL spectrum of QDs with the I-F process shows a blue shift of emission wavelength due to the enhancement of quantum confinement by truncation of the tops of the QDs with the I-F application. Figure (b) indicates the dependence of the partial cap layer (InAs layer: 1.7 ML) on the thickness. A partial cap layer thickness less than 4 nm causes a blue shift of the longer wavelength edge of the emission curve, which indicates the truncation of the tops of the QDs. In other words, this result implies that the height of InAs QDs is about 4–5 nm.

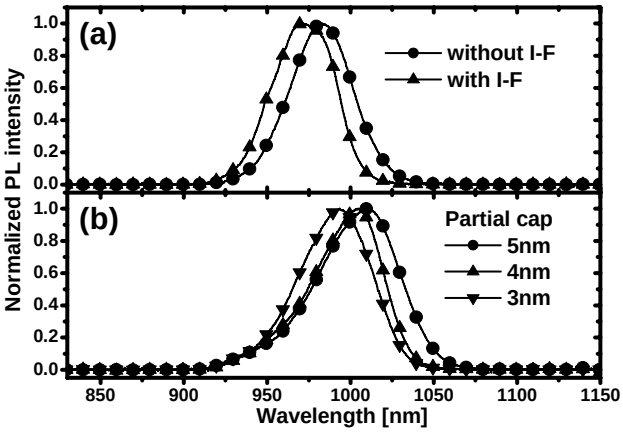

Fig. 4-17. PL spectra of QDs grown by I-F method.
(a) Effect of I-F method in single QDs layer.
(b) Dependence on thickness of partial cap layer.

Next, we show examples of CQD growth. As mentioned above, the growth of the 2nd layer QDs is accelerated by the strain originating from the 1st layer QDs. Consequently, if the same amount of InAs is supplied for both the 1st and 2nd layer growths, the QDs of the 2nd layer grow larger than those of the 1st layer. Therefore, in order to fabricate the upper and lower QDs with similar sizes, the small amount of indium supplied to the 2nd QD layer must be controlled. This feature is seen in Fig. 4-18. In this figure, the 2nd InAs layer thickness is varied with a constant 1.65 ML thickness of the 1st InAs layer, where the partial cap and barrier layers are 4 and 5 nm thick, respectively. As

seen in the figure, in the case of similar thicknesses of the 1st and 2nd layers (1.6, 1.7 ML), the 2nd layer QDs exhibit longer wavelength emission than the 1st layer QDs because of the weakness of quantum confinement originating from the larger size growth of 2nd layer QDs. With the reduction in the 2nd InAs layer thickness, the QD size decreases, which induces the blue shift of the emissions. A decrease in the thickness from 1.4 to 1.5 ML results in a similar size of upper and lower layer QDs. A further reduction of 2nd layer thickness (1.35 ML) provides more smaller sized QDs in the 2nd layer than those in the 1st layer, which causes the blue shift of the 2nd layer emission compared with the wavelength of the 1st layer emission. Thus, it is possible to control the energy difference between the upper and lower QDs by adjusting the thickness of the 2nd QD layer.

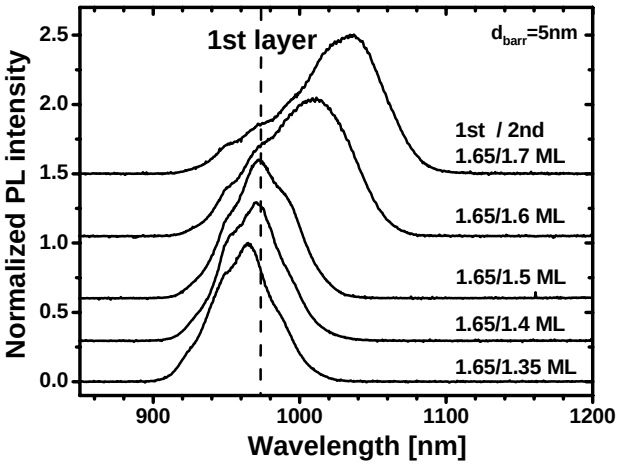

Fig. 4-18. PL spectra of CQDs. Dependence on thickness of 2nd InAs layer.

Finally, we consider the application effect of the I-F process on CQD growth. Figure 4-19 presents the PL spectra of the CQD with or without the I-F method. The barrier layer thickness "d" was changed to 3 nm [(a), (c)] and 5 nm [(b), (d)]. Figure (a-b) indicates the CQDs with the I-F method, and figure (c-d) indicates the CQD without I-F. Each graph contains two PL curves under the conditions of high (lower curve) and low (upper curve) excitation intensities. Here, the InAs layer thicknesses were adjusted as 1st/2nd = 1.65/1.4 ML. Consequently, the longer wavelength peak (indicated as 1st) is attributed to the 1st layer QDs and the shorter wavelength peak (indicated as 2nd) to the 2nd layer QDs. Comparing d = 3 nm with 5

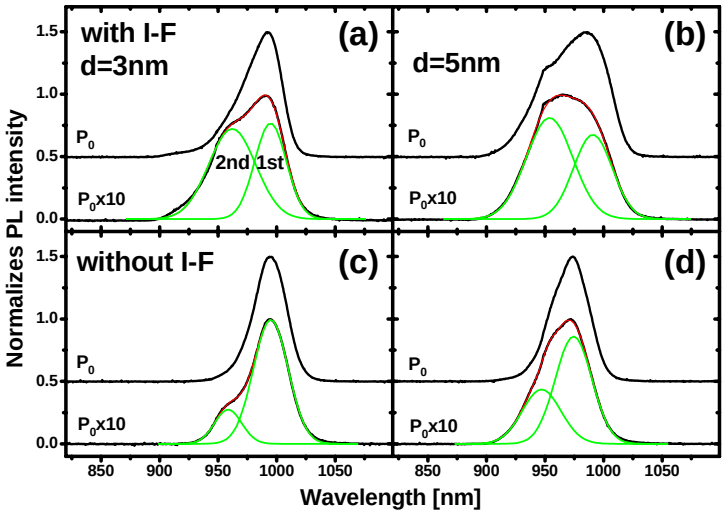

Fig. 4-19. Application effect of I-F process in CQD growth.

nm, the 2nd layer QDs with d = 3 nm emit light with great difficulty. This is because the photo-generated carriers in the 2nd layer QDs leak into the 1st layer QDs because of the thin barrier. Here, let us focus on the application effect of the I-F process. Comparing figure (a-b) with (c-d), the 2nd layer QDs without I-F emit light with great difficulty in both cases of d = 3 and 5 nm. This means that the carriers easily leak into the 1st layer QDs in the CQD without the I-F process. This phenomenon is considered to occur because the barrier layer without I-F cannot adequately separate the upper and lower QDs because of the convexoconcave nature of the barrier layer surface. Thus, the I-F method is absolutely essential for fabricating the CQD samples with adequate barrier thickness and a stacked structure.

4-4-4. Comparing with Other Self-Organized CQD Systems

Finally, we summarize a CQD sample comparing our samples with other self-organized CQD structures. To investigate a single CQD system, very low in-plane QD density is first required for single QD spectroscopy. To investigate the physical properties dependent on the interdot distance, we need to precisely control the barrier thickness between the two QDs. Because the energy difference between the QDs influences the strength of the interdot interaction, it is preferred that both QDs have the same size and the same crystal composition. Furthermore, reproducibility of QD growth is also needed to compare the different samples. In addition, it would be better if the sample shows a high optical response.

Table 4-1 compares various self-organized CQD structures with respect to these five perspectives. The GaAs quantum disk induced in a very narrow quantum well has excellent crystal composition and optical response,[29] but it is difficult to control the QD size and interdot distance because the disk is fortuitously formed at the concavoconvex edge of the quantum well. With lateral CQDs, it is also difficult to control the interdot distance because of the uncontrollable QD formation.[107] The $In_xGa_{1-x}As$ vertical QD makes it possible for us to control the in-plane QD density, but it is difficult to produce the precise crystal composition because very low growth rate is required for the crystal growth of QDs.[108] It was mentioned above that the InAs vertical CQD without Indium-Flush method has concavoconvex barrier layers.

Compared to the above examples, the InAs vertical CQD grown with the Indium-Flush method shows excellent controllability of interdot distance. As mentioned in the previous sections, these

CQDs also provide good controllability of in-plane QD density and QD size, which are crucial for single dot spectroscopy and investigation of interdot interaction. Thus, the fabrication method used in this work provides the best CQD samples for the investigation of physical properties in a single CQD system.

Table 4-1. Comparison of self-organized CQDs

	Reproducibility of Crystal Composition	Controllability of In-plane QD Density	Controllability of QD Size	Controllability of Interdot Distance	Optical Response
InAs Vertical CQD with I-F 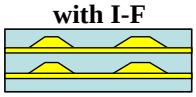	○	◎	◎	◎	△
InAs Vertical CQD without I-F 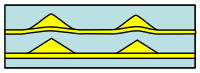	○	◎	○	○	△
InGaAs QDs 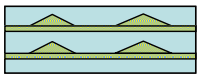	△	○	○	—	○
Lateral CQD 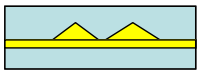	—	×	×	×	—
GaAs Disk 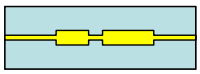	◎	×	×	×	◎

In Fig. 4-20, we present the cross-sectional scanning transmission electron microscope (STEM) image of the CQD sample used in our study (see Section 5-2). The thickness of each layer was adjusted so that the 1st/2nd InAs layer = 1.65/1.45 ML, the partial cap layer = 3.5 nm, and the GaAs barrier layer = 7 nm, respectively. From this image, the lateral and vertical sizes of QDs are estimated as about 20 and 3 nm. As seen in the figure, the 2nd layer QDs are grown just above the 1st layer QDs, and the barrier layer is not deformed.

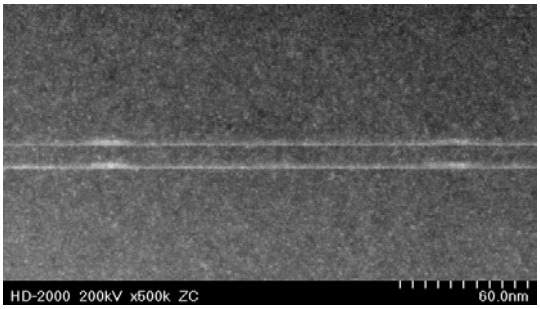

Fig. 4-20. Cross-sectional STEM image of the CQD used in this study.

Thus, in our study, we estimated the optical properties of a CQD system on the basis of

correctly fabricated samples.

4-5. Sample Preparation for Single Dot Spectroscopy

In the next chapter, we present the observation results for single CQD. In order to observe a single QD, it is necessary to collect the luminescence from only a single QD and this must be directed into a monochromator. Therefore, the number of QDs within the visual area of a lens must be around one. While we used the objective lens for focusing the excitation light and the collection of luminescence, its spot size of 2–4 μm remained insufficient for single QD observation, compared to the in-plane QD density of 20–100 pcs/μm^2.

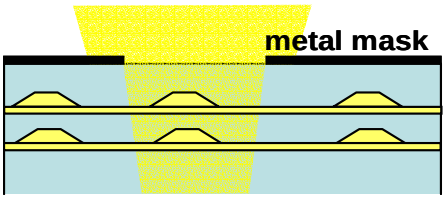

Fig. 4-21. Sample construction for single QD observation.

For this reason, we fabricated an aperture mask on the sample surface for light interception.[26] Figure 4-21 presents a schematic diagram of sample construction. The fine pores on the metal surface make it possible for us to observe only an area less than the spot size of an objective lens. We chose Ti/Au (100/700 Å) as the metal mask, and fabricated the fine pores (0.2–0.5 μmϕ) by means of electron beam lithography and the lift-off technique.

Figure 4-22 shows the actual sample surface. As seen in figure (a), the addresses were marked in the metal mask, and enabled us to observe the same position in repeat experiments. Figure (b) presents the expanded SEM image around a pore, in which the fine pore formation of 0.2 μmϕ is confirmed. Figure (c) shows an SEM image of the sample surface before mask fabrication. The optimization of QD growth conditions gave low in-plane QD density, and accordingly, pores of 0.2 μmϕ sufficiently ensured the selectivity of a single QD.

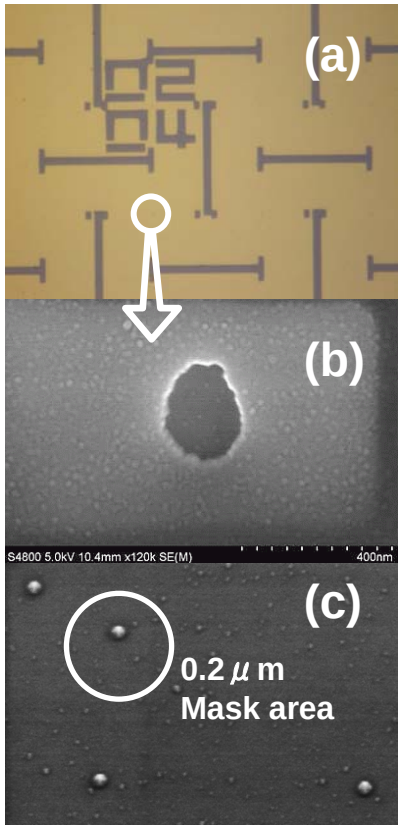

Fig. 4-22. Images of sample surface.
(a) Metal mask pattern.
(b) Fine pore formation (0.2 μmϕ).
(c) Surface before mask fabrication.

Thus, the observations of optical properties mentioned in the next chapter were performed using reliable samples of CQDs fabricated as mentioned above.

5. Optical Properties of Coupled Quantum Dots

In this chapter, we detail the optical characteristics of InAs/GaAs coupled quantum dot (CQD), which were fabricated by methods mentioned in the previous sections. In Section 5-1, we determine the optical properties of CQD ensembles by macrospectroscopic observations. The optical characteristics of single CQDs observed by microspectroscopy will be discussed in Section 5-2 or later.

5-1. Optical Properties in Non-Resonant Coupled Quantum Dots Ensembles

In this section, the optical characteristics of CQD ensembles are presented. While each QD is expected to individually exist under different surroundings, we firstly estimated the general optical properties of QD ensembles in order to avoid missing out the broader picture of the CQD. In reality, it may be difficult for us to distinguish the upper and lower QDs in the PL spectra by macroscopic measurements, because the QD ensembles show large inhomogeneous PL broadening due to the large size distribution of QDs. However, as mentioned in Section 4-4-3, we achieved distinct observations between the upper and lower QDs by growing smaller QDs in the second QD layer than those in the first QD layer. In this section, we discuss the macro-optical features of the energetically non-resonant CQD.

The samples used in this section are InAs/GaAs CQDs grown by the Indium-Flush (I-F) method mentioned in Section 4-4-3. The thicknesses of the 1st and 2nd InAs QD layers were 1.65 and 1.5 monolayer (ML), respectively. The thickness of the partial capping layer was 4 nm, and we used three samples whose effective barrier thicknesses “d” were 7 nm (sample C), 5 nm (sample D), and 3 nm (sample E), respectively.

5-1-1. PL Spectra Reflecting Wave Function Penetration

Figure 5-1 shows the PL spectra of three non-resonant CQD samples at several excitation

densities, where each spectrum is normalized at the highest peak intensity. The laser diode (635 nm) was used as an excitation source, and we utilized the 55-cm single monochromator and the cooled CCD detector for the spectroscopy, while the samples were cooled to 10 K in a liquid helium flow cryostat. In the inset, we also present the PL spectra of a single QD layer sample grown by the I-F method as a reference. As shown in the figure, we observed two main peaks in the PL spectra of all three CQD samples, and confirmed a noticeable difference of excitation density dependence between the three samples in which the PL intensity of the higher energy peak decreases with reductions in the barrier thickness at the same excitation density. We interpret the two PL peaks as luminescence from the upper (smaller) and lower (larger) QD layers, respectively, as discussed in the section 4-4-3, whereas the excitation density dependence is distinctly different from that in the spectrum of the single QD layer sample. Moreover, this observation indicates that photo generated carriers in the smaller dots, which are the origin of the higher energy peak, transfer to the larger dots due to the thinner barrier. In other words, the reduction in the barrier thickness enhances the tunneling probability between the double QDs.

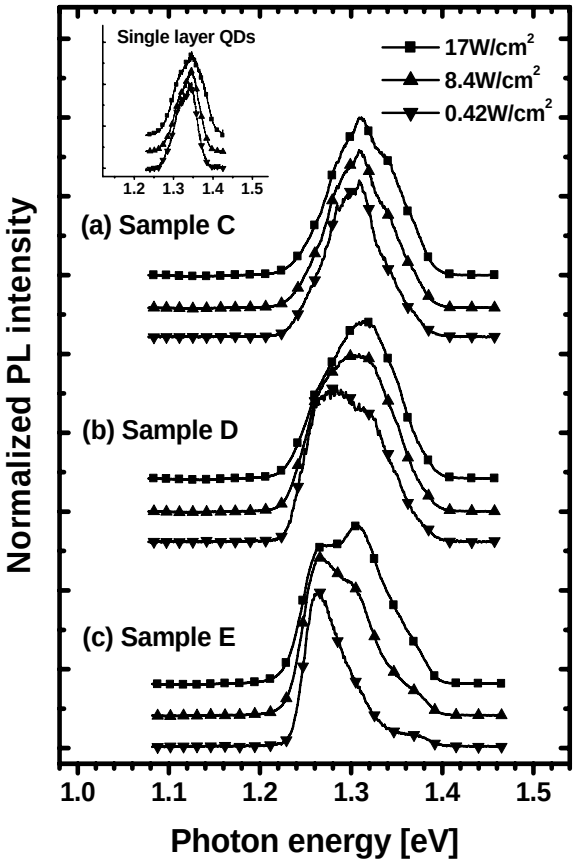

Fig. 5-1. Macro-PL spectra of non-resonant CQDs. Barrier thicknesss "d": (a) 7nm, (b) 5nm, (c) 3nm. The inset indicates the spectra of single layer QDs. Each spectrum is normalized at the maximum intensity.

Let us detail the profiles of the PL spectra. Figure 5-2 presents the results of Gaussian fitting to the PL spectra.

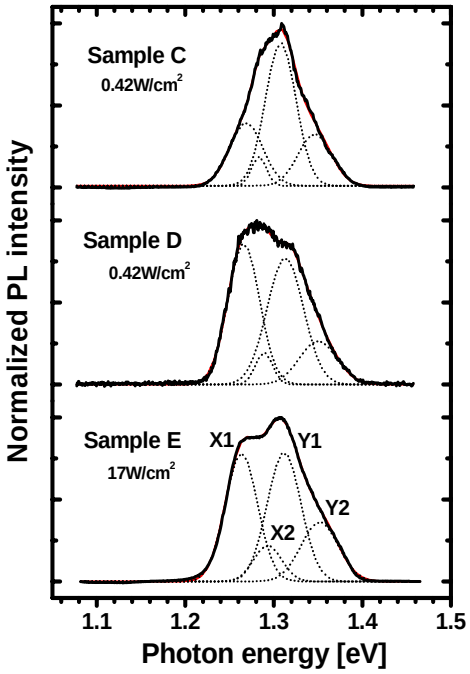

Fig. 5-2. Gaussian fitting to the PL spectra.

All spectra were fitted by four Gaussian curves, where we carefully chose the fitting parameters which satisfied the spectra at six levels excitation densities from 0.42–17 W/cm^2. We assigned two main peaks X1 and Y1 to the lowest excited states of the 1st and 2nd layer QDs, respectively. The sub-peaks X2 and Y2 seem to be the excited states of X1 and Y1.

We then plotted the energies of each peak as a function of the barrier thickness in Fig. 5-3(a). The energy splitting between the main X1 and Y1 peaks increases with reductions in the barrier thickness. This feature can not be explained by an aftereffect of the thin barrier, which leads to a larger strain on the surface and enhances the growth of the 2nd layer QDs. That is because the fact that the 2nd layer QDs are smaller than the 1st layer QDs in our CQDs can not explain the shift in the lower energy peak that originates from the 1st layer QDs. The energy shift natures in Fig. 5-3(a) are attributed to the enhancement of the wave function penetrating to a neighboring QD with the barrier thickness reduction, which causes the weakening of an effective quantum confinement. For comparison, we calculated the energy states of a non-resonant quantum well pair and obtained similar energy shift results to those shown schematically in Fig. 5-3(b). These states are interpreted as the bonding-like and antibonding-like coupling states. However, the higher (Y1) and the lower state (X1) among the coupling states are expected to be mainly occupied by smaller (2nd layer) and larger (1st layer) QD's electrons, because of the weak electron coupling originating from the relatively large energy difference between the upper and lower QDs before coupling. Therefore, the coupling nature in non-resonant CQD systems can be interpreted as the carrier tunneling between QDs.

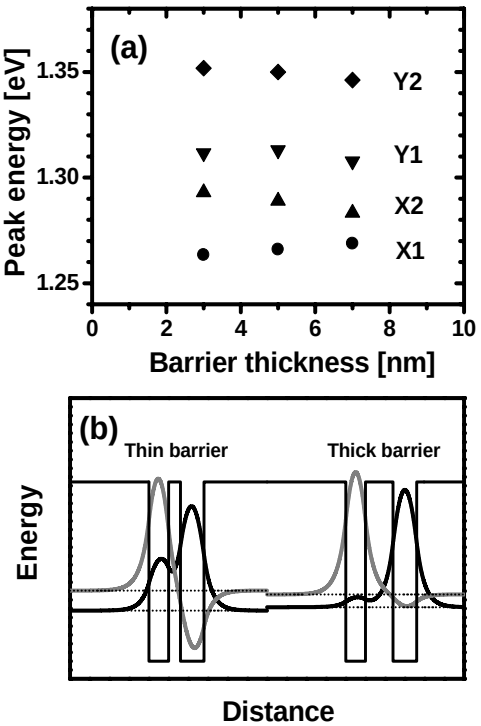

Fig. 5-3. (a) PL peak energies as a function of barrier thickness. (b) Calculation example of wave function in non-resonant coupled quantum wells.

5-1-2. Carrier Transfer Process between QDs

On the basis of the above mentioned discussions, we estimated the carrier transfer transience through the tunneling process from the smaller QD state (Y1) to the larger QD state (X1) by

measuring the PL decay time of the CQD. In the experiments, we used a streak camera (Hamamatsu Photonics C4334) and a picosecond Ti:sapphire laser whose wavelength, pulse repetition, and pulse width were 750 nm, 76 MHz, and 1.9 ps, respectively.

Figure 5-4(a) shows time resolved PL spectra of the sample E (d = 3 nm) at several delay times. It can be seen from the figure that the photo-generated carriers are transferred from smaller QDs (Y1 peak) to larger QDs (X1 peak). Next, we estimate the carrier transfer time. The decay time of smaller QDs (τ_{Y1}) consists of both the carrier transfer time (τ_t) to larger dots and the carrier recombination time (τ_r), and is given by the following rate equation:[109]

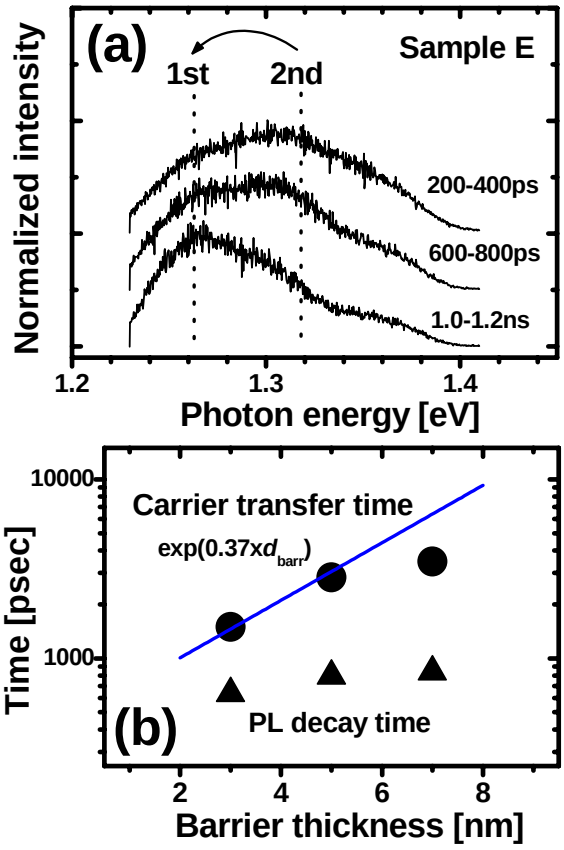

Fig. 5-4. Carrier tunneling between QDs. (a) Time-resolved PL spectra of d=3nm CQD. Each spectrum is normalized at the max intensity. (b) Carrier transfer time vs barrier thickness. The filled triangle indicates the PL life time of Y1 peak. The solid line is the fitting curive (see text).

$$\frac{dN_s}{dt} = -\frac{N_s}{\tau_r} - \frac{N_s}{\tau_t}\ ,\ \tau_t = \frac{\tau_{Y1}\cdot\tau_r}{\tau_r - \tau_{Y1}}, \qquad \text{…Eq. 5-1}$$

where N_s is the carrier density in the smaller dots. τ_r was estimated at 1.24 ns from the decay time of the single layer QDs, and accordingly, we can calculate τ_t from τ_{Y1} and τ_r. The estimated carrier transfer times are presented in Fig. 5-4(b). As shown in the figure, the carrier transfer time decreases with a reduction in the barrier layer thickness, and is longer than the PL life time of single layer QDs.

As is well known, the tunneling probability depends on the barrier thickness and the energy gap between the confinement energy level and the conduction band energy of the barrier material, and is given by a WKB approximation as follows;[39,109]

$$T \approx \exp\left[-2d_{barr}\sqrt{\left(2m^*/\hbar^2\right)(V-E)}\right], \qquad \text{…Eq. 5-2}$$

where d_{barr} is the barrier thickness, m^* is the effective mass in the barrier layer, V is the conduction

band energy of the barrier material, and E is the confinement energy level in the QD. In carrier transfer process, the penetrated carrier needs to be relaxed energetically to the energy level in the neighboring QD (Fig. 5-5). Therefore, the carrier transfer time τ_t involves the energy relaxation time in the energy offset ΔE, and is written as

$$1/\tau_t \approx \exp\left[-2d_{barr}\sqrt{(2m^*/\hbar^2)(V-E)}\right]\times\gamma_{Ph}, \quad \text{…Eq. 5-3}$$

where γ_{Ph} is the energy relaxation probability in ΔE. Our experimental result is fitted by Eq. 5-3 as follows [solid line in Fig. 5-4(b)]:

$$\tau_t\,[\text{ns}] = \exp(0.37\cdot d_{barr}\,[\text{nm}])/0.48, \quad \text{…Eq. 5-4}$$

where the data of d = 7 nm CQDs is neglected in the fitting because of large experimental error. From this fitting result, the barrier height $V-E$ was estimated as 31.4 meV, using m^* = 0.0665 (GaAs electron).

Here, we show the acceptability of this estimated value in another way. In the previous reports,[52,110] the barrier height $V-E$ has been estimated as 140 meV from the results of infrared spectroscopy in InAs/GaAs QDs whose center of luminescence was 1.2 eV. The luminescence energy difference between reported QDs and our smaller dots (1.31 eV) is 110 meV. We can estimate the electron contribution to the energy difference (110 meV) considering that the carrier confinement energy is approximately proportional to $1/m^*$ on the basis of Eq. 2-3. We estimated the electron contribution as 104 meV, assuming that the effective mass of the electron (hole) was 0.023 (0.41). Then, we estimated $V-E$ as 35.8 (73.8) meV for our smaller (larger) QDs, compared with the reported value of 140 meV (Fig. 5-6). This estimation of $V-E$ = 35.8 meV corresponds quantitatively to the estimated value from Eq. 5-4 (31.4 meV). Thus, the barrier thickness dependence of the carrier transfer time is explained by the carrier tunneling probability of Eq. 5-2.

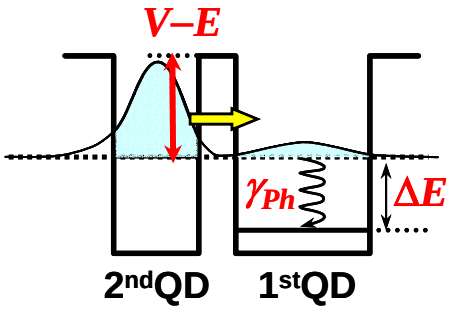

Fig. 5-5. Carrier transfer process in non-resonant coupling system.

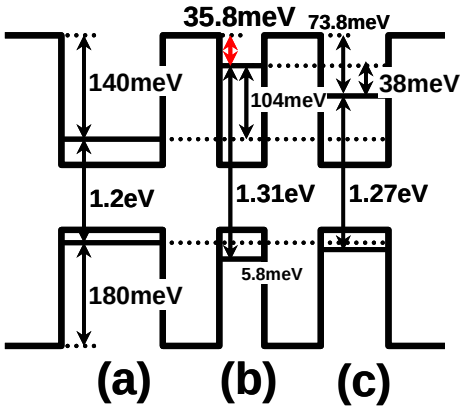

Fig. 5-6. Estimation of energy offset *V-E*.
(a) Band diagram of InAs QD in references.
(b) *V-E* in 2nd layer QD.
(c) *V-E* in 1st layer QD.

Next, we compare our results with the other reported results. Figure 5-7 shows the carrier transfer time as a function of Gamow transmission factor $d_{barr}[m^*(V\text{-}E)]^{1/2}$. The square in the figure indicates the reference data in the case of InAs/InAlAs CQDs given by A. Tackeuchi *et al*.,[109] and the triangle indicates the reference data in the case of InAs/GaAs CQDs given by Yu. I. Mazur *et al*.[111] Our estimated value is not only longer than the PL life time but is 10 times as large as these reference values. This mismatch is considered to come from the energy relaxation probability γ_{Ph} in Eq. 5-3.

S. Muto *et al*. discussed the t carrier transfer process in a non-resonant coupled quantum well.[112] They indicated that the carrier transfer process was determined by the energy relaxation time of the tunnel electrons in the neighboring well (ΔE in Fig. 5-5). Furthermore, they suggested that the longitudinal optical (LO) phonon played the main role in the carrier transfer process. This is because the LO-phonon produces fast intraband relaxation due to strong coupling with the electron.[113] In contrast, when the energy relaxation requires an acoustic phonon emission, the energy relaxation time is one order of magnitude longer than that by the optical phonon.[5] In our case, the energy separation ΔE is estimated as 38 meV (see Fig. 5-6), which does not agree with the LO-phonon energy (~34 meV in InAs QD[114]). This mismatch is compensated by the acoustic phonon emission, which results in a long carrier transfer time.

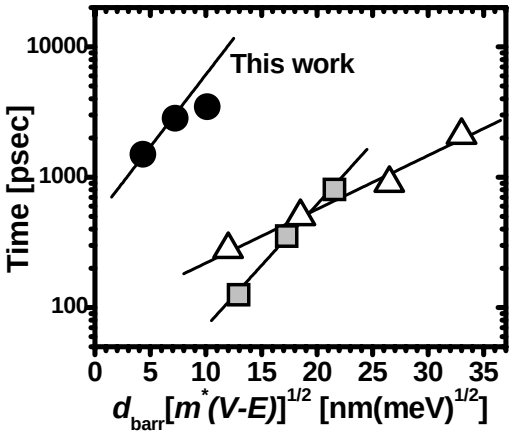

Fig. 5-7. Comparing with the previous reports. The squar and triangle indicate the reference values reported by A. Tackeuchi *et al*. and Yu. I. Mazur *et al*., respectively.

From Eq. 5-4, we estimated the energy relaxation time $1/\gamma_{Ph}$ as 480 ps. This value corresponds to the theoretical estimation of the energy relaxation time with LO + acoustic phonon.[115] On the other hand, in reference reports, the energy separation ΔE between two QDs is larger than 80 meV (much larger than our case). In this case, it is highly possible that there are real electron levels in ΔE. Because the transition probability through the real electron levels is high (several tens picosecond), the carrier transfer times in the references are thought to be shorter than our observations. Thus, the long carrier transfer time in our case is attributed to the fact that the electron energy relaxation in the carrier transfer process is interrupted because of the small energy separation between QDs,

namely, the phonon-bottleneck effect.

5-1-3. Electron–LO-phonon Interaction in Coupled Quantum Dots

In addition, we discuss the barrier thickness dependence of the electron–LO-phonon interaction in non-resonant CQD systems. Figure 5-8 presents the photoluminescence excitation (PLE) spectra of the non-resonant CQD, where the excitation source is a cw Ti:sapphire laser. As shown in the figure, we clearly observed the PLE peaks resonant to the LO-phonon (34.5 meV), which indicates strong interactions between the carriers and the LO-phonon in the CQD. Furthermore, one noticeable feature is that the intensity of the LO-phonon resonant peak decreases with a reduction in the barrier thickness.

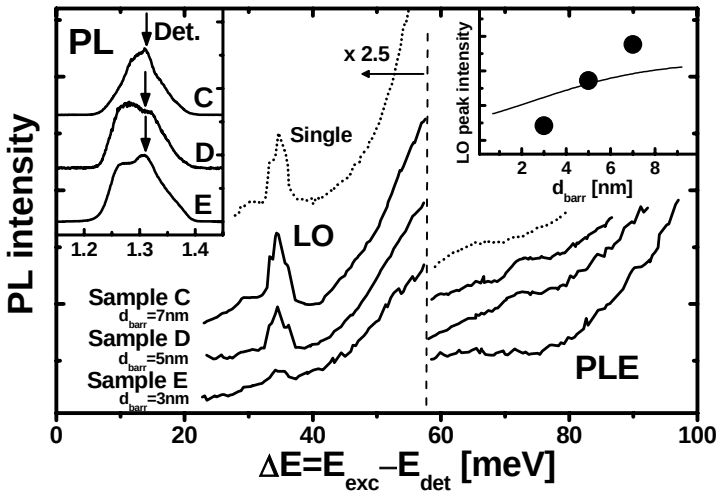

Fig. 5-8. PLE spectra of non-resonant CQD. Each spectrum was detected at the arrowed PL peak in the left inset. The right inset shows the integral PLE intensity of the LO resonant peak as a function of the barrier thickness. The solid line is the theoretical curve (see text).

One possible interpretation of this observation is the competitive process between the electron–LO-phonon interaction and the electron tunneling process. In this competitive process, as shown in Fig. 5-9, the rate equation of the carriers is written as

$$\frac{dN_0}{dt} = \frac{N_1}{\tau_{LO}} - \left(\frac{N_0}{\tau_{PL}} + \frac{N_0}{\tau_{t0}}\right), \quad \frac{dN_1}{dt} = \Gamma - \left(\frac{N_1}{\tau_{LO}} + \frac{N_1}{\tau_{t1}}\right), \qquad \text{…Eq. 5-5}$$

where τ_{LO} is the energy relaxation time caused by the electron–LO-phonon interaction, τ_{PL} is the carrier recombination time, τ_{t0} and τ_{t1} are the carrier transfer times through the tunneling process in the ground and excited levels, N_0 and N_1 are the carrier populations in the ground and excited levels, and Γ is the excitation rate. From these equations, the PL intensity I_{LO} (PLE intensity of the LO

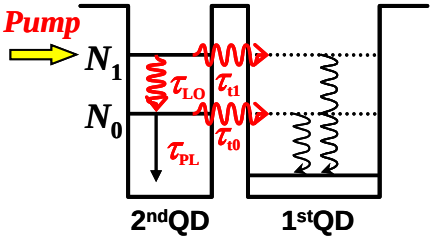

Fig. 5-9. Competitive process between the electron–LO-phonon interaction and the electron tunneling.

resonant peak) is given by

$$I_{LO} = \frac{N_0}{\tau_{PL}} = \Gamma \cdot \frac{1}{1+\tau_{PL}/\tau_{t0}} \cdot \frac{1}{1+\tau_{LO}/\tau_{t1}}. \quad \textbf{…Eq. 5-6}$$

In the right inset figure of Fig. 5-8, we present the application result of Eq. 5-6 for data reproduction, where τ_{t0} is given by Eq. 5-4 and τ_{PL} is 1.24 ns. The theoretical consideration of Eq. 5-6 corresponds to the experimental result as a general trend, but acceptable fitting could not be achieved with any fitting parameters. This result implies that some other physics remains concealed. For example, it is thought that the electron–LO-phonon interaction itself is weakened by a thin barrier thickness. This possibility has been discussed by P. Borri *et al.*,[116] in which they proposed that the overlap between the acoustic phonon and the electron wave function in the interaction matrix element was cut off in the very narrow quantum well by the “equivalent” well thickness because of the penetration of the electron wave function into the barrier. However, further investigations are required to interpret our results.

5-1-4. Conclusion

In conclusion, we discussed the macro-optical characteristics of non-resonant CQDs. The excitation power dependence of the PL spectra indicated an enhancement in the tunneling probability between QDs with a reduction in the barrier thickness. From the results of the PL peak shift, we also confirmed the weakening of effective quantum confinement because of the penetration of wave function into a neighboring QD. We estimated the carrier transfer time between QDs and found a long tunneling time, which was more than the PL life time in a single QD. This result suggests that the electron transfer process is interrupted by the phonon bottleneck effect originating from the small energy separation between QDs. Additionally, we discussed the competitive nature between the electron–LO-phonon interaction and the carrier tunnel transfer process on the basis of the PLE experiments.

5-2. Electronic Structures in a Single Coupled Quantum Dot

In the preceding section, the macro-optical characteristics of non-resonant CQD ensembles were presented. In this and the following sections, we discuss the optical properties of a single resonant CQD. The electronic structures of a single CQD are mentioned in this section, and then we discuss the interdot interactions in a CQD system in the following sections.

As previously mentioned, the main purpose of this study is to observe interdot interactions in a CQD system, as shown in Fig. 3-6. For this, we first need to detail the electronic structures in a single CQD. Although several observation results of single CQD have been reported,[29,38,74,117,118,119,120] these studies focused only on the fine structures around the ground exciton states, and little attention was given to the higher electronic states. In this section, we consider the overall electronic structures, involving higher energy states, in a CQD system with various interdot spacings.

5-2-1. Samples and Experimental Setup

The samples used in this section were InAs/GaAs CQDs fabricated by the Indium-Flush method, as shown in Section 4-4-3. We achieved a low in-plane QD density of 4–30 pcs/μm^2 by optimizing the growth conditions, which enabled us to perform single dot spectroscopy. At the same time, we optimized the InAs thickness of the 2nd QD layer to obtain similar (resonantly) sized upper and lower QDs, where the thicknesses of the 1st/2nd InAs layers were 1.7/1.45 ML and the thickness of the partial cap layer was 3.5 nm. We prepared three samples whose barrier thicknesses were 3, 5, and 7 nm, with the aim of observing the barrier thickness dependence of the electronic structures in a CQD. Figure 5-10(a) shows the cross-sectional scanning transmission electron microscope (STEM) image of the CQD sample with d = 7 nm (the same as Fig. 4-20). We clearly confirmed the vertical alignment of two QDs in the image, where we estimated the dot height as ~3 nm and the effective thickness “d” of the barrier as ~7 nm, respectively. The dot diameter was also estimated as ~20 nm using a high-resolution scanning electron microscope (HRSEM). In addition, we fabricated an aluminum aperture mask (0.2–0.5 μmϕ) on the sample surface by an electron beam lithography technique, as mentioned in Section 4-5. Considering the low in-plane QD density, this mask

enables us to observe single CQD by selecting the aperture hole that shows the luminescence of only one CQD. In the macro-PL spectra, the luminescence peak from the QD ensemble ranged from 935 to 955 nm. We did not observe any energy splitting caused by wave function coupling in the macro-PL spectra because the QD ensemble had a large size distribution due to the thin InAs layer close to the critical thickness of the dot formation.

All micro-PL (μ-PL) and photoluminescence excitation (μ-PLE) measurements were performed using a microspectroscopy system similar to that shown in Fig. 4-9. We used a 1-m double monochromator and a cooled CCD detector with a spectral resolution of ~20 μeV. The excitation light focusing and the luminescence collection were performed using a microscope objective with a large numerical aperture (spot diameter ~4 μmϕ). The samples were cooled to 6 K in a liquid helium cryostat and a continuous-wave tunable Ti:sapphire laser was used as the excitation source.

5-2-2. Energy States around Ground Level

Typical μ-PL spectra from a single CQD are shown in Fig. 5-10(b), where the excitation energy was 1.41 eV (absorption band of WL) and the excitation intensity was set low enough (< 0.1 mW) to prevent multiple excitons from being excited. We also show the PL spectrum of a single QD layer sample as a reference at the top of the figure. As shown in Fig. 5-10(b), the overall trend of the CQD is that the spectra have two PL groups on the high and low energy sides, unlike the single QD which has only one group. Each PL group consists of two or three peaks that are separated by 2–5 meV, except for the d = 7 nm sample. The notable feature of the CQD is that the energy separation between the two PL groups increases with reductions in the barrier thicknesses, as indicated by ΔE in Fig. 5-10(b). This feature arises from the wave function coupling of electrons between the upper and lower QD and these PL groups constitute the bonding (X^+) and anti-bonding (X^-) states, respectively. The barrier thickness dependence of the energy splitting ΔE agrees well with previously reported results.[117,120] Of course, ΔE values may include the energy differences originating from the variations of characteristics between two QDs (size, location, strain *etc.*). But, in our observations, many CQDs in the different aperture hole areas show similar PL spectra and ΔE values, although the PL energies varied (1.285–1.350 eV) due to reflection of the inhomogeneity of the QD sizes. As seen in the inset in Fig. 5-10(b), the small data spread (fudge factor) of ΔE in our samples implies that the upper and lower QDs are of the similar (resonantly

growing) size in the analogous surrounding conditions. Here, increases in the data spread of ΔE with reductions in the barrier thickness seem to originate from increases in the thickness fluctuations with reductions in the barrier thicknesses because the barrier thickness is dominant element to affect the wave function coupling of electrons.[120]

Other feature of PL spectra is that the higher energy PL group (X^- state) maintains large PL intensity under the weak excitation conditions and has narrow line width as similar as X^+ PL group. This indicates that the carrier relaxation from X^- to X^+ state is suppressed. The energy relaxation of carriers under the weak exaction is mainly caused by the phonon emission. As is well known, the carrier relaxation rate induced by the acoustic phonons is ten times less than that by the optical phonons.[5] In our cases, the energy splitting ΔE are less than the longitudinal-optical (LO) phonon energy (~35 meV in InAs QDs): the acoustic phonons dominant the relaxation processes. Therefore, the long relaxation time from X^- to X^+ state due to the contribution of acoustic phonons to the relaxation processes, which is regarded as being longer than the exciton decay time, allows the strong PL intensity for the X^- state.

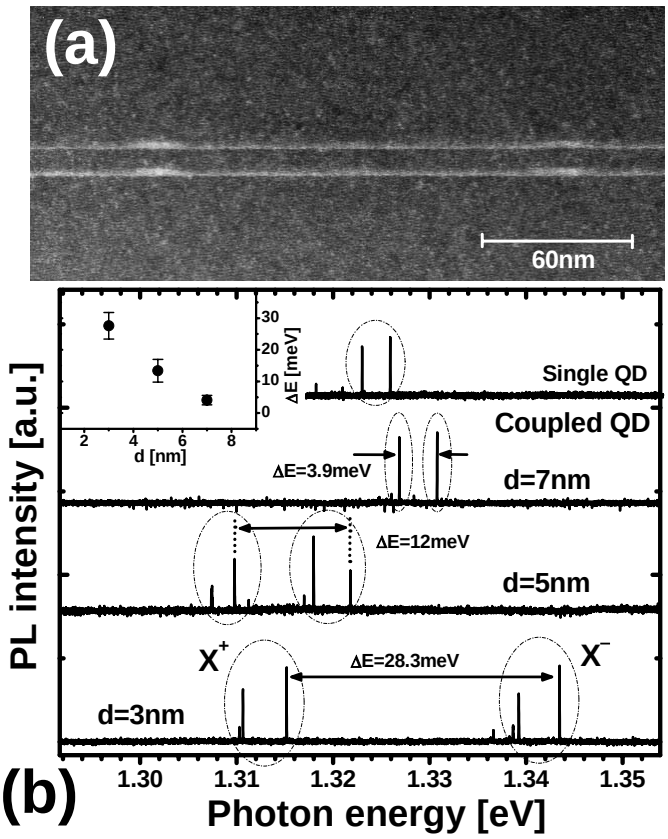

Fig. 5-10. (a) Cross-sectional STEM image of vertically coupled QDs (d=7nm). (b) μ-PL spectra of single CQD (pump: 1.41eV). The inset indicates a barrier thickness dependence of the energy difference ΔE between X^+ and X^- levels.

We shall now look more carefully at the multiple PL peaks of each PL group in our QDs. First, we will distinguish the emissions of exciton from those of multiple excitonic states by observing the excitation power dependence of the PL intensities. In the case of multiple excitonic states (biexciton *etc.*), the excitation power dependence will be out of linearly dependence on the excitation intensity.[55] In Fig. 5-11(a)–(d), we show the PL spectra under the low and high power

excitation conditions. We also shows the example of the excitation power dependence of the integral PL intensities in d = 3 nm CQD and the table in Fig. 5-11 presents the exponent "*m*" of all labeled PL peaks to the excitation power. At low excitation intensities, two peaks with a few meV energy separation dominate the one PL group (labeled X_1, X_2), where one peak dominates the PL group in the case of the d = 7 nm CQD. On the other hand, at high excitation intensities, extra peaks (labeled X_{XX} *etc.*) appear with lower energies than the X_1, X_2 peaks and exhibit a nonlinear dependence on the excitation intensities (m > 1), which indicates that these extra peaks originate from the multiple excitonic (biexciton-like) states (see the table in Fig. 5-11).

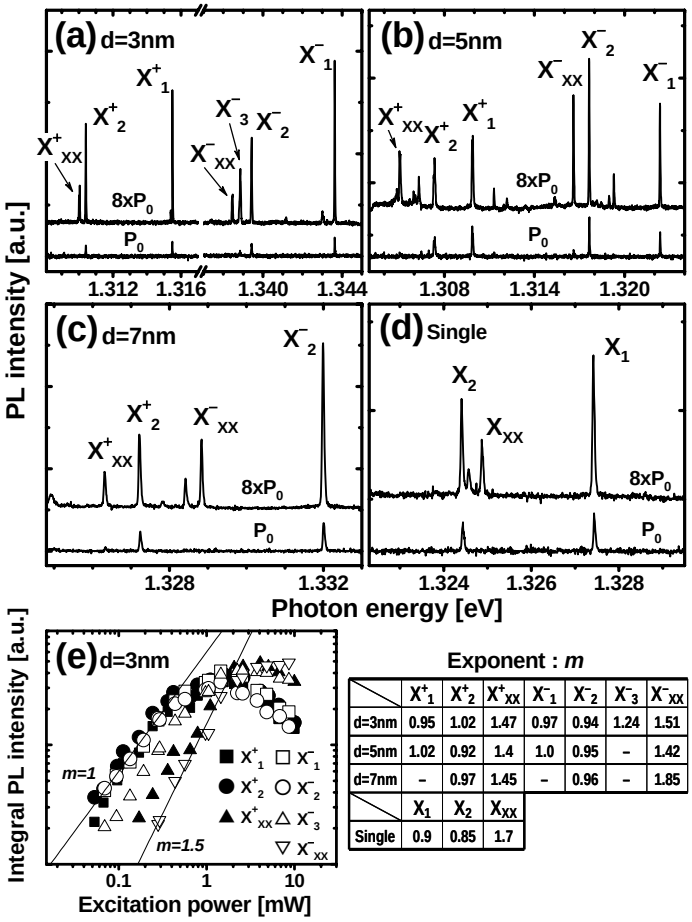

Fig. 5-11. Excitation power dependence of PL spectra (pump: 1.41eV). (a)-(d) PL spectra at the high/low excitation intensity. (e) Excitation power dependence of the integrated PL intensity in d=3nm CQD. Table: Exponent "*m*" to the excitation power of all labeled peaks.

Here, we focus on the two fundamental PL peaks (X_1 and X_2). These peaks exhibit a linear dependence on the excitation intensities (m ~ 1). This feature shows that the X_1 and X_2 peaks originate from exciton states rather than multiple excitonic states. Much the same is true for the single QD. The presence of the doublet PL peaks (X_1 and X_2) has possibilities of several origins: (1) Charged exciton (2) Different exciton states (involving a dark exciton) caused by the anisotropy of the QD shape (3) Asymmetric transition between an electron in one QD and a hole in the neighboring QD (4) Excited states of exciton. We shall consider these possibilities in order.

(1) Charged exciton:

Many previous studies indicate the existence of a charged exciton in In(Ga)As QDs[2755,121] and GaAs quantum disks.[122] As is well known, a negatively (positively) charged exciton shows a lower (higher) energy PL peak than a PL peak of a neutral exciton. Furthermore, it has been reported that a negatively charged exciton in an InAs QD[123] and a positively charged exciton in a GaAs quantum disk[122] had the polarization memory to circularly polarized right, unlike a neutral exciton which did not depend on circularly polarized right. Here, we show the circular polarization dependences of the PL spectra in our CQDs and a single QD in Fig. 5-12(a)–(d). As seen in the figures, the X_1 peak in all samples is strongly dependent on circularly polarized light. The X_1 peak, therefore, has possibility of a positively charged exciton because of the higher peak energy than the neutral exciton energy (X_2 peak). But, we need to be careful about the origin of extra carriers contributing to the charged exciton formation, which will be supplied from out of QDs or exist preliminarily in QDs. J. J. Finley *et al*. have reported that the PLE spectra of the positively charged exciton do not have peaks below the WL energy.[55] This suggests that the extra carriers contributing to the charged exciton formation are not excited under the excitation condition of lower energy than the WL energy; this condition leads to create only one pair of an electron and a hole. In other words, in this case, the extra carriers contributing to the charged exciton formation were supplies

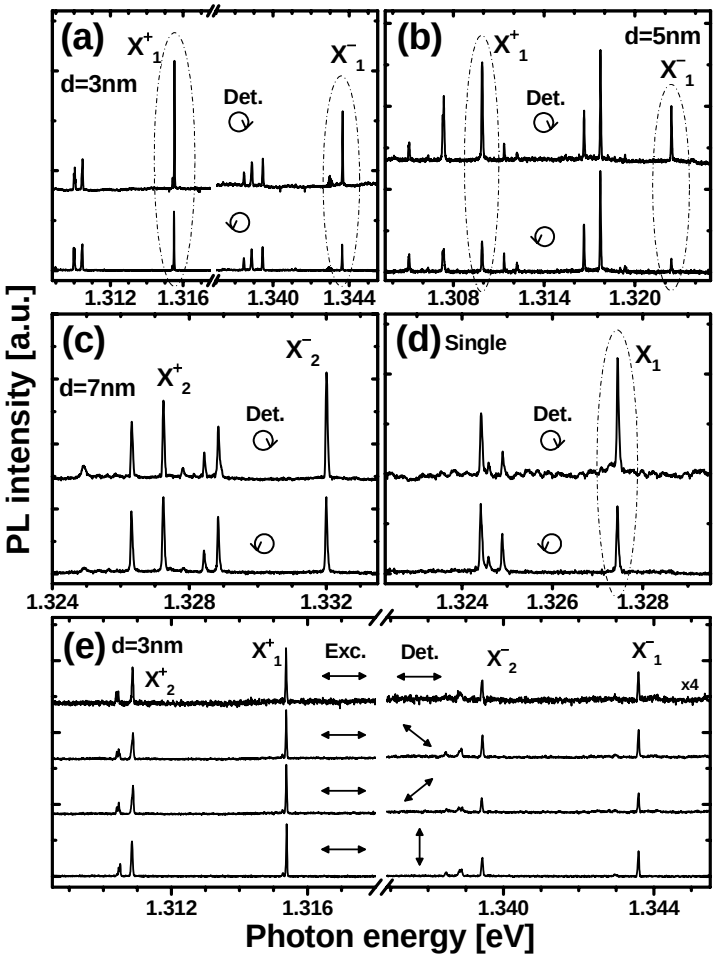

Fig. 5-12. PL spectra under the polarized light excitation.
(a)-(d) PL spectra under the circularly light excitation. The polarization of the excitation light is clockwise and the polarization of the PL detection is both clockwise and anticlockwise. (e) Dependence of the PL spectra on linearly polarized light in d=3nm CQD. Excitation energy was 1.41eV in all spectra.

from out of a QD. L. Besombes *et al*. have also reported that the PLE spectra of the positively charged exciton do not have peaks around the WL energy.[27] This suggests that the carriers originating from background doping, which contribute to the charged exciton formation, are compensated by the extra carriers dissociating from excitons in the WL. In other words, in this case, the extra carriers contributing to the charged exciton formation exist preliminarily in a QD. However, in our cases, the structure of X_1 PLE spectra (see Fig. 5-13–14) has many peaks at the overall excitation energy and we confirmed that the X_1 peak maintains it's intensity at the WL excitation (Fig. 5-10–12) and the interband excitation (1.55 eV), conflicting with the results of previous works about the charged exciton. These observations suggest that the X_1 peak does not originate from extra carriers. Therefore, a charged exciton does not explain our observations.

(2) Different exciton states (involving a dark exciton) due to the QD shape:

The doublet exciton states in a QD have been discussed theoretically[46,124,125] and have been observed experimentally.[126,127] This doublet structure with 0.01–1 meV scale energy splitting is considered to be results of an activation of the "bright" exciton mixing with the "dark" exciton through the exchange interaction caused by the anisotropy of the QD shape or magnetic field induced. Furthermore, it has been reported that these doublet peaks depend on linearly polarized light, because of the origin of the QD shape anisotropy.[124,126] Now, we show the linear polarization dependences of the PL spectra in our d = 3 nm CQD in Fig. 5-12(e). As seen in the figure, the ratios between the X_1 and X_2 PL intensities are almost same. This result indicates that the X_1 and X_2 peaks do not relate to the QD shape anisotropy. Therefore, the possibility given here can not explain our observations. Intrinsically, the splitting energy between the X_1 and X_2 peaks (1–5 meV) is too large to be explained by the exchange interaction.

(3) Asymmetric transition between an electron in one QD and a hole in the neighbor QD:

It has been suggested that an electron of the coupling levels (bonding and anti-bonding states) in a CQD has possibility to recombine severally with each hole in two QDs because a hole is isolated in each QD due to its large effective mass.[120] This prediction indicates multiple PL peaks in a PL spectrum of a single CQD. In this case, it seems to be roughly expected that the energy separation between two peaks (X_1, X_2) will be same in both two PL groups (X^+, X^-) because the energies of holes in each QD stay constant. But, in our observation, the energy separations between the X_1 and X_2 peaks are all different in each PL group of every CQDs. Furthermore, the fact that the single QD

also has double PL lines conflicts with this prediction, because a single QD would have a single PL line if this prediction was true. In addition, this prediction does not explain the circular polarization memory of the X_1 peaks. Therefore, the asymmetric transition can not explain our observations.

(4) Excited states of exciton:

Thus, the possibilities of (1)–(3) mentioned above can not explain our observation. When we focus on the circular polarization memory of the X_1 peaks, this feature implies that the X_1 states have a nonzero quantum number; it means that the X_1 states will be excited states of a neutral exciton. Many hole bound states with a close energy level separation of a few meV in a QD were expected on the basis of theoretical calculations[45] and were reported experimentally,[128] in contrast to the electron bound states with a large energy separation more than several tens meV. Therefore, considering the result of the circular polarization memory, we think that the X_1 peak seems to originate from the *p*-like hole excited state in the exciton consisting of the coupling levels. In contrast, the X_2 peak, which has a zero quantum number on the basis of its lack of dependence on circularly polarized light, seems to originate from the *s*-like ground state. Furthermore, the X_1 peak is thought to be stable and to have a long relaxation time for relaxation to the ground X_2 states based on the large PL intensity.

Here, we note that d = 7 nm CQD has only *s*-like X_2 peak which is independent on circularly polarized light [Fig. 5-12(c)], whereas single QD has both X_1 and X_2 peaks [Fig. 5-12(d)]. Although it is currently unclear why the d = 7 nm CQD does not have an *p*-like X_1 peak, we consider this may be because the X_1 state is forbidden as a result of the strain distribution of d = 7 nm CQD being different from those of other samples. At any rate, comparison of PLE spectra enables us to confirm more clear origin whether two PL peaks originate from same QD (single QD) or different QDs (d = 7 nm CQD). The details will be mentioned in the next section.

5-2-3. Electronic Structures at Higher Energy States

Next, we discuss the higher excited states of CQDs using the results of photoluminescence excitation (PLE) measurements. The electronic structures at the higher energy states will inform us about the carrier transfer between two QDs through the electron wave function coupling of the excited levels. Moreover, we will also identify the origin of the emission more clearly by means of comparing the peak energy correspondence between PLE spectra. In Fig. 5-13–14, we present the

PLE spectra of a single CQD with various barrier thicknesses and a single QD. We can see two general characteristics in the figure. One is that the PLE spectra of the two PL peaks (X_1, X_2) in one PL group have many coincident peaks as indicated by the dotted line. Another is that there are several coincident PLE peaks between the two PL groups (between the X^+ and X^- states) as indicated by the dashed line but other peaks are inherent to each group.

The former characteristic, the existence of many coincident PLE peaks in one PL group (between X_1 and X_2), indicates that these two peaks originate from the same excited level series, which means that the X_1 peak is the excited level of the X_2 state in a group. In the single QD [Fig. 5-14(b)], we also observed same feature, which indicates the pair PL lines (X_1 , X_2) originating from same QD. These observations support our suggestion in the previous section that the X_1 state is the *p*-like hole excited state. In contrast, in the case of d = 7 nm CQD [Fig. 5-14(a)], the PLE spectra of two PL peaks (X^+_2, X^-_2) are not correspondent, which means that these peaks originate from different QD in d = 7 nm CQD each other. Thus, comparison of PLE spectra enables us to identify the origin of the emission.

On the other hand, the latter characteristic, the coexistence of both the coincident PLE peaks between the two PL groups and the inherent peaks to each group, indicates the coexistence of two different excited level series in the electronic structure of our CQDs, which are the common excited level series between the X^+ and X^- levels and the individual excited level series for each state. In these

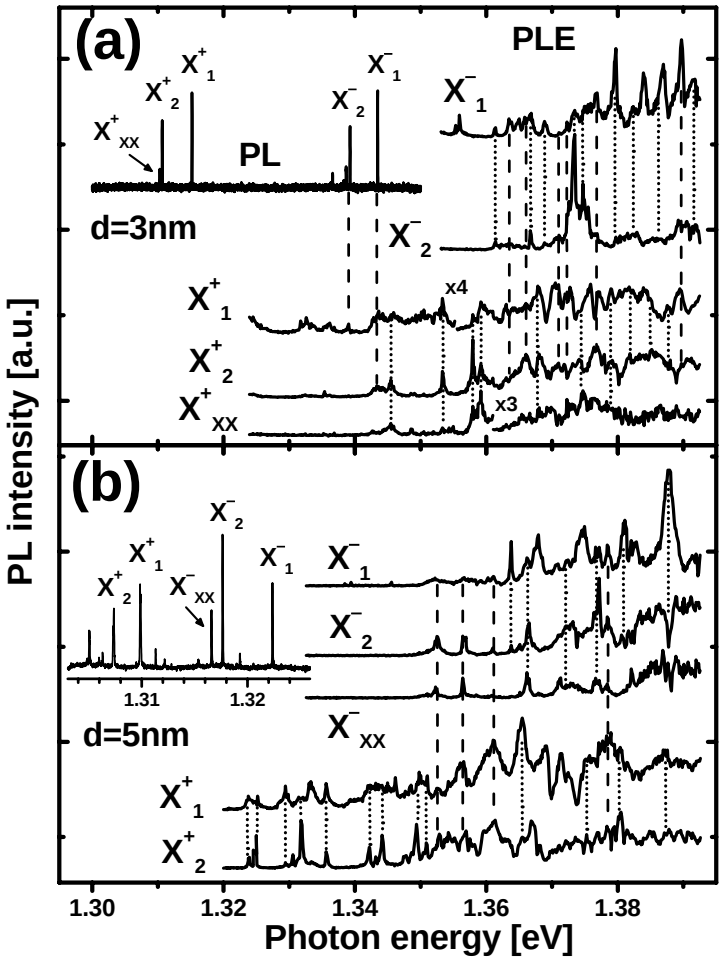

Fig. 5-13. PLE spectra in a CQD (a) d = 3 nm, (b) d = 5 nm.

two excited level series, the individual excited level series is considered to originate from the hole excited states. As mentioned above, many hole bound states with a close energy level separation of a few meV are existing in a QD.[28,29] Because of a large effective mass of the hole, the hole wave functions will not couple with the neighboring QD. Therefore, the energy levels related to the hole excited states should be observed as individual excited level series for each PL group (each coupling level of X^+ and X^-). On the contrary, the electron wave function coupling between two QDs will induce the common excited levels between the X^+ and X^- states. The number of the common excited levels should change with the coupling strength between two QDs; for examples, the strong wave function coupling will result in many common excited levels due to increasing of the number of the electron excited states coupling with the neighboring QD (the level sharing between the X^+ and X^- states), which means enhancement of the carrier transfer between two QDs. This prediction can be seen in Fig. 5-13–14. Comparing the PLE spectra of CQDs with various barrier thicknesses, the number of the common PLE peaks between the X^+ and X^- states increases with reductions of the barrier thicknesses as indicated by the dashed line. This observation directly shows that the level sharing between the X^+ and X^- states and the carrier transfer between two QDs are enhanced with reductions of the barrier thickness due to the wave function coupling of the excited levels.

Thus, we observed the common excited levels due to the level sharing between the electron

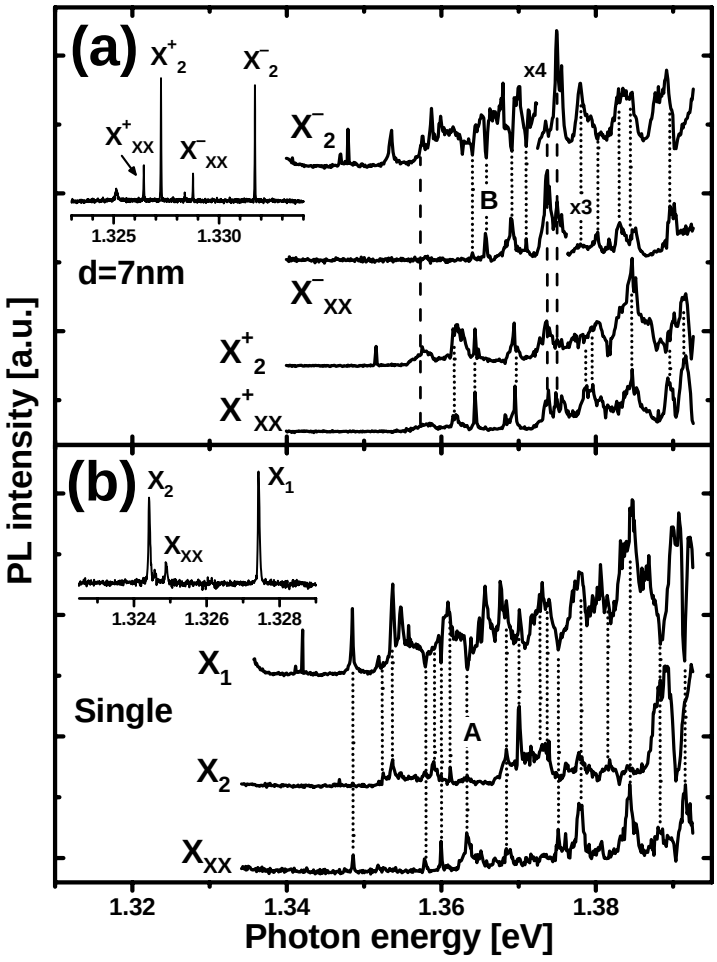

Fig. 5-14. PLE spectra in a CQD and single QD. (a) d = 7 nm CQD (b) single QD.

excited states and the individual excited levels originating from the hole excited states in a CQD system. From these results, we can roughly classify d = 3, 5 nm CQDs into the quantum mechanical coupling system (strong coupling region), in which the wave function coupling and the carrier transfer are large, and d = 7 nm CQD into the electromagnetic coupling system (weak coupling region), in which the wave function coupling and the carrier transfer are very small and the electromagnetic interaction will be dominant.

5-2-4. Carrier Relaxation in CQD System

Additionally, we will mention the carrier relaxation in a CQD system. Gotoh *et al.* discussed the quantum resonance, namely the Fano resonance, in a single QD.[129] They suggested that an exciton shows the Fano resonance with a biexciton because the difference in the relaxation path between the exciton and the biexciton yields the phase difference of the coherent dipole as long as the exciton and the biexciton maintain its coherence (Fig. 5-15). Further, they showed its experimental evidences in a single QD in which the PLE spectra of the exciton showed dip structure caused by the existence of the biexciton. We observed same features in the PLE spectra of our QDs. In Fig. 5-13–14, we also show the PLE spectra of the biexciton-like states (labeled as X_{XX}). With the single QD and d = 7 nm CQD, there are dip structures in the X_1 PLE spectra at an energy corresponding to the peaks in the PLE spectra of the X_{XX} states, for example, peaks A and B in the figures (the detail spectra are shown in Fig. 5-16). This phenomenon suggests that there is Fano resonance between the $X_{1,2}$ and X_{XX} states in our QD as discussed in Ref. 129.

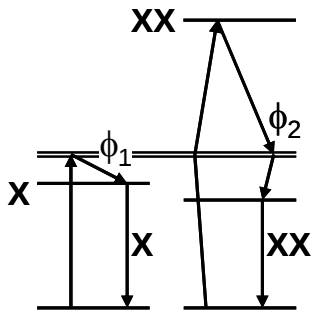

Fig. 5-15. Fano resonance in a QD proposed by H. Gotoh *et al.*.

This expression of the quantum resonance will enable us to monitor the coherence of the carrier relaxation in a CQD. The strong wave function coupling will induce many fine energy structures because of the exchange interaction among electrons and holes. Then, the complexity of the relaxation process originating from the mixed energy structures should dissipate the carrier coherence and eliminate the quantum resonance because of the carrier–phonon interaction which is main rule of the carrier relaxation. This prediction can be seen in our observation. The reductions in the barrier thicknesses leads many weak PLE peaks which blur boundaries between neighboring

peaks and yield quasi-continuum band (Fig. 5-13–14). This suggests that the strong wave function coupling induces many mixing energy states. And, in the single QD and d = 7 nm CQD which are a non-coupling and a weak coupling system, there are dip structures in the $X_{1,2}$ PLE spectra at an energy corresponding to the PLE peaks of the X_{XX} states; it indicates the existence of the quantum resonance. On the contrary, in the d = 5 and 3 nm CQDs which are strong coupling system, the dip structures do not appear in the $X_{1,2}$ PLE spectra; it indicates the nonexistence of the quantum resonance. This observation directly shows that the complexity of the energy states in a strong CQD system has an important influence on the decoherence of the carrier relaxation process. Therefore, we must be careful when choosing the energy states if a CQD system with quantum mechanical coupling is used for applications involving the use of coherence.

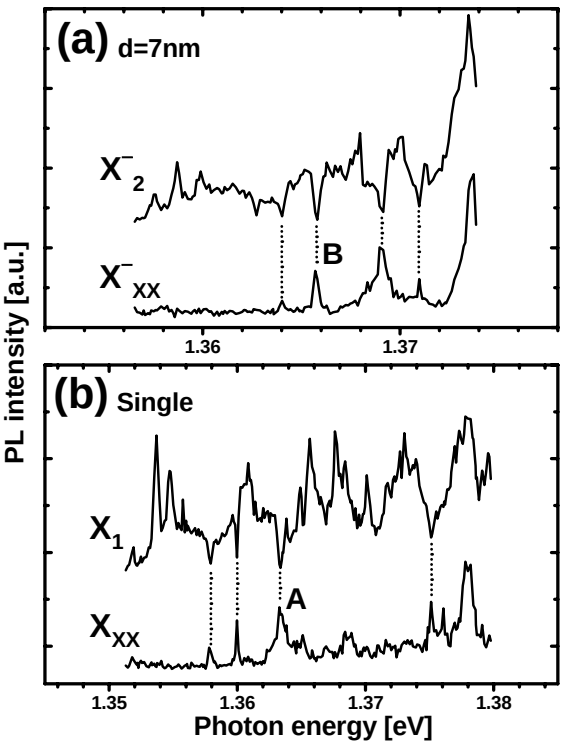

Fig. 5-16. Expanded PLE spectra.
(a) d=7nm CQDs. (b) single QD. The dotted line indicates the levels causing the Fano resonance between the X_1 and X_{XX} states.

5-2-5. Conclusion

The electronic structures in a single InAs/GaAs CQD have been discussed. We observed the bonding and anti-bonding states due to the electron wave function coupling in the PL spectra, in which the strength variation of the quantum mechanical coupling with different barrier thicknesses was confirmed. We also discussed the origin of the multiple PL peaks and suggested the contribution of the hole excited states to the emissions in the QDs. On the basis of PLE measurements, we showed the electronic structures of a CQD system in higher energy states. We confirmed the common excited levels due to level sharing between the electron excited states and the individual excited levels originating from the hole excited states in a CQD system. From this result, we classified d = 3, 5 nm CQDs into the quantum mechanical coupling system (strong coupling region) and d = 7 nm CQD into the electromagnetic coupling system (weak coupling

region). Moreover, we implied the influence of strong wave function coupling on the decoherence of the carrier relaxation processes in single CQD.

5-3. Interdot Interactions in a Strongly Coupled Quantum Dot *~Formation of Exciton Molecule~*

In the previous section, we showed the characteristics of electronic structures in a single CQD. It was shown that d = 3, 5 nm CQDs were classified into the quantum mechanical coupling system and d = 7 nm CQD was classified into the electromagnetic coupling system. In this section, we focus on the interdot interaction in a strongly (quantum mechanically) CQD with d = 3 nm. We discuss the inter-exciton interaction in a CQD by means of the two-color excitation technique.

5-3-1. Samples and Experimental Setup

The sample used in this section was the same as that used for d = 3 nm CQDs presented in Fig. 5-10(b). The experimental set-up was also the same as that in the previous section, in which a 1-m double monochromator and a cooled CCD detector were used. The samples were cooled to 6 K in a liquid helium cryostat, and two continuous-wave tunable Ti:sapphire lasers were used as excitation sources in the two-color PLE measurement.

5-3-2. Results and Discussion

We replot the PL/PLE spectra of the d = 3 nm single CQD in Fig. 5-17. As discussed in the previous section, the PLE spectra show common excited levels and individual excited levels between the bonding (X^+) and the anti-bonding (X^-) states. In this section, we focus on the latter: the individual excited levels for each coupling state. These individual excited level series enable us to excite the X^+ and X^- states individually. Using this characteristic, we attempted to observe the inter-exciton interaction between bonding levels in a strongly CQD system.

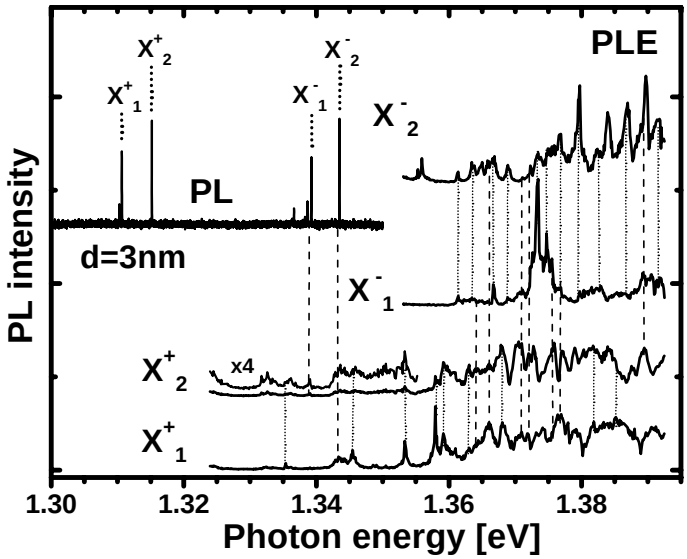

Fig. 5-17. PL/PLE spectra of d=3nm CQD.

For this purpose, we proposed the differential PLE (DPLE) spectroscopy. The measurement procedure is described in Fig. 5-18(a). To begin with, we measure the one-color PLE spectra of both the X^+ and X^- states, and we select the energy level in the X^+ PLE spectrum whose energy does not respond to the X^- state, as indicated by "Pump" in the figure. Tuning the wavelength of the pump light source at this energy makes it possible for us to create carriers constantly only in the X^+ state. Then, we measure the PLE spectrum of the X^- state excited by the probe light source *with* or *without* pumping the X^+. Finally, we obtain the DPLE spectrum of the X^- state in a reflection of the X^+ carrier creation by subtraction between the two PLE spectra of the X^- state.

In the top of Figure 5-18(b), we show the DPLE spectrum of the X^-_1 state. Here, the X^+_1 state was stationary excited by the pump excitation source whose energy was fixed at the E_{pum} energy in the figure. This E_{pum} energy is in the zero absorption range of the X^-_1 state and excites only the X^+_1 state. The DPLE spectrum of the X^-_1 state was obtained by subtraction between the one-color PLE spectrum (without pump) and the two-color PLE spectrum (with pump) which are shown in the middle of figure. As shown in Fig. 5-18(b), the remarkable feature of the DPLE spectrum is the existence of the X^-_1 luminescence suppression at the X^-_1 excited states.

We also show PL spectra under the two-color excitation condition in Fig. 5-19(a), where X^+_1 and X^-_1 were excited at E_{pum} and E_A energies, respectively. In the X^+ group spectra, the carrier creation in X^-_1 (two-color excitation) induces dramatic PL increment of the XX^{+-} peak, which is located at a lower energy than X^+_1, in contrast to almost the same PL intensities of X^+_1 and X^+_2 peaks. On the other hand, in the X^- group spectra, the carrier creation in X^+_1 (two-color excitation)

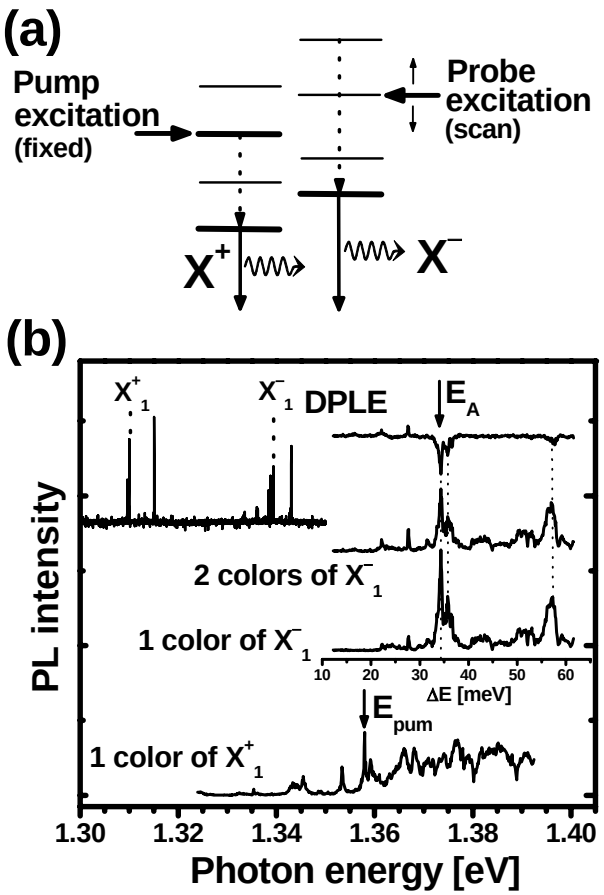

Fig. 5-18. (a) Observation scheme of carrier correlation. (b) 1-color, 2-color and differential PLE spectra in d=3nm CQD.

induces noticeable PL decrement of the X^-_1 peak. These features are more clearly presented in the excitation power dependence of PL intensities described in Fig. 5-19(b), where X^-_1 was constantly excited at E_A and the excitation intensity for X^+_1 was changed at E_{pum} energy. Significantly, in the two-color excitation condition, the X^+_1 excitation (E_{pum}) induces only the XX^{+-} increment in spite of the prompt saturation of X^+_1/X^+_2 peaks. At the same time, more remarkably, it induces the decrement of the X^-_1 emission, antisymmetrically to the XX^{+-} increment. These features demonstrate that X^-_1 carriers contribute to XX^{+-} formation. Of course, X^+_1 surely contributes to XX^{+-} formation. In other words, the XX^{+-} peak consists of both X^+_1 and X^-_1 states.

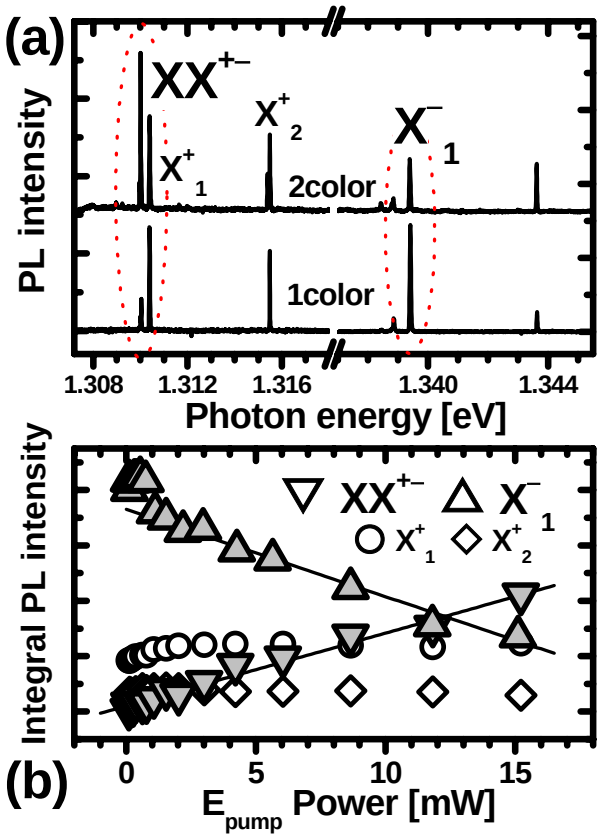

Fig. 5-19. (a) PL spectra under the 1-color/2-color excitation condition, where X^+_1 and X^-_1 were excited at E_{pum} and E_A respectively. (b) Integral PL intensity as a function of excitation power of E_{pum} under the 2-color excitation.

Essentially, the bonding (X^+) and anti-bonding (X^-) states in a quantum mechanical CQD will constitute a quasi-biexcitonic state, called "exciton molecule," caused by the interaction between them. This formation corresponds to the $X_1X_2-\Delta E$ state in Fig. 3-6. Our observations in Fig. 5-19 precisely show that the XX^{+-} peak originates from an exciton-molecule. What is more noteworthy is that X^-_1 carriers are inductively expended to form exciton molecules under the existence of X^+_1 carriers.

Next, let us examine the detailed PL spectra of the X^+ group. In truth, the biexciton of X^+_1 itself (called "self-biexciton") is observed at an energy close to the XX^{+-} peak. Figure 5-20 shows the PL spectra of the X^+ group with various E_{pum} excitation intensities: (a) with X^-_1 excitation at the E_A energy (b) without X^-_1 excitation. As can be seen in figure (b), when X^-_1 is not excited, the self-biexciton of X^+_1 (XX^+_1) is dominantly emitted with an increment of excitation intensity, and

the intensity of X^{+}_{1} also increases. In contrast, when X^{-}_{1} is excited [figure (a)], the exciton molecule (XX^{+-}_{1}) is dominantly emitted, and furthermore, X^{+}_{1} and XX^{+}_{1} hardly increase. This observation demonstrates that the X^{+}_{1} carrier is also expended inductively to form exciton molecules under the existence of X^{-}_{1} carriers.

Here, we consider the biexciton formation yield "γ" on the basis of the excitation power dependence of PL intensity, $I = \gamma \times P$, where I and P are a PL and an excitation intensity, respectively (Fig. 5-21). The original yield of self-biexciton γ^{+}_{1} is estimated at 1.96 from the PL intensity in the one-color excitation condition [filled triangle in Fig. 5-20(c)]. On the other hand, the estimated yield of exciton molecules in two-color excitation (γ^{+-}) is larger than γ^{+}_{1} (open triangle). This result shows that the X^{+}_{1} carrier forms an exciton molecule more inductively than the self-biexciton formation. In our two-color excitation condition, we estimated that the yield of exciton molecules was 1.7 ($\gamma^{+-}/\gamma^{+}_{2}$ = 2.68/1.57) times larger than that of self-biexciton. We note that the yield of exciton molecules depends on the excitation rate of X^{-}_{1} carriers because the exciton molecule formation depends on the coexistence rate of both X^{+} and X^{-}_{1} per unit time. At any rate, both X^{+} and X^{-} carriers preferentially contribute to the formation of exciton molecules.

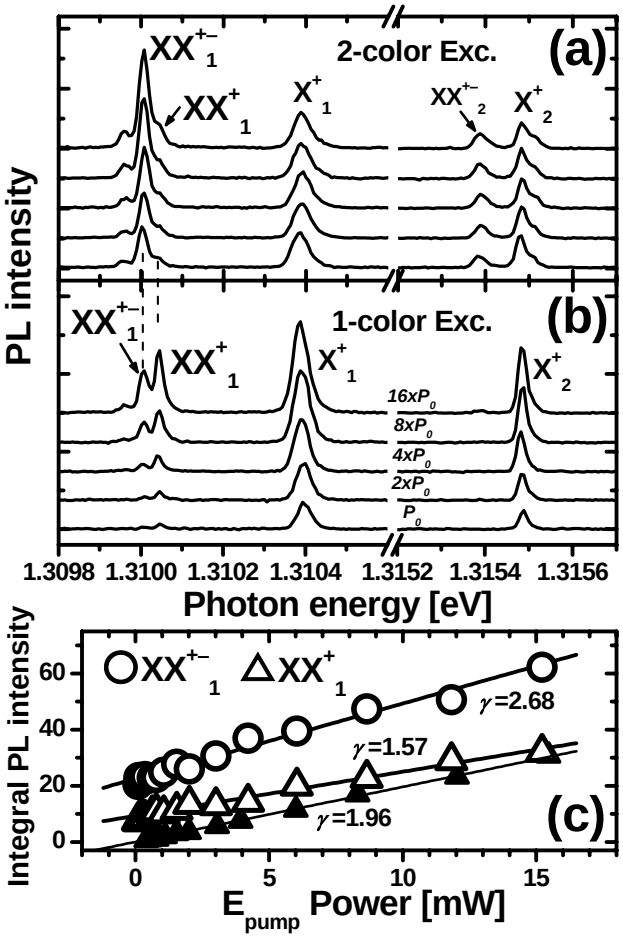

Fig. 5-20. (a-b). Excitation intensity dependence of X^{+} PL group: (a) with (b) without X^{-}_{1} excitation, where X^{+}_{1} and X^{-}_{1} were excited at E_{pum} and E_A respectively. (c). Integral PL intensities of exciton molecule (XX^{+-}_{1}) and self-biexciton (XX^{+}_{1}) as a function of excitation intensity of E_{pum} under the 2-color excitation [the condition of figure (a)]. Filled triangle indicates XX^{+}_{1} intensity under the 1-color excitation. Solid lines indicate linear fitting.

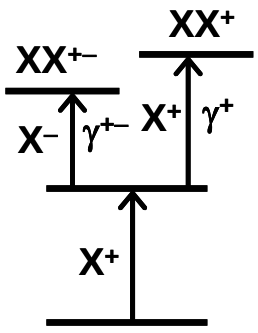

Fig. 5-21. Biexciton formation yield.

Putting it all together, the above processes are schematically shown in Fig. 5-22. In the one-color excitation condition [figure (a)], the photo excited carrier in the X^- excited level is preferentially expended on X^- exciton emission because X^- carriers cannot form an exciton molecule because of the non-existence of X^+ carriers. This case is common to the one-color PLE spectrum of X^-_1 in Fig. 5-18(b) and the PL spectra in Fig. 5-20(b). On the other hand, in the two-color excitation condition [Fig. 5-22 (b)], the existence of both X^+ and X^- carriers induces inductive formation of an exciton molecule that results in the dominant emission of XX^{+-} [Fig. 5-19, 5-20(a)], the dip structures in the DPLE spectrum in Fig. 5-18(b), and the decrement of X^-_1 intensity in Fig. 5-19(b).

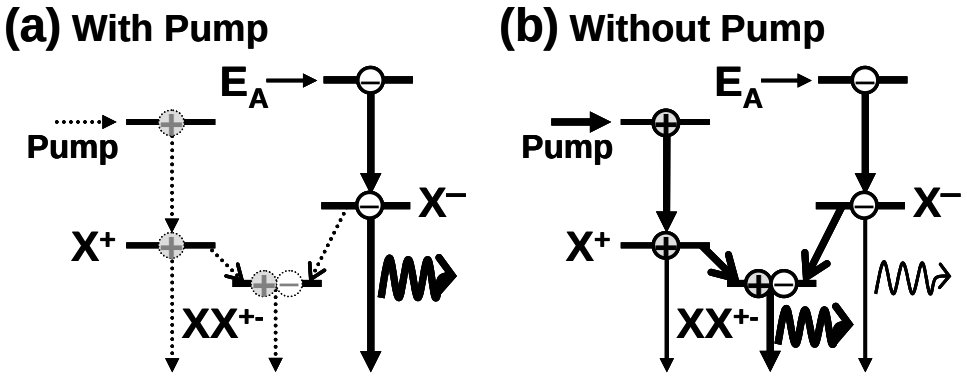

Fig. 5-22. Schematic drawing of inductive exciton-molecule formation in strongly CQDs. (a) Mono-excitation. (b) Co-excitation.

5-3-3. Conclusion

We discussed the inter-exciton interaction between bonding levels in a strongly CQD. The unique excited levels of X^+/X^- bonding states enabled us to excite the X^+ states individually. Analysis of the differential PLE spectrum and the two-color excitation PL spectra demonstrated the inductive formation of an exciton molecule consisting of both X^+ and X^- states due to strong quantum mechanical coupling. The formation yield of exciton molecules is 1.7 times larger than that of self-biexciton in our excitation condition. These results and discussion offer new possibilities to expand the design flexibilities of quantum logic devices using coupled QD systems.

5-4. Interdot Interactions in an Intermediate Coupled Quantum Dot *~Formation of Exciton Molecule~*

In the previous section, we considered the interdot interactions in a strongly (quantum mechanically) CQD system. We showed that both bonding (X^+) and anti-bonding (X^-) states contributed inductively to form an exciton molecule originating from the quantum mechanical coupling. However, it was not possible to perform absolute separated excitation of the X^+/X^- states because of the large energy separation between these states originating from the strong quantum coupling. This situation made it difficult for us to simply observe the inter-carrier interaction in a CQD. In this section, the subject of the experiments is the d = 5 nm CQD, in which the energy separation between the bonding states is smaller than that in d = 3 nm CQD due to the intermediate coupling strength. This condition in the d = 5 nm CQD will enable us to produce an individual excitation of the X^+/X^- states and a distinct observation of the inter-exciton interaction in a CQD.

5-4-1. Samples and Experimental Setup

The sample used in this section is the same as that in Section 5-2. The experimental set-up is also the same as that in the previous section, in which a 1-m double monochromator and a cooled CCD detector were used. The samples were cooled to 6 K in a liquid helium cryostat and two continuous-wave tunable Ti:sapphire lasers were used as excitation sources in the two-color PLE measurement.

5-4-2. Results and Discussion

In the previous section, we showed the formation of an exciton molecule consisting of both bonding (X^+) and anti-bonding (X^-) states. In d = 5 nm CQD (intermediate coupling), the quantum mechanical coupling is comparatively available, and consequently, there is the possibility that coupling X^+ with X^- causes formation of an exciton molecule even in d = 5 nm CQD.

Figure 5-23(a) presents the PL and PLE spectra of d = 5 nm single CQD used in this section; here, this CQD is different from that presented in Section 5-2 (different aperture hole). As shown in the figure, this CQD shows the energy separation between X^+/X^- states of ΔE = 17.5 meV. With careful selection, we could find CQDs whose coupling levels were individually excited, although the

sharing excited levels between X^+/X^- were observed. In Fig. 5-23(a), X^+/X^- states can be separately excited at the E^+/E^- levels that originate from the hole excited states as mentioned in Section 5-3. Thus, the energy difference of the excited states between X^+ and X^- makes it possible to individually control the creation of an exciton in each bonding state.

The co-creation of X^+ and X^- carriers by means of two-color excitation yields an interaction between X^+/X^- states. In Fig. 5-23(b), we present the PL spectra under individual or simultaneous excitation conditions. The excitation at the E^+ (E^-) energy yielded only an X^+ (X^-) emission as shown in the center (bottom) of the figure. However, when the X^+ and X^- states were excited simultaneously [two-color (E^+/E^-) excitation], a new peak appeared on the lower energy side than the X^+_1 peak (labeled XX^{+-} at the top of the figure). This observation indicates the formation of an exciton molecule consisting of X^+ and X^- states in a d = 3 nm CQD as shown in the previous section.

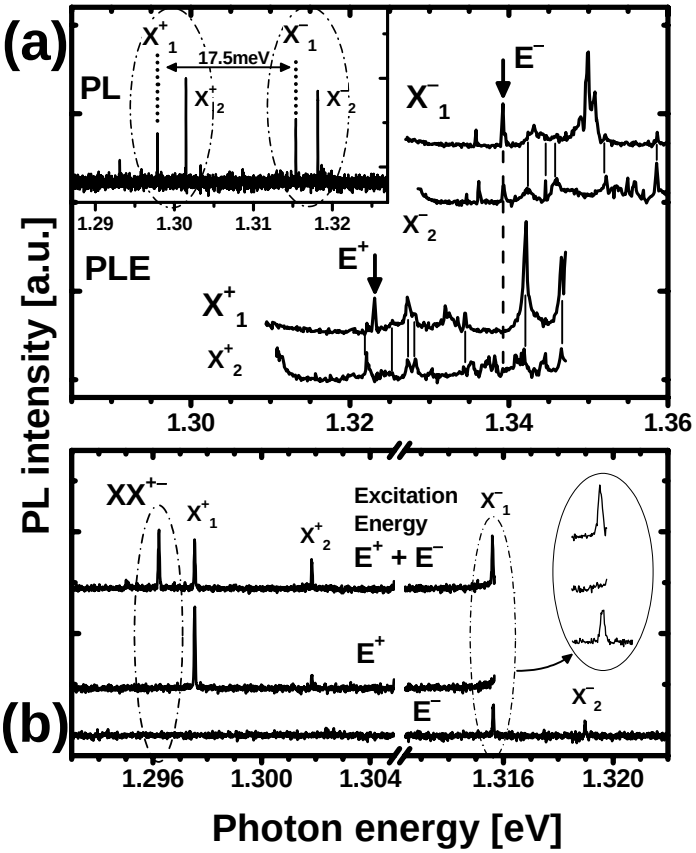

Fig. 5-23. (a) PL/PLE spectra of d=5nm CQD. The inset indicates the PL spectrum under WL excitation. (b) PL spectra under the 1-color/2-color excitation (E^+/E^-). XX^{+-} indicates the exciton molecule.

To rule out the possibility that XX^{+-} peak attributed to self-biexciton of X^+, we check the excitation power dependence on PL intensity of all multiple exciton peaks. Firstly, we examined the one-color excitation power dependence of the PL intensities as presented in Fig. 5-24(a), where the excitation laser energy was fixed at wetting layer energy. At high excitation density, the four new peaks (XX^{+-}, XX^+_2, XX^-_1, XX^-_2) were appeared at lower energy side of each fundamental peak (X^+_1, X^+_2, X^-_1, X^-_2). The excitation power dependence of these four peaks exhibits the quadratic dependence on excitation power, which imply that two excitons contribute to form these new peak. From this result, there are two possibility that new peak XX^{+-} is due to the biexciton of X^+_1 exciton

itself or an exciton molecule consisting of two different exctions.

If the XX^{+-} originates from the self-biexiciton of the X^{+}_{1}, the PL intensity of XX^{+-} should strongly depend on only the E^{+} excitation, while if the XX^{+-} originates from an exciton molecule, the PL intensity of XX^{+-} should depend on both E^{-} and E^{+} excitation. Consequently, we measured the two-color excitation power dependence of the XX^{+-} PL intensity, as shown in Fig. 5-24(b), where the two-color excitation energies were fixed at E^{+} and E^{-}. As seen in the figure, the XX^{+-} PL intensity depends on both E^{-} and E^{+} excitation, which reveals that XX^{+-} originates from an exciton molecule consisting of the X^{+}/X^{-} states.

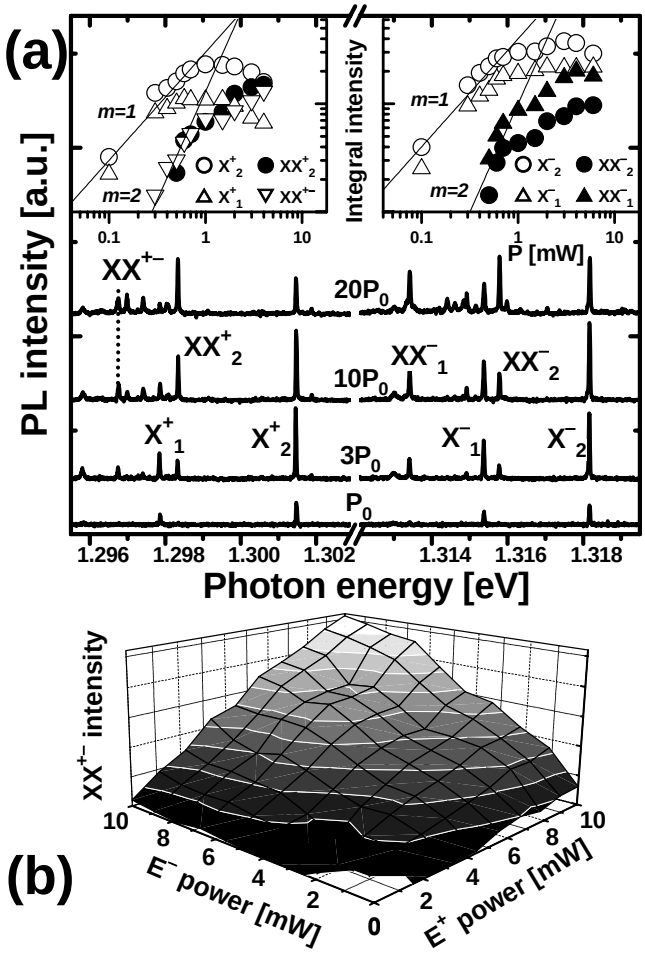

Fig. 5-24. Excitation power dependence of PL spectra. (a) 1-color excitation condition (WL excitation). (b) Integral PL intensity of XX^{+-} peak under 2-color excitation (E^{+}/E^{-}).

Furthermore, we will show another evidence for the existence of an exciton molecule by undertaking a two-color PLE measurement, as mentioned in the previous section. If the exciton molecule originates from both the X^{+} and X^{-} states, the X^{+} exciton should always contribute to the formation of an exciton molecule regardless of which higher energy levels of X^{+} are excited. The measurement procedure is as follows [see Fig. 5-25(a)]. To begin with, the energy of the pump light source is fixed at the excited state of X^{-}, which is excited constantly, as indicated by "Pump" in the figure. Then, X^{+} is excited by a 2^{nd} probe light source whose energy is scanned for the PLE measurement. We measure the PLE spectra of the XX^{+-} peak with the pump (two-color PLE) and the X^{+} peak without the pump (one-color PLE), and finally we confirm which X^{+} levels contribute to the XX^{+-} emission by comparing the PLE spectra of the XX^{+-} and X^{+} states.

The measurement results are presented in Fig. 5-25(b), where the X^{-} states was constantly excited

at E^{-}_{pump} energy indicated in the figure. The two-color PLE peaks of the XX^{+-} state (at the top of the figure) nearly coincide with the one-color PLE peaks of X^{+}_{1} (second from the bottom in the figure) as indicated by dotted lines. This result shows that the X^{+} exciton is certain to contribute to the XX^{+-} emission in the excited state of X^{+}. Thus, we show evidence for the formation of an exciton molecule consisting of X^{+} and X^{-} excitons in an intermediate CQD system.

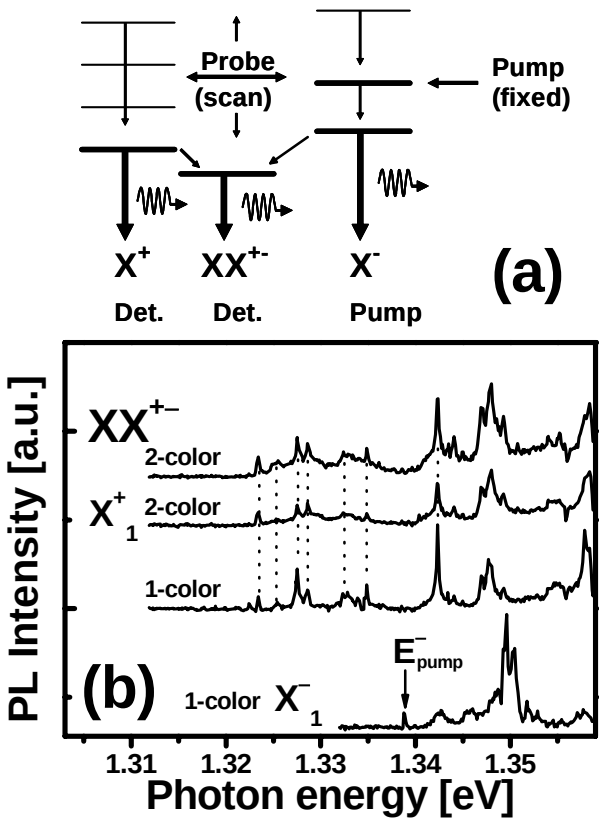

Fig. 5-25. (a) 2-color excitation experiment. (b) PLE spectra under 1-color/2-color excitation.

Now, let us briefly mention the binding energy of an exciton molecule (between excitons). Figure 5-26 shows the binding energies of an exciton molecule in d = 3, 5 nm CQDs and the self-biexciton in d = 3 nm CQD (see the previous section). As shown in the figure, the binding energy of the exciton molecule is larger than that of the self-biexciton, and also increases with increments in the barrier thickness. Here, an exciton is analogous to a hydrogen atom, consequently we can assume that the interaction between excitons is analogous to a hydrogen molecule.[130] When the inter-exciton distance is close to the Bohr radius, the repulsive force between exctions may make the system energy large; that is, the binding energy between excitons will be reduced. In our QD system, the QD size (~20 nm) is smaller than the exciton Bohr radius (36.8 nm in bulk). Therefore, the binding energy between excitons seems to be smaller than the value at the minimum system energy. In this condition, losing the inter-carrier distance will reduce the system energy rapidly. In our CQDs, the carrier occupation in different bonding levels (X^{+}, X^{-})

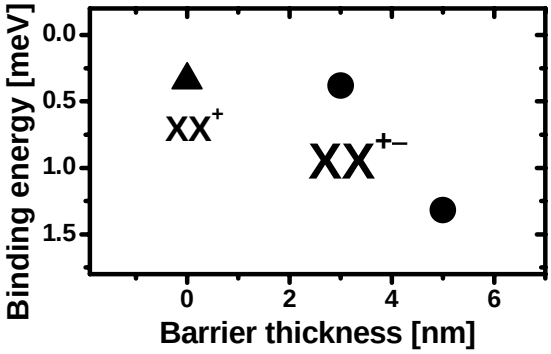

Fig. 5-26. Binding energy of the exciton molecule and the self-biexciton as a function of the barrier thickness.

increases the inter-carrier distance, and also the larger interdot spacing may increase it, because these bonding levels are expected to be slightly localized in either one of two QDs, respectively, due to the small energy mismatch between two QDs. We think that this effect seems to be the main origin of the large binding energy of an exciton molecule and the barrier thickness dependence. Of course, our data is insufficient for quantitative analysis, therefore, further systematic experiments need to be performed for a definitive understanding.

5-4-3. Conclusion

We discussed the interdot interaction in an intermediate CQD system. The intermediate coupling strength in d = 5 nm CQD enabled us to produce an individual excitation of the bonding (X^+)/anti-bonding (X^-) states. We demonstrated the formation of an exciton molecule consisting of X^+ and X^- excitons in a CQD, which appeared in the two-color excitation PL spectra. In addition, we suggested that the binding energy of an exciton molecule depended on the inter-carrier distance. Our result offers new possibilities for quantum logic devices using a CQD system.

5-5. Interdot Interaction in a Weakly Coupled Quantum Dot *~Multiplication Effect of PL Intensity~*

In the above sections, we investigated the inter-exciton interaction in quantum mechanical CQDs. We demonstrated that quantum mechanical coupling induced the formation of an exciton molecule consisting of bonding states. However, it is difficult for us to distinguish between quantum mechanical and electromagnetic couplings, because these coexist in the quantum coupling system. Furthermore, the complexities of the electronic structures and the coupling mechanisms are an obstacle for the application of a CQD system, as indicated in Section 5-2-4. On the other hand, as described in Section 3-1-5, the thick interdot spacing sufficiently weakens the quantum mechanical coupling so as to neglect the carrier transfer between QDs, but maintains an electromagnetic interaction. The simplification of the coupling mechanisms will help us understand the interdot interaction and provide us with a simple system for applications. In this section, we discuss the interdot interaction in d = 7 nm single CQD, in which the carrier transfer between QDs is negligible as mentioned in Section 5-2. We present the responses in a co-excitation of two QDs constituting a CQD.

5-5-1. Samples and Experimental Setup

The sample used in this section was the same as the d = 7 nm CQD treated in Section 5-2. The experimental set-up was also the same as that outlined in the previous Sections 5-2-4, in which a 1-m double monochromator and a cooled CCD detector were used. The samples were cooled to 6 K in a liquid helium cryostat and two continuous-wave tunable Ti:sapphire lasers were used as excitation sources in the two-color PLE measurement.

5-5-2. Results and Discussion

The PL and PLE spectra of two pairs of CQDs used in this section are presented in Fig. 5-27(a). CQD A is the same single CQD as presented in Section 5-2, and CQD B is another single CQD lying in a different aperture hole on the same sample. In Section 5-2, we described the two fundamental PL peaks as X^{+}_{2} and X^{-}_{2}. However, it may be better to express these peaks as the different QDs constituting a CQD, because the carrier transfer is negligible in d = 7 nm CQD.

Therefore, the two PL peaks are expressed as two QDs (QD1, QD2) in Fig. 5-27(a).

As shown in the PLE spectra of QD1/QD2, the discrete excited levels due to three-dimensional quantum confinement, which are related to holes (Section 5-2), are observed as in previous sections. These excited levels vary between QD1 and QD2 as regards the reflection of the different luminescence energies, consequently this observation ensures that there is no carrier transfer between QD1 and QD2. These results are common features in CQD A and B, and make it possible for us to excite each QD individually using two laser sources and observe the interdot interaction.

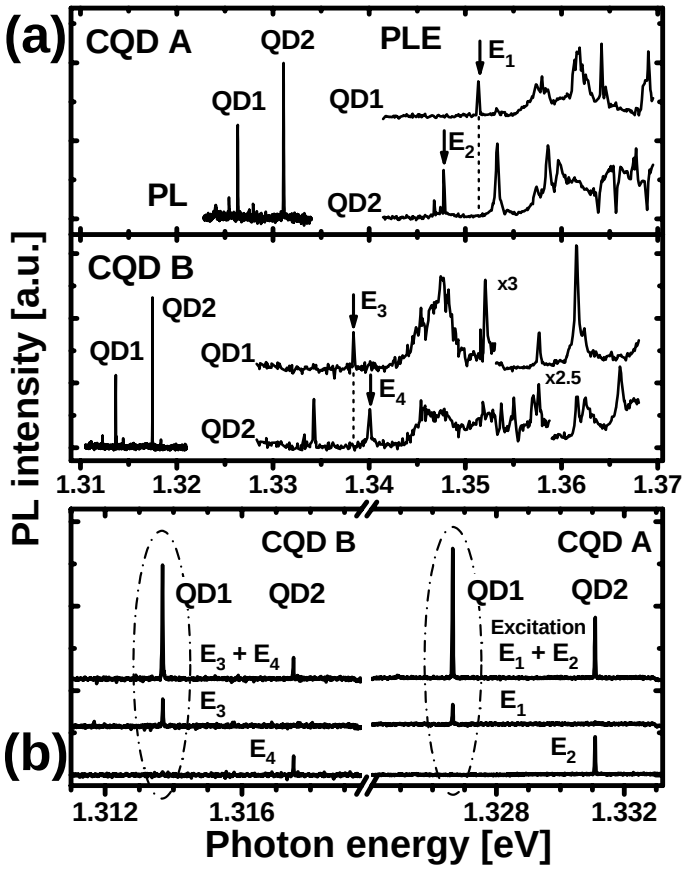

Fig. 5-27. (a) PL/PLE spectra of d=7nm single CQD. CQDs A/B are located in different aperture hole. QD1/QD2 indicate the two QDs in a single CQD, respectively. (b) PL spectra of CQDs in figure (a) under 1-color and 2-color excitation condition. E1 (E3) and E2 (E4) indicate the excitation energy of the two laser sources as are shown in figure (a).

Figure 5-27(b) presents the PL spectra under the one-color or two-color excitation. In the case of CQD A, the E1 (E2) energy excites only QD1 (QD2) as shown in the middle (bottom) of the figure. However, when QD1 and QD2 are excited at the same time by using two-color excitation (both E1 and E2), there is a noticeable increase in the PL intensity (at the top of the figure). In particular, the PL intensity of QD1 is dramatically increased more than three times. Exactly the same feature was observed in the case of CQD B. These observations directly indicate the existence of an interdot interaction in the electromagnetic CQD.

To rule out the possibility that the above results indicate an accidental observation, we simply have to confirm whether the luminescence intensity of QD1 increases with the excitation of most excited levels of QD2. This is because the carriers created in QD2 will influence the luminescence

of QD1 independently of which levels of QD2 are excited if the interaction occurs. Therefore, we performed a two-color PLE measurement, as mentioned in the previous sections. The measurement procedure is as follows [Fig. 5-28(a)]. To begin with, the wavelength of the pump light source is fixed at an excited state of QD1, which is excited constantly, as indicated by "Pump" in the figure. Then, QD2 is excited by a 2nd probe light source whose wavelength is scanned for the PLE measurement. We measure the PLE spectra of QD1 with (two-color PLE) and without (one-color PLE) the pump: the interaction between two QDs will appear in the two-color PLE. Finally, we confirm which levels of QD2 influence the luminescence intensity of QD1 by comparing the two-color and one-color PLE.

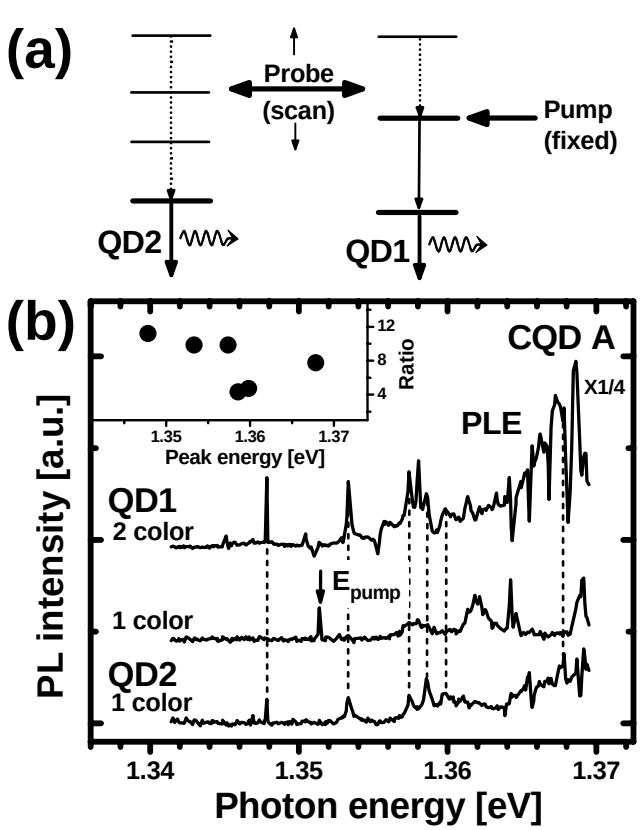

Fig. 5-28. (a) 2-color PLE experiment. (b) Results of 2-color PLE measurement in CQD A. The bottom (middle) spectrum is the 1-color PLE spectrum of QD2 (QD1). The top spectrum is the 2-color PLE spectrum of QD1, which was pumped constantly at the E_{pump} energy by another laser source. The inset shows rate of PL increasing in QD1 with 2-color excitation; the amount of QD1 PL increasing with 2-color excitation is divided by the QD2 PL intensity with 1-color excitation for the particular peaks indicated by the dotted lines.

The measurement result of CQD A is shown in Fig. 5-28(b). The one-color PLE peaks of QD2 seen at the bottom of the figure coincide with the two-color PLE peaks of QD1 at the top of the figure, which indicate the increasing PL intensities of QD1, as indicated by dotted lines. This result shows that the carriers created in QD2 are certain to couple with those in QD1 in any excited state of QD2. Thus, our remarkable observation demonstrates the interdot interaction in the electromagnetic CQD.

Next, let us consider the mechanism of interdot interaction in weakly CQDs. Here, we give some possible explanations for the PL enhancement effect, as follows: (1) carrier transfer through the tunneling process (Dexter type energy transfer);[131] (2) two-photon absorption; (3) Förster type

energy transfer;[132] (4) super radiance effect.[133]

As mentioned in Section 5-2, the assumption (1), carrier transfer, is very small in d = 7 nm CQD. If the tunneling process had occurred, the one-color excitation would have yielded both QD1 and QD2 emissions. The realization of separate excitation evinced the inadequacy of assumption (1). Next, the assumption (2), two-photon absorption, induces interband transition at a higher energy than the wetting layer energy. In this case, the PL spectrum under two-color excitation should be the same as that under one-color wetting layer excitation. However, this prediction contradicts our observations. It is also difficult to explain the PL enhancement more than three times by two-photon absorption. The Förster type energy transfer, assumption (3), is a typical process in electromagnetic interaction. In this process, the higher energy system releases energy to the lower energy system through dipole-dipole interaction. In this case, although carrier transfer is not involved, the one-color excitation of QD1 yielded QD2 emission. However, the separate excitation in our CQD system conflicts with this assumption. The super radiance effect, assumption (4), proposed by R. H. Dicke, is the coherent conjunction phenomenon of the transition dipole aggregates, in which coherent coupling between transition dipoles leads to stimulated emission resulting in enhanced luminescence.[134] In QDs, the shortening of emission lifetime, namely the emission enhancement per unit time, has been reported.[135] This has been understood as the super radiance effect caused by the fact that the transition dipole fills the volume of a QD coherently (coherent volume).[136] In this case, the PL intensity is expected to be two-fold with the double coherent volume caused by the total size of a CQD. However, the increment in the PL intensities in our observations is too large to be explained by super radiance.

Thus, the explanations given above do not correspond to our observations. Here, we propose a model where the PL increment originates from the enhancement of the energy relaxation caused by the electromagnetic interaction between two QDs. That is, the quasi-biexcitonic state induced by the

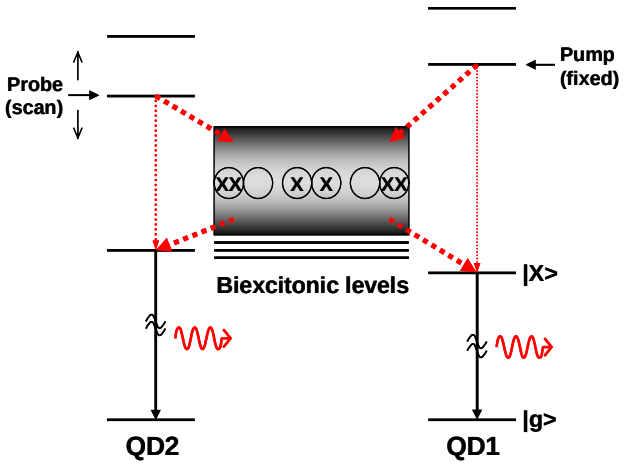

Fig. 5-29. Quasi-biexcitonic state induced by the dipole-dipole interaction between excitons of QD1/QD.

dipole-dipole interaction between excitons of QD1/QD2 allows extra rapid relaxation paths that enhance the energy relaxation per unit time, resulting in the increment of the PL intensity (Fig. 5-29).

Here, in order to consider the above interpretation, we present the excitation power dependence of the PL intensity under two-color excitation. Figure 5-30(a) shows the excitation power dependence of integral PL intensities in CQD A. The open circle and triangle indicate the dependences of QD1 and QD2, respectively, under the one-color excitation condition, which reasonably exhibits linear dependence on the excitation power (m = 1). The filled circle and triangle denote the dependences under the two-color excitation condition, where the data for QD1 were obtained under the varied E2 intensity with constant E1 excitation and the data for QD2 were obtained under the varied E1 intensity with constant E2 excitation. Consequently, these observations mean the PL increment caused by carrier creation in the neighboring QD [see Fig. 5-30(b)]. As we can see, the dependences in two-color excitation express the non-linear dependence on excitation intesity (m < 0.5). Here, we consider the increasing amount of PL intensity in two-color excitation:

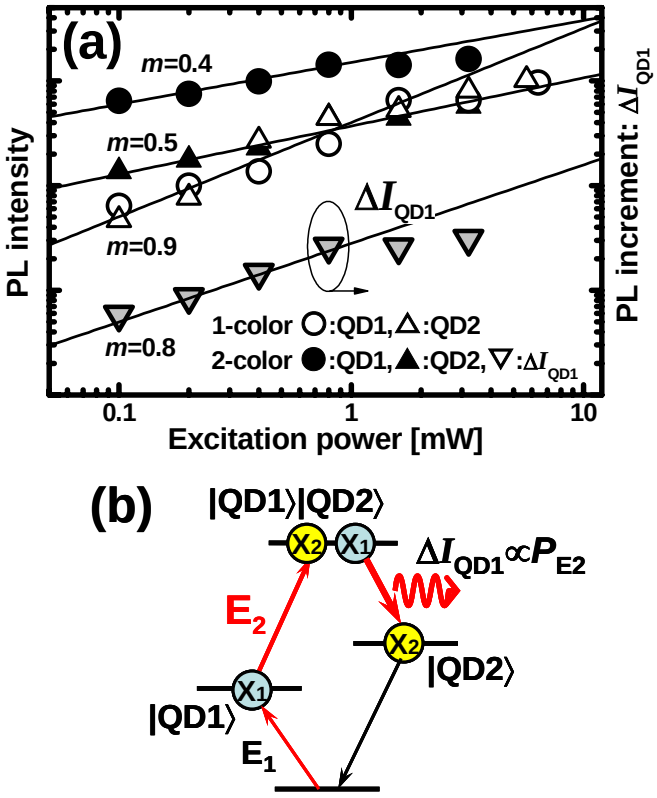

Fig. 5-30. (a) Excitation power dependence of integral PL intensities in CQD A. QD1 and QD2 were excited at E1 and E2, respectively. In 2-color excitation, the detection of QD1 was performed under the varied E2 intensity with constant E1 excitation, and vice versa. Solid lines are fitting curves with the exponent "*m*" to the excitation power. (b) Carrier occupation diagram in a weakly CQD.

$$\Delta I_{QD1} = I_{QD1}^{2c} - I_{QD1}^{1c}, \quad \text{…Eq. 5-7}$$

where I^{2c} is the PL intensity under two-color excitation, and I^{1c} is the PL intensity under one-color excitation. The inverted triangle in Fig. 5-30(a) denotes ΔI_{QD1} as a function of QD2 excitation power. As we can see, ΔI_{QD1} shows close to linear dependence on the QD2 excitation power (m = 0.8). This result reflects the fact that the PL increment arises from the state |QD1⟩|QD2⟩ in which both QD1 and QD2 are excited [|QD1⟩|QD2⟩ → |QD2⟩ as shown in Fig. 5-30(b)]. The fact that the

PL increment is more than three times indicates that the increasing ratio of PL intensity is very large.

Then, we analyzed the PL increasing ratio in two-color excitation on the basis of our interpretation. We consider the rate equation of QD1 [Fig. 5-31(a)]:

$$\frac{dN_2}{dt} = -\gamma_{21}N_2 + \Gamma N_0 , \quad \frac{dN_1}{dt} = -\gamma_{10}N_1 + \gamma_{21}N_2 . \quad \textbf{…Eq. 5-8}$$

From these equations, the population of the lowest excited level N_1 is written as

$$N_1 = \frac{\Gamma \cdot \gamma_{21}}{\gamma_{10}\Gamma + (\gamma_{10} + \Gamma)\cdot \gamma_{21}} N . \quad \textbf{…Eq. 5-9}$$

When the interband energy relaxation γ_{21} is modulated by the carrier population of QD2, the increasing ratio of PL intensity in two-color excitation is derived as

$$N_{2c}/N_{1c} = \frac{\gamma_{10}\Gamma + (\gamma_{10} + \Gamma)\gamma_{21}^{1c}}{\gamma_{10}\Gamma + (\gamma_{10} + \Gamma)\gamma_{21}^{2c}} \frac{\gamma_{21}^{2c}}{\gamma_{21}^{1c}}, \quad \textbf{…Eq. 5-10}$$

where N_{1c} and N_{2c} are the carrier populations in one-color and two-color excitations, γ_{21}^{1c} and and γ_{21}^{2c} are the interband energy relaxation rates in one-color and two-color excitation, respectively. Here, we assume that the interband energy relaxation γ_{21}^{2c} is proportional to the carrier population of QD2 (N_{QD2}); that is, γ_{21}^{2c} is proportional to the QD2 excitation intensity (P_{E2}):

$$\gamma_{21}^{2c} \propto N_{QD2} \propto P_{E2} . \quad \textbf{…Eq. 5-11}$$

Then, we analyzed the observation results using Eqs 5-10 and 5-11. Figure 5-31(b) presents the PL increasing ratio N_{2c}/N_{1c} as a function of QD2 excitation intensity. Different marks in the figure denote different QD1 excitation conditions. As shown in the figure, the fitting curves derived from Eqs 5-10 and 5-11 reproduce the observation results even with different excitation conditions of QD1 (Γ = 0.42, 0.67), where the carriers mainly

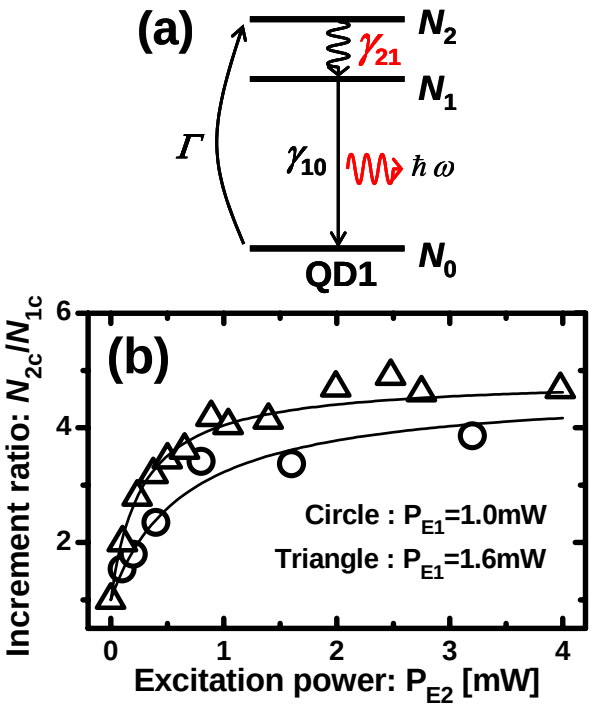

Fig. 5-31. (a) Energy level diagram of QD1. (b) Increment ratio of QD1 PL intensity in CQD A under 2-color excitation as a function of E2 excitation intensity, where the E1 intensity was constant. Solid lines are fitting curves (see the text).

occupy the excited state N_2 in these excitation conditions. Thus, these analyses strongly support our interpretation that the PL increment in two-color excitation arises from enhancement of the interband energy relaxation due to interdot interaction, such as dipole-dipole interaction. When we consider $1/\gamma_{10}$ = 1.24 ns (Section 5-1), we obtain $1/\gamma_{21}^{1c}$ = 5.2 ns from the fitting parameters. Furthermore, we can estimate that the energy relaxation time $1/\gamma_{21}^{2c}$ is reduced from 5.2 ns to 650 ps by the co-excitation of QD1/QD2 (at P_{E2} = 1 mW).

Here, we mention another possible interpretation: the defect levels near the QD are occupied by photo-generated carriers in QD2, which leads to the inhibition of optical quenching, and consequently QD2 emission is increased. We verified this interpretation by means of the rate equations

$$\frac{dN_2}{dt} = \Gamma N_0 - (\gamma_{21} + \gamma_{df})N_2\,, \quad \frac{dN_1}{dt} = \gamma_{21}N_2 - (\gamma_{10} + \gamma_{df})N_1\,, \qquad \textbf{…Eq. 5-12}$$

where γ_{df} is the relaxation rate through the defect level. We assumed $\gamma_{df}^{2c} \propto \gamma_{df}^{1c} / P_{E2}$, and estimated N_{2c}/N_{1c} as is the case with Eq. 5-10. However, we could not reproduce our experimental results with realistic fitting parameters, because we needed $\gamma_{df} >> \gamma_{10}$ (one-order magnitude) for the fitting ($1/\gamma_{df}$ ~ 100–200 ps). This kind of fast detention time in the defect level is unlikely because the non-radiative recombination time was estimated at 1–10 ns in III-V compound semiconductor nano-structures.[137,138] Furthermore, the observation of PL lifetime = 1.24 ns (Section 5-1) conflicts with such a fast non-radiative recombination because the PL lifetime is composed of radiative and non-radiative recombination times ($1/\tau_{PL} = 1/\tau_{10} + 1/\tau_{df}$).

In the first place, if the defect level has an effect on the photon emission process, the two-color excitation of QD1 induces similar phenomena to the PL increment in the excitation of both QD1/QD2. However, our results in the two-color PLE experiment conflict with this prediction. For example, let us look back at the two-color PLE spectrum of QD1 in Fig. 5-28(b). The one-color PLE spectrum of QD1 exhibits PLE peaks around 1.362 and 1.364 eV. Therefore, it might be expected that the excitation at these PLE peaks induced the large PL increment in the two-color excitation condition if the above prediction was correct. However, the fact that the large PL increments are not present around 1.362 and 1.364 eV in the two-color PLE spectrum of QD1 conflicts with the mentioned assumption of the effect from the defect levels.

Thus, from the above discussion, our interpretation of the acceleration of energy relaxation with

interdot interaction is thought to be the most likely cause of our observations. In passing, a PL energy shift by the two-color excitation was not observed in our experiments. This implies that the dipole-dipole interaction in d = 7 nm CQDs is not as intensive as leading to a larger energy shift than the spectrum resolution (20 μeV).

5-5-3. Conclusion

Interdot interaction in d = 7 nm weakly CQDs has been discussed. The separate excitation of two QDs constituting the CQD was achieved because of the negligible carrier transfer arising from weak wave function coupling. The simultaneous carrier creation in two QDs (two-color excitation) induced the anomalous increment in PL intensity in the PL/PLE spectra, which evidenced the interdot interaction in electromagnetic CQD. We suggest that this result originated from the enhancement of interband energy relaxation due to interdot interaction.

5-6. Correlated Photon Emission in a Weakly Coupled Quantum Dot

In the previous section, we presented interdot interaction in electromagnetic CQDs. The enhancement of PL intensity was observed as interdot interaction under the simultaneous co-excitation of two QDs constituting the CQD. We suggested that this observation seemed to arise from the enhancement of the interband energy relaxation due to the dipole-dipole interaction between QDs. However, the photon emission dynamics is not always clear. Therefore, in this section, we attempt to detail the photon emission process in an electromagnetic CQD by observing the photon emission correlation between QDs. The observation of a photon emission process in a CQD by the time correlated single photon counting experiment will make it possible for us to discuss the time evolution of the interdot interaction.

5-6-1. Sample

The sample used in this section is the same as the d = 7 nm CQD treated in the previous section, while the aperture hole is different from that used in the previous section. Figure 5-32 presents the observation results under two-color excitation spectroscopy as performed in the previous section. In spite of observation with a different aperture hole, enhancement of the PL intensity was observed when both QD1 and QD2 constituting the CQD were simultaneously excited at their unique excited states E1 and E2 [figure (b)], as shown in the previous section. As mentioned in the previous section, this phenomenon is a

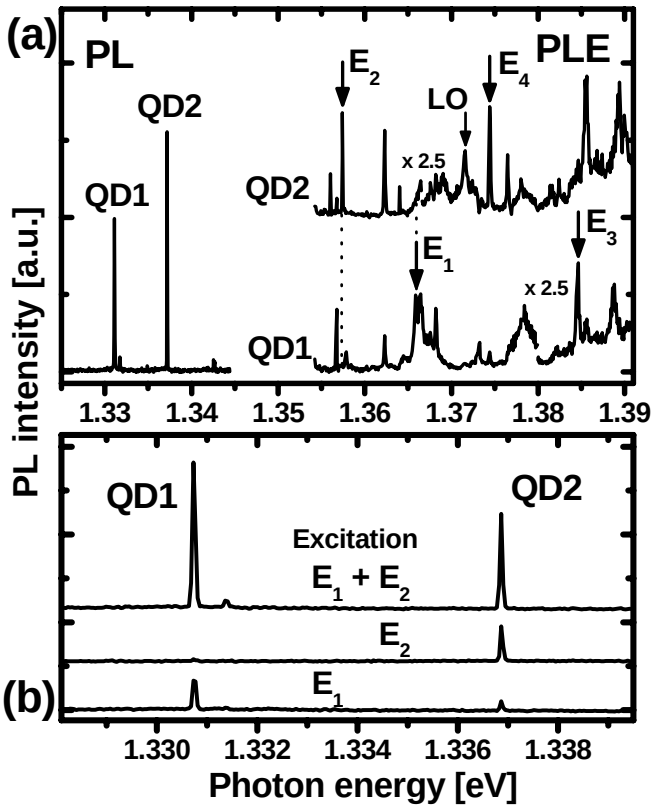

Fig. 5-32. (a) PL/PLE spectra of d=7nm single CQD. (b) PL spectra of the CQD under 1-color/2-color excitation, whose energies are indicated in figure (a).

common feature in d = 7 nm CQDs. In this section, we measure the photon emission correlation between QD1 and QD2 in Fig. 5-32 by the time correlated photon counting experiment.

5-6-2. Photon Correlation Statistics

Here, we briefly mention the photon correlation measurement technique.[82,139] First, let us consider the time correlation of optical intensity in an intensity fluctuated light as shown in Fig. 5-33(a). The Hanbury-Brown-Twiss set-up indicated in Fig. 5-33(b) is commonly used in the time correlation measurement of photons.[140] In the experimental set-up, the coincident counting of photons both on the single photon detector 1 in the time interval from t to $t+dt_1$ and on detector 2 from $t+\tau$ to $t+\tau+dt_2$ is proportional to the following formula:

$$I(t)I(t+\tau)dt_1dt_2. \quad \textbf{...Eq. 5-13}$$

Here, we define the time average of Eq. 5-13 as $\langle I(t)I(t+\tau)\rangle$, and define the time averages of photon counts by detectors 1 and 2 as $\langle I(t)\rangle$ and $\langle I(t+\tau)\rangle$, respectively. Then, the former is normalized by the latter, and we obtain the coincident counting probability at the time delay τ, as follows:

$$g^{(2)}(\tau)=\frac{\langle I(t)I(t+\tau)\rangle}{\langle I(t)\rangle\langle I(t+\tau)\rangle}. \quad \textbf{...Eq. 5-14}$$

This is known as a second-order photon correlation function. As can be seen from Fig. 5-33 and Eq. 5-14, the photon correlation function near $\tau = 0$ means the photon number at $\tau = 0$ relative to the photon number at $\tau >> 0$. For example, in the case of a pulsed light as shown in Fig. 5-33(c), if a single pulse contains only a single photon, the destination of this photon through the beam splitter is either detector 1 or detector 2. This means a coincident counting probability of $g^{(2)}(0) < 1$, because the two detectors do not detect the photon simultaneously. This feature

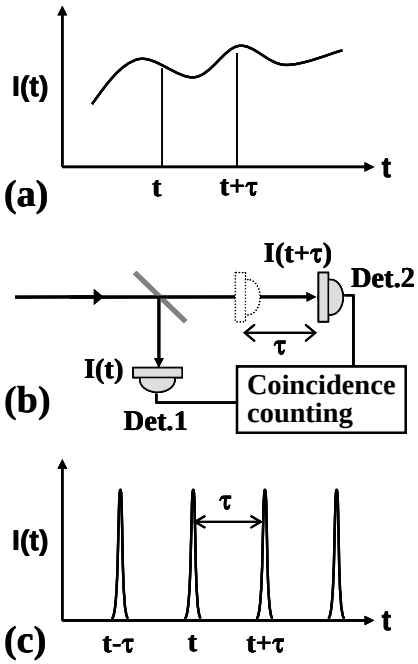

Fig. 5-33. Time-correlated photon statistics. (a) Light with temporal fluctuation. (b) Photon correlation measurement (Hanbury-Brown-Twiss setup). (c) Pulsed light source.

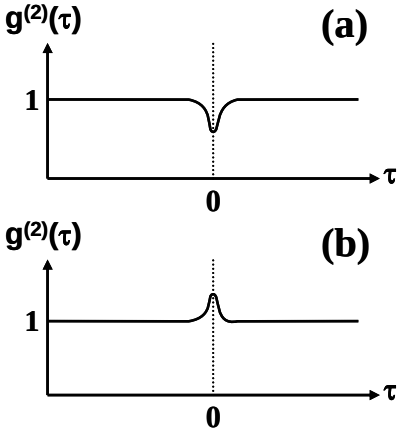

Fig. 5-34. Second-order photon correlation function.
(a). Anti-bunching. (b). Bunting.

is called “photon anti-bunching” [Fig. 5-34(a)]. Even with a single photon in a single pulse, the non-correlation of emissions between one photon at t and another photon at $t + n\cdot\tau$ results in $g^{(2)}(n\cdot\tau) = 1$ ($n = \pm1, \pm2, \pm3\ldots$). On the other hand, the case of a pulse containing several photons has the possibility of $g^{(2)}(0) \geq 1$, because the detectors can detect photons simultaneously. Here, the case of a coherent light source with a Poisson distribution, such as a laser, presents $g^{(2)}(0) = 1$. In addition, natural light, such as black-body radiation, provides $g^{(2)}(0) > 1$, because the stimulated emission of one atom is induced by the photon emitted from another atom within the coherence time. This feature is called “photon bunching” [Fig. 5-34(b)].

As mentioned in Section 3-2-3, the exciton level in a QD becomes a single discrete state due to three-dimensional quantum confinement. This means that the number of excitons lying at the lowest excited level is unity. Consequently, the recombination of the exciton causes emission of a single photon. In this process, the photon re-emission of the exciton after the photon emission of the previous exciton requires a time interval more than the recombination life time of an exciton. In other words, a single QD always emits a single photon intermittently, even in the continuous excitation condition.

In fact, there have been several previous reports on observation of a single photon emitting from a single QD by the Hanbury-Brown-Twiss experiment.[32,33, 35,83,84] In one example, we cite the emission correlation between an exciton and a biexciton in a QD, reported by E. Moreau *et al.* (Fig. 5-35).[33] In the case of the biexciton existing in a QD, the exciton emits a photon just after the dissociation and photon emission of the biexciton. In this system, the observation of the coincident counting probability between an exciton and a biexciton at $\tau < 0$ shows the anti-bunching of $g^{(2)}(0) < 1$, because the exciton emission does not arise at $\tau < 0$, which is the time segment before the biexciton emission (see Fig. 5-35). On the other hand, in the time segment of $\tau > 0$, in which the biexciton has already emitted a photon, the coincident counting rate presents the bunching of $g^{(2)}(0) > 1$ due to the cascading photon emission of the exciton after the biexciton emission. Thus, the estimation of $g^{(2)}(\tau)$ by the time correlated photon

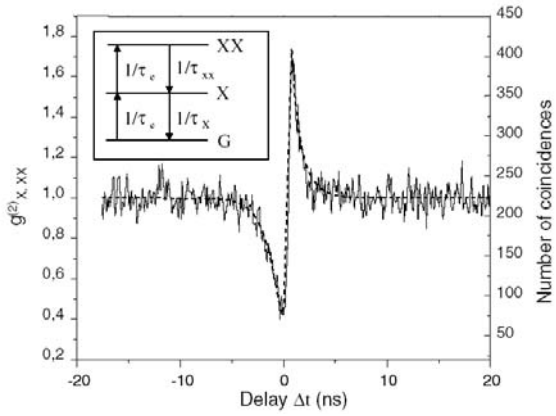

Fig. 5-35. Time-correlated photon statistics in a single QD, reported by E. Moreau *et al.*.

counting gives information on photon emission dynamics.

This technique has already been applied to the observation of a single CQD, as reported by B. D. Gerardot *et al.*[85] Although they suggested that dipole-dipole interaction dominated the photon emission process in a CQD, the very thin barrier (d = 3 nm) between QDs in the sample used in their report was unable to remove the effect of quantum coupling and has made it difficult to analyze the photon emission processes. On the other hand, the CQDs used in this section have a thick barrier layer (d = 7 nm), which effectively diminishes the quantum coupling and enables the individual excitation of two QDs, as mentioned in the previous sections. Therefore, the dipole–dipole interaction in a CQD will be discussed more clearly.

5-6-3. Single Photon Emission Depending on Energy Relaxation

Figure 5-36(a) shows the experimental system we used for time correlated photon-counting measurements. The basic system is pursuant to the Hanbury-Brown-Twiss set-up, as mentioned above. The CQD sample was cooled to 6 K in a liquid helium cryostat and excited by two continuous-wave tunable Ti:sapphire lasers at the sample rear surface, where the components were located in forward scattering geometry. The QD luminescence emitting from the sample front surface was collected through a 50× objective lens and was led into a 50:50 beam splitter. The separated beams were led into two monochromators, which selected photons from an arbitrary QD (QD1 or QD2), and the selected photons were then detected by single

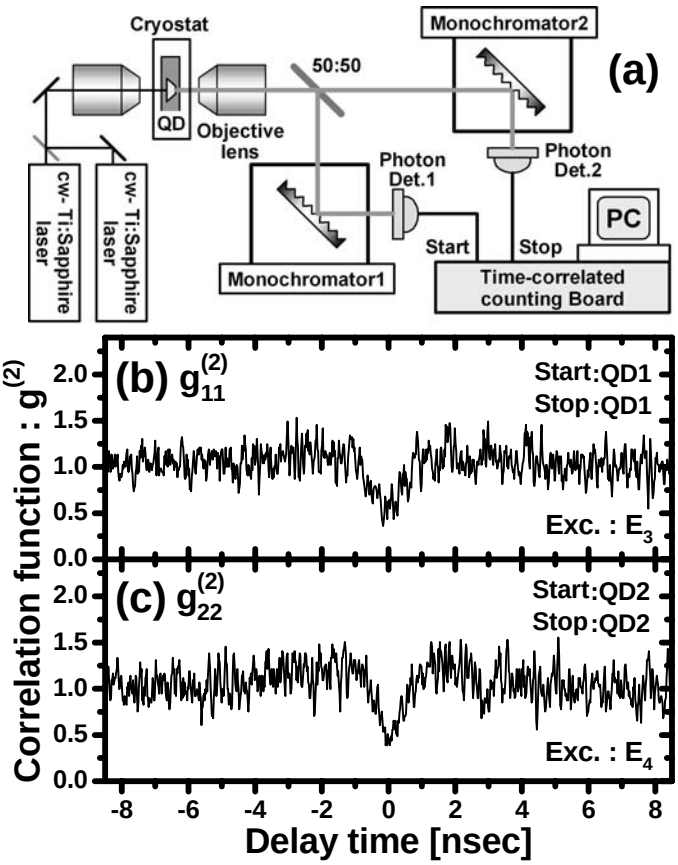

Fig. 5-36. (a) Experimental setup of time-correlated photon counting. (b-c) 2nd-order photon correlation function spectra of a single CQD under 1-color excitation [QD1: (b), QD2: (c)], where the excitation energies are indicated in Fig. 5-25 (E_3, E_4).

photon detectors (Si avalanche photodiode). By using start and stop signals from the detectors, the time correlated counting board outputs the second-order photon correlation function (PCF) spectrum: $g^{(2)}_{\alpha,\beta}(\tau) = \langle I(t)I(t+\tau)\rangle / \langle I(t)\rangle\langle I(t+\tau)\rangle$, where the suffix α (β) indicates the selected QD as a start (stop) signal.

First, we confirm the single photon emission from each QD constituting the CQD. In Fig. 5-36(b-c), we present the auto-PCF spectra of QD1 and QD2 under the one-color excitation condition, where the wavelengths of both monochromators were set to that of QD1 or QD2. The two QDs were individually excited at the E3 (E4) energy indicated in Fig. 5-32(a); this means that the interdot interaction between QD1 and QD2 was miniscule. As shown in the figures, the auto-PCF spectra of both QD1 and QD2 ($g^{(2)}_{11}$ and $g^{(2)}_{22}$) exhibit dip structures around the delay time DT = 0, which mean reduction in the coincident photon counting rate. These structures originate from photon anti-bunching, which is evidence for the single photon emission from each QD constituting the CQD, as described in previous reports.

Even in the case without interdot interaction, the auto-PCF spectrum of a single QD reflects the difference of the energy relaxation process to the state emitting photon. With an excitation energy higher than the longitudinal optical (LO) phonon energy, the energy relaxation of the photo-generated carriers is rapid due to the exciton–LO phonon interaction, as discussed in Section 5-1. On the other hand, when the excitation energy is lower than that of the LO-phonon, the energy relaxation of the carriers depends only on the acoustic phonon emission, which requires several nanoseconds. In Fig. 5-37, we show the auto-PCF spectra of QD2 under one-color excitation whose energy was higher [E4: Fig. (a)] or lower [E2: Fig. (b)] than the excited level resonated with the LO-phonon (ΔE_{LO} = 34.4 meV, see Fig. 5-32). While both spectra show anti-bunching at DT = 0 reflecting single photon emission, the

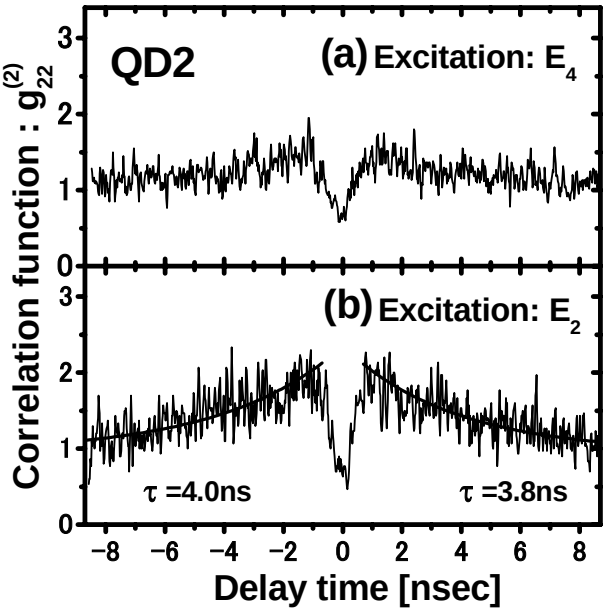

Fig. 5-37. Excitation energy dependence of a photon correlation spectrum in QD2. (a). Excitation energy more than LO-phonon resonated level (E_4). (b). Excitation energy less than LO-phonon resonated level (E_2)。 τ indicates the decay time of bunching appearance.

excitation at an energy lower than the LO-phonon level causes bunching feature whose decay time τ is about 4 ns. This result indicates that the photon emission is stimulated during DT < ± 4 ns when the energy relaxation is caused by the acoustic phonon.

When the carrier energy relaxation is caused by the LO-phonon (E4 excitation), the cycle time of an exciton emission in a QD is about an exciton lifetime (~1 ns) due to the rapid energy relaxation process, and consequently the detection probability of the next exciton emission is regarded as constant in the time domain of DT > ±1 ns. Therefore, the $g^{(2)}_{22}$ in Fig. 5-37(a) does not show bunching. On the other hand, when the carrier energy relaxation is caused by the acoustic phonon (E2 excitation), the 1st exciton (detected as a start signal) will leave several acoustic phonons in the QD before the photon emission. In this case, it is just conceivable that these phonons remain in the QD for a while after the photon emission. Consequently, the 2nd exciton generated in the QD (detected as a stop signal) will be scattered by these residual phonons (see Fig. 5-38). The phonon scattering rate is proportional to the phonon number, according to following formula:

$$\left|M_q\right|^2 \propto \begin{array}{ll} \left|\left\langle k+q, n_q-1 \middle| a_q \middle| k, n_q \right\rangle\right|^2 = n_q & : \text{Absorption} \\ \left|\left\langle k-q, n_q+1 \middle| a_q^{\dagger} \middle| k, n_q \right\rangle\right|^2 = n_q+1 & : \text{Emission} \end{array} \quad , \qquad \text{…Eq. 5-15}$$

where n_q is the number of phonons, a_q and $a^{\dagger}_q$ are creation and destruction operators, and k and q are the exciton and phonon wavenumbers. The high scattering rate accelerates the carrier energy relaxation. Therefore, the detection probability of a stop signal during the phonon survival time is expected to become higher than that in DT >> 0 time domain. On the basis of the above discussion, our observation of the bunching for DT < ± 4 ns in Fig. 5-37(b) is considered to originate from the enhancement in the energy relaxation caused by the residual phonons emitted from the start signal exciton. And, the decay time of the bunching (~4 ns) indicates the phonon dissipation time.

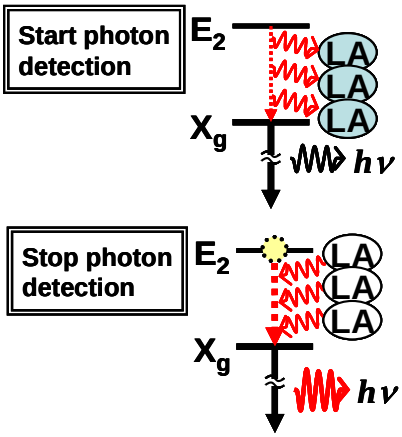

Fig. 5-38. Photon detection processes.

Here, let us compare the bunching decay time with the phonon dissipation time estimated using classical statistical mechanics. It is well known that the phonon dissipation time is classically given by

$$\tau = \frac{3\kappa}{C_v v^2}, \quad \text{…Eq. 5-16}$$

where C_v is the specific heat at constant volume, κ is the thermal conductivity, and v is the phonon (sound) velocity.[141] When we used C_v = 107.2 mJ/K,[142] κ = 25 W/cm K, and $v = 4\times10^5$ cm/s for GaAs,[40] the phonon dissipation time was estimated to be 4.4 ns. This value corresponds quantitatively with our observation of the bunching decay time and this correspondence supports our interpretation. In addition, we roughly estimate the number of residual phonons on the basis of the magnitude of $g^{(2)}_{22}$. As seen in Fig. 5-37(b), the bunching magnitude is almost double. If it is assumed that a phonon does not exist in the steady state, the phonon scattering rate will double when there is an average of one phonon in the bunching time domain (see Eq. 5-15). In this case, the photon detection probability ($g^{(2)}_{22}$) is considered to be doubled. Accordingly, we can roughly estimate the number of residual phonons as one in the bunching time domain.

5-6-4. Cross-Photon Correlation between Two QDs

Next, we consider the correlated photon emission between two QDs in a weakly CQD. Figure 5-39 shows the PCF spectra of the CQD under two-color excitation conditions, where QD1 (QD2) was excited at E1 (E2) energy indicated in Fig. 5-32(a). Figure (a) and (b) show the auto-PCF spectra of QD1 and QD2, respectively. Both spectra, $g^{(2)}_{11}$ and $g^{(2)}_{22}$, exhibit the bunching feature as found with the result in Fig. 5-37(b). Figure (c) shows the cross-PCF spectrum $g^{(2)}_{12}$ between QD1 (for a start signal) and QD2 (for a stop signal). It is noteworthy that spectrum $g^{(2)}_{12}$ exhibits a wide

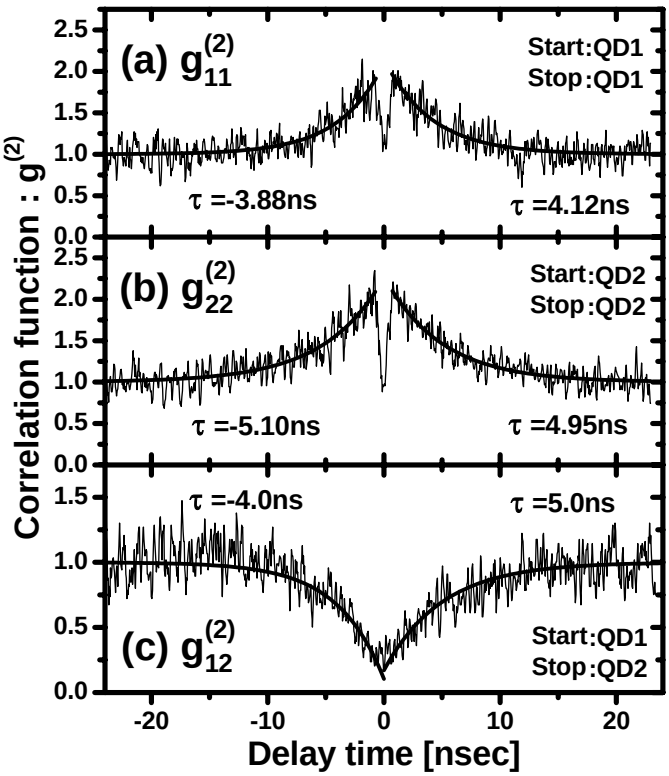

Fig. 5-39. 2nd-order photon correlation spectra of a single CQD under 2-color excitation. (a-b) Auto photon correlation spectra, (a): QD1, (b): QD2. (c) Cross photon correlation spectrum between QD1 and QD2. QD1/QD2 were excited at E_1/E_2 indicated in Fig. 5-25, respectively. τ indicates the decay time of bunching and anti-bunching.

anti-bunching structure without bunching. We qualitatively interpret this notable observation on the basis of the discussion in Section 5-5, as described below.

First, we consider the photon detection process in the cross-photon correlation experiment. Figure 5-40 shows the carrier occupation diagram in a CQD, which includes the inter-band energy relaxation process in each QD. In this figure, the photon detection process of the start signal (QD1) is either $|1\rangle|0\rangle \rightarrow |0\rangle|0\rangle$ or $|1\rangle|1\rangle \rightarrow |0\rangle|1\rangle$. For each start detection process, the detection processes of the stop signal (QD2) are described as below;

[QD1 detection]	[QD2 detection]
$\|1\rangle\|0\rangle \rightarrow \|0\rangle\|0\rangle$	(1) $\|0\rangle\|0\rangle \rightarrow \|0\rangle\|1\rangle \rightarrow \|0\rangle\|0\rangle$
	(2) $\|0\rangle\|0\rangle \rightarrow \|1\rangle\|0\rangle \rightarrow \|1\rangle\|1\rangle \rightarrow \|1\rangle\|0\rangle$
$\|1\rangle\|1\rangle \rightarrow \|0\rangle\|1\rangle$	(3) $\|0\rangle\|1\rangle \rightarrow \|0\rangle\|0\rangle$
	(4) $\|0\rangle\|1\rangle \rightarrow \|1\rangle\|1\rangle \rightarrow \|1\rangle\|0\rangle$

The shortest of these detection processes is the (3) pass; QD1: $|1\rangle|1\rangle \rightarrow |0\rangle|1\rangle$, QD2: $|0\rangle|1\rangle \rightarrow |0\rangle|0\rangle$. Therefore, in the cross-photon correlation measurement, it is considered that the (3) pass is mainly counted and contributes to the $g^{(2)}_{12}$ spectrum.

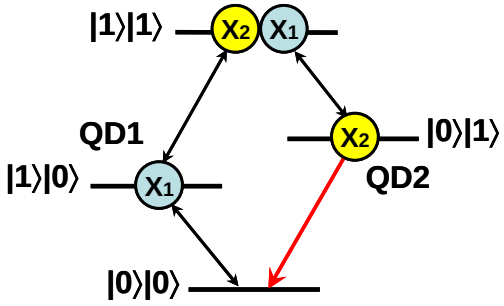

Fig. 5-40. Carrier occupation diagram in a weakly CQDs.

In this detection pass, QD1 emits a photon at DT = 0 and then becomes vacant at DT > 0. In this case, QD2 must alone emit a photon without an interdot interaction. Here, when we review the discussion in Section 5-5, the carrier energy relaxation time *without* the interdot interaction is longer than that *with* the interdot interaction. Accordingly, the probability of detecting QD2 is considered to become lower in the immediate aftermath of the QD1 emission: this process results in anti-bunching. In this case, QD2 will take a long energy relaxation time before the photon emission and then begin to emit a photon gradually, which results in the long recovery time of the $g^{(2)}_{12}$ anti-bunching. At the same time, even if the next carriers are excited in QD1 at DT > 0, these carriers does not affect the carrier energy relaxation in QD2. This is because the secondarily excited carrier in QD1 is rapidly relaxed energetically by the residual phonon emitted at DT = 0 and then emits a photon (Section 5-6-3). Therefore, the long energy relaxation time in QD2 is maintained, which keeps the long recovery time of the $g^{(2)}_{12}$ anti-bunching. In fact, the

anti-bunching recovery times (4–5 ns) are comparable to the estimated energy relaxation time in Section 5-5 (~5 ns). As discussed above, the $g^{(2)}_{12}$ anti-bunching and it's long recovery time are attributed to the photon detection processes in the weakly CQD in the presence of the interdot interaction, and these results support our interpretation that the enhancement of carrier energy relaxation is caused by the interdot interaction.

Here, we mention other possibilities for interpretation. The first is the effect of the defect levels as mentioned in Section 5-5. In this case, in order to cause anti-bunching, the relaxation process through the defect level must be very fast (perhaps less than a few hundred picoseconds). This is because the defect level should be filled before the QD1 emission and the filled carriers should disappear immediately after the QD1 emission in order to trap the QD2 carrier. And then, the trapped QD2 carrier also disappears immediately and the next excited carrier in QD1 or QD2 fills the defect level again. If the QD1 carrier fills the defect, the excited carrier in QD2 relaxes energetically to the lowest level and emits a photon. In this process, if the energy relaxation time is long, a long recovery time for the anti-bunching will be observed. However, this kind of fast detention time in the defect level is unlikely, as discussed in Section 5-5. Another possibility is the effect of an acoustic phonon as mentioned in Section 5-6-3. The acoustic phonons emitted before the QD1 emission may influence the QD2 emission process. In this case, these retained phonons will accelerate the energy relaxation of the QD2 carriers. This effect would induce the fast recovery time of the $g^{(2)}_{12}$ anti-bunching, but our observations conflict with this prediction.

Thus, from the above discussions, the acceleration of exciton energy relaxation with the interdot interaction is thought to be the most likely interpretation of our observations.

5-6-5. Conclusion

We observed the second-order photon correlation function spectra and discussed the interdot interaction in a d = 7 nm weakly CQD. We confirmed the single photon emission from each QD constituting the CQD, in which the auto photon correlation spectrum depended on the energy relaxation process derived from the exciton–phonon interaction. The cross photon correlation spectrum between two QDs exhibited photon anti-bunching. This result implies the enhancement of exciton energy relaxation caused by the interdot interaction.

6. Summary

This thesis has mainly focused on understanding the electronic structure and interdot interaction in a coupled QD (CQD) system, which is an important physical system with the potential to realize adaptable quantum information devices. We fabricated reliable samples of CQDs, and observed their physical properties by optical measurements.

Quantum dot fabrication

We produced InAs/GaAs self-organized QD samples by the MBE crystal growth technique. The self-organized QD is the product derived from the strain originating from lattice mismatch.

In Section 4-3, we showed the potential for site controlled QD growth by utilizing the strain of a host material. We found orderly self-aligned InAs QDs on a GaAs oval crystal strain region, and showed that these QDs had high crystalline quality, similar to a QD grown by conventional methods.

In the fabrication of CQD structures, we employed the stacking growth technique of QD layers, in which the 2nd layer QDs were orderly grown above the 1st layer QDs because of the presence of crystal strain in the barrier layer induced by the 1st layer QDs. Using this technique, we could obtain a CQD system joined in the growth direction (vertical direction) with an arbitrary barrier thickness.

In Section 4-4, we showed that the modification of an InAs layer thickness enabled us to control the QD size (emission wavelength) between the 1st and 2nd QD layers, and showed that the application of the Indium-Flush method provided us with a fine quality CQD structure even in the case of a thinner barrier thickness.

In order to observe the optical properties of a single CQD, a sample that enables us to extract just a single CQD must be prepared. In Section 4-1, it was shown that optimization of the InAs layer thickness and substrate temperature enabled us almost individually to control the emission wavelength of QDs and the in-plane QD density. Accordingly, we achieved to provide the very low in-plane dot density, which was essential for single QD spectroscopy. Furthermore, it was shown in Section 4-5 that the fabrication of an aperture metal mask on the surface of QD samples with low

in-plane dot density could sufficiently ensure the selectivity of a single QD.

Optical properties of coupled QDs

Based on reliable samples of CQDs fabricated as mentioned above, we observed the optical properties and discussed the electronic structure and interdot interaction in CQDs.

In Section 5-1, we first considered the interdot interaction in non-resonant CQDs on the basis of the observation of general optical properties averaged as ensembles by macrospectroscopic measurements. We observed the carrier transfer between QDs depending on the interdot distance as a result of the variance in PL spectra, and confirmed the weakening of effective quantum confinement caused by the wave function penetrating to a neighboring QD. On the basis of observation of the carrier transfer time between QDs by time-resolved PL spectroscopy, we found a long carrier transfer time more than the PL life time of a QD. This result indicated that the electron tunneling transfer was interrupted by the phonon bottleneck effect which arose from the small energy separation between QDs.

For the realization of a quantum information device, it is necessary to understand in detail the electronic structures in a single CQD system. In Section 5-2, we discussed the overall electronic structures, involving higher energy states, in a CQD with various interdot spacings. We observed the bonding (X^+) and anti-bonding (X^-) states due to electron wave function coupling in the PL spectra of a single CQD, and confirmed that the strength of the quantum mechanical coupling varied with barrier thicknesses. We also discussed the origin of the multiple PL peaks and suggested the contribution of the hole excited states to the emission spectra of the QDs. On the basis of PLE measurements, we showed the electronic structures of a CQD system in higher energy states. We confirmed the common excited levels due to level sharing between the electron excited states and the individual excited levels originating from the hole excited states in a CQD. From these results, we classified d = 3, 5 nm CQDs into the quantum mechanical coupling system (strong coupling region) and d = 7 nm CQD into the electromagnetic coupling system (weak coupling region).

In Section 5-3, we presented the interdot interaction in a strongly (quantum mechanically) CQD with barrier thickness “d” = 3 nm. On the basis of two-color excitation spectroscopy, we demonstrated the formation of an exciton molecule consisting of X^+ and X^- excitons in a CQD.

Furthermore, we showed that both X^+ and X^- carriers were preferentially expended to form an exciton molecule, and confirmed that the formation yield of an exciton molecule was larger than that of a self-biexciton.

In Section 5-4, we discussed the interdot interaction in an intermediate CQD system, in which the quantum mechanical coupling remained. The intermediate coupling strength in d = 5 nm CQDs enabled us to produce a completely individual excitation of the X^+ and X^- states. The simultaneous excitation of both X^+ and X^- states induced a new PL peak that appeared at a lower energy than the X^+ level. We showed that this new peak originated from the exciton molecule as was discussed in Section 5-3. Thus, it was demonstrated that the quantum mechanical coupling between two QDs induced an exciton molecule consisting of X^+ and X^- states. These results offer new possibilities for quantum logic devices using a CQD system.

In Section 5-5, the interdot interaction in d = 7 nm weakly (electromagnetically) CQD was discussed. The separate excitation of two QDs constituting the CQD was achieved because of the negligible carrier transfer arising from the weak wave function coupling. The simultaneous carrier creation in two QDs (two-color excitation) induced an anomalous increment of PL intensity in the PL/PLE spectra. This observation seems to originate from the enhancement of the carrier energy relaxation caused by dipole-dipole interaction between excitons in two QDs.

In Section 5-6, we further examined the interdot interaction in a d = 7 nm weakly CQD on the basis of the second-order photon correlation spectra. We confirmed the single photon emission from each QD constituting the CQD by means of the auto photon correlation spectra. In this photon emission process, the carrier–phonon interaction is very important, and we have shown that the residual acoustic phonon enhanced the carrier energy relaxation in the photon emission process. The cross photon correlation spectrum between two QDs exhibited long-lived photon anti-bunching. This result implies the enhancement of the exciton energy relaxation caused by the interdot interaction as described in Section 5-5.

Thus, this thesis has provided findings regarding the electronic structure and interdot interaction in a CQD system using reliable samples of CQDs that were cautiously fabricated. As a remarkable finding, we showed that the quantum mechanical coupling between two QDs induced an exciton molecule. However, unfortunately, the physical properties of CQDs have not been completely

revealed. Although it is undeniable that our theoretical discussion still remains insufficient in this study, our results and discussion are considered to be able to offer some contribution to the understanding of a CQD system with a view to realize quantum information device applications.

In order to understand and extract the physical properties which enable operation of a specific device, it is indispensable to accumulate a lot of data from further systematic and interdisciplinary investigations. We look forward to the future development of research in this area.

– Acknowledgment –

The author wishes first to express his sincere gratitude to Professor Yasuaki Masumoto, Institute of Physics, University of Tsukuba, for his continuous encouragement and considerable commitment, and for giving me the opportunity to write this dissertation. The author also gratefully acknowledges helpful discussions and comments from Associate Professor Shintaro Nomura and Associate Professor Kenji Shiraishi of the Institute of Physics, University of Tsukuba, and Professor Kiyoshi Asakawa and Associate Professor Toshiaki Hattori of the Institute of Applied Physics, University of Tsukuba.

This thesis is a compilation of the studies carried out as a part of the research project named "Coherent quantum-control and information-processing technology" promoted by "Core Research for Evolutional Science and Technology (CREST)" program of Japan Science and Technology Agency (JST), for 3 years and 5 months, August 2002–December 2005. When the author joined this research project, he was given very thoughtful consideration by Administrateur Masahiro Kobayashi of Eudyna Device Co. Ltd. of the author's former affiliation. The author is greatly indebted to Adm. M. Kobayashi for his understanding and generous support of the author's work, and for enlightening suggestions and continuous encouragement. The author also wishes to appreciate Dr. Shoichi Ogita, Mr. Takashi Satsukawa and several other members of Eudyna Device for their understanding and effort on the author's research activities.

This research project was carried out at Ultrafast Optoelectronic Devices Group, Photonics Research Institute, National Institute of Advanced Industrial Science and Technology (AIST). The author would like to gratefully acknowledge Dr. Kazuhiro Komori, project leader of AIST, for giving this opportunity, and for continuous guidance, encouragement, and helpful suggestions during this work.

The author especially wishes to sincerely thank Prof. Toshihide Takagahara, Department of Electronics and Information Science, Kyoto Institute of Technology, who provided extremely meaningful discussions and critical comments about data interpretation, and kindly guided me on writing articles.

The author would like to express special gratitude to Dr. Takeyoshi Sugaya of AIST, who guided

me entirely on the MBE crystal growth technique, for patient guidance and indispensable discussions and comments during this study. The author also gratefully acknowledges helpful discussions, comments, and technical assistance from Dr. Taro Itatani, Dr. Noritsugu Yamamoto, Dr. Takeru Amano, and all other members of Ultrafast Optoelectronic Devices Group, and Dr. Mutsuo Ogura of Nanotechnology Research Institute, AIST.

The author is especially grateful to Associate Professor Noriaki Tsurumachi of Kagawa University and Associate Professor Takumi Okada of Tokai University Junior College, for their meaningful discussions, comments, and continuous encouragement.

Furthermore, this study is the result of cooperation with co-workers of the CREST project. Dr. Isao Morohashi entirely developed the surface manufacturing of samples, which was crucial for the single QD spectroscopy. The author gratefully acknowledges his substantial effort and meaningful discussions during this work. The author also gratefully appreciates Dr. Amane Shikanai, who cooperatively analyzed the experimental data, for his insightful discussions, valuable suggestions, and considerable efforts. The author wishes to thank Dr. Shigenori Furue for his thoughtful discussions, and whose interest in my work encouraged me. The author is also grateful to Mr. Keishiro Goshima for his technical assistance and cooperation.

Finally, the author wishes to express supreme thanks to his family for their continuous and tremendous support and encouragement.

山内掌吾

Shohgo YAMAUCHI

Tsukuba, February 2007

– Publication List –

– Original Articles on This Dissertation –

[1] **S. Yamauchi**, K. Komori, I. Morohashi, K. Goshima and T. Sugaya:
"Electronic Structures in Single Pair of InAs/GaAs Coupled Quantum Dots with Various Interdot Spacings"
J. Appl. Phys. **99**, 033522 (2006).

[2] **S. Yamauchi**, K. Komori and T. Sugaya:
"Optical Characteristics of Self-Aligned InAs Quantum Dots in the Presence of GaAs Oval Strain"
Jpn. J. Appl. Phys. **45**, 1030 (2006).

[3] K. Goshima, **S. Yamauchi**, K. Komori, I. Morohashi and T. Sugaya:
"Observation of Exciton Molecule Consisting of Two Different Excitons in Coupled Quantum Dots"
Appl. Phys. Lett. **87**, 253110 (2005).

[4] **S. Yamauchi**, K. Komori, I. Morohashi, K. Goshima, T. Sugaya and T. Takagahara:
"Observation of Interdot Correlation in Single Pair of Electromagnetically Coupled Quantum Dots"
Appl. Phys. Lett. **87**, 182103 (2005).

[5] **S. Yamauchi**, K. Komori, I. Morohashi, K. Goshima and T. Sugaya:
"Electronic Structures and Carrier Correlation in Single Pair of Coupled Quantum Dots"
Jpn. J. Appl. Phys. **44**, 2647 (2005).

[6] **S. Yamauchi**, K. Komori, T. Sugaya and K. Goshima:
"Optical Characteristics of InAs/GaAs Double Quantum Dots Grown by MBE with the Indium-Flush Method"
Jpn. J. Appl. Phys. **43**, 2083 (2004).

– Other Articles –

[1] T. Amano, T. Sugaya, **S. Yamauchi** and K. Komori:
"Realization of 1.3 μm InAs quantum dots with high-density, uniformity, and quality"
J. Cryst. Growth **295**, 162 (2006).

[2] T. Amano, **S. Yamauchi**, T. Sugaya and K. Komori:
"Control of subband energy levels of quantum dots using InGaAs gradient composition strain-reducing layer"
Appl. Phys. Lett. **88**, 261110 (2006).

[3] K. Goshima, K. Komori, **S. Yamauchi**, I. Morohashi, A. Shikanai and T. Sugaya:
"Pulse Area Control of the Exciton Rabi Oscillation in InAs/GaAs Single Quantum Dot"
Jpn. J. Appl. Phys. **45**, 3625 (2006).

[4] K. Goshima, K. Komori, **S. Yamauchi**, I. Morohashi, A. Shikanai and T. Sugaya:
"Observation of bonding states in single pair of coupled quantum dots using micro-spectroscopy"
Jpn. J. Appl. Phys. **44**, 2684 (2005).

[5] T. Sugaya, K. Komori, **S. Yamauchi** and T. Amano:
"1.3 um InAs quantum dots grown with an As2 source using molecular-beam epitaxy"
J. Vac. Sci. Technol. B **23**, 1243 (2005).

[6] T. Okada, K. Komori, K. Goshima, **S. Yamauchi**, I. Morohashi, T. Sugaya, O. Yamazaki, M. Ogura and T. Hattori:
"Coherent Control of Exciton in a Single Quantum Dot Using High-Resolution Michelson Interferometer"
Jpn. J. Appl. Phys. **43**, 6093 (2004).

[7] A. V. Baranov, **S. Yamauchi** and Y. Masumoto:
"Softening of the LO phonons in excited state of CuCl nanocrystals"

Journal of Luminescence **87-89**, 500 (2000).

[8] A. V. Baranov, **S. Yamauchi** and Y. Masumoto:
"Exciton--LO-phonon interaction in CuCl spherical quantum dots studied by resonant hyper-Raman spectroscopy"
Phys. Rev. B **56**, 10332 (1997).

– International Conference –

[1] **S. Yamauchi**, A. Shikanai, I. Morohashi, S. Furue, K. Komori, T. Sugaya and T. Takagahara:
"Photon Statistics in a Thick Barrier Coupled Quantum Dot"
2006 International Conference on Solid State Devices and Materials (SSDM 2006), 2006.09.

[2] K. Goshima, K. Komori, **S. Yamauchi**, I. Morohashi and T. Sugaya:
"Exciton Rabi Oscillation in InAs/GaAs Coupled Quantum Dot"
2006 International Conference on Solid State Devices and Materials (SSDM 2006), 2006.09.

[3] K. Goshima, K. Komori, **S. Yamauchi**, I. Morohashi, A. Shikanai, T. Sugaya:
"Pulse Area Control of the Exciton Rabi Oscillation in InAs/GaAs Single Quantum Dot"
2005 International Conference on Solid State Devices and Materials (SSDM 2005), 2005.09.

[4] **S. Yamauchi**, K. Komori, I. Morohashi, K. Goshima and T. Sugaya:
"Interdot Correlation in Single Pair of Coupled Quantum Dots"
International Conference on Quantum Electronics 2005 and the Pacific Rim Conference on Lasers and Electro-Optics 2005 (IQEC/CLEO-PR 2005) 2005.07.

[5] K. Goshima, K. Komori, **S. Yamauchi**, I. Morohashi and T. Sugaya:
"Measurement of Two-Qubit States Consisting of Two Different Excitons in Coupled Quantum Dots"
International Conference on Quantum Electronics 2005 and the Pacific Rim Conference on Lasers and Electro-Optics 2005 (IQEC/CLEO-PR 2005) 2005.07.

[6] I. Morohashi, **S. Yamauchi**, A. Shikanai, K. Goshima, T. Sugaya, N. Yamamoto and K. Komori:
"Electric field Dependence of Photoluminescence in Coupled Quantum Dots"
International Symposium on Quantum Dots and Photonic Crystals 2005 (ISQDPC2005), 2005.03.

[7] T. Sugaya, K. Komori, **S. Yamauchi** and T. Amano:
"1.3 μm InAs Quantum Dots Grown with an As2 Source using Molecular Beam Epitaxy"
North American Conference on Molecular Beam Epitaxy (NAMBE 2004), 2004.10.

[8] **S. Yamauchi**, K. Komori, T. Sugaya, I. Morohashi and K. Goshima:
"Carrier correlation in single pair of coupled quantum dots"
2004 International Conference on Solid State Devices and Materials (SSDM 2004), 2004.09.

[9] K. Goshima, K. Komori, **S. Yamauchi**, I. Morohashi, A. Shikanai and T. Sugaya:
"Observation of bonding states in single pair of coupled quantum dots using Micro-spectroscopy"
2004 International Conference on Solid State Devices and Materials (SSDM 2004), 2004.09.

[10] **S. Yamauchi**, K. Komori, T. Sugaya and K. Goshima:
"Optical characteristics of InAs/GaAs double quantum dots grown by MBE with Indium-Flush method"
2003 International Conference on Solid State Devices and Materials (SSDM 2003), 2003.09.

[11] T. Okada, K. Komori, K. Goshima, **S. Yamauchi**, T. Sugaya, O. Yamazaki and T. Hattori:
"Coherent control of exciton in a single quantum dot using a high-resolution Michelson interferometer"
2003 International Conference on Solid State Devices and Materials (SSDM 2003), 2003.09.

– References –

[1] X. Wang, J. Zhuang, Q. Peng and Y. Li: Nature **437**, 121 (2005).

[2] 小泉光恵, 奥山喜久夫, 目義雄(編): ナノ粒子の製造・評価・応用・機器の最新技術 (シーエムシー出版, 2002).

[3] A. D. Yoffe: Adv. Phys. Vol. **42**, No. 2, 173 (1993).

[4] D. Bimberg, M. Grundmann and N. N. Ledentsov: *Quantum Dot Heterostructures* (John Wiley, New York, 1999).

[5] Y. Masumoto and T. Takagahara (Eds.): *Semiconductor Quantum Dots* (Springer, Berlin, 2002).

[6] A. I. Ekimov and A. A. Onushchenko: JETP Lett. **34**, 345 (1981).

[7] Y. Arakawa and H. Sakaki: Appl. Phys. Lett. **40**, 939 (1982).

[8] M. Asada, Y. Miyamoto and Y. Suematsu: IEEE J. Quantum Electron. **22**, 1915 (1986).

[9] L. Goldstein, F. Glas, J. Y. Marzin, M. N. Charasse and G. Le Roux: Appl. Phys. Lett. **47**, 1099 (1985).

[10] K. Otsubo, N. Hatori, M. Ishida, S. Okumura, T. Akiyama, Y. Nakata, H. Ebe, M. Sugawara and Y. Arakawa: Jpn. J. Appl. Phys. **43**, L1124 (2004).

[11] M Sugawara, N Hatori, M Ishida, H Ebe, Y Arakawa, T Akiyama, K Otsubo, T Yamamoto and Y Nakata: J. Phys. D **38**, 2126 (2005).

[12] 細谷暁夫: 量子コンピュータの基礎 (サイエンス社, 1999).

[13] M. A. Nielsen and I. L. Chuang: *Quantum Computation and Quantum Information* (CambridgeUniversity Press, Cambridge, 2000).

[14] D. A. Bonn, J. C. Wynn, B. W. Gardner, Y. Lin, R. Liang, W. N. Hardy, J. R. Kirtley and K. A. Moler: Nature **414**, 887 (2001).

[15] E. Waks, A. Zeevi and Y. Yamamoto: Phys. Rev. A **65**, 052310 (2002).

[16] D. Bouwmeester, J.-W. Pan, K. Mattle, M. Eibl, H. Weinfurter and A. Zeilinger: Nature **390**, 575 (1997).

[17] A. Barenco, D. Deutsch and A. Ekert: Phys. Rev. Lett. **74**, 4083 (1995).

[18] 羽田野剛司, 樽茶清悟: 応用物理 **74**, 0313 (2005).

[19] 山本喜久: 応用物理 **72**, 0146 (2003).

[20] Peter Michler (Ed.): *Single Quantum Dots* (Springer, Berlin, 2003).

[21] P. Borri, W. Langbein, S. Schneider, U. Woggon, R. L. Sellin, D. Ouyang and D. Bimberg: Phys. Rev. Lett. **87**, 157401 (2001).

[22] N. H. Bonadeo, J. Erland, D. Gammon, D. Park, D. S. Katzer and D. G. Steel: Science **282**, 1473 (1998).

[23] Y. Toda, T. Sugimoto, M. Nishioka and Y. Arakawa: Appl. Phys. Lett. **76**, 3887 (2000).

[24] T. H. Stievater, Xiaoqin Li, D. G. Steel, D. Gammon, D. S. Katzer, D. Park, C. Piermarocchi and L. J. Sham: Phys. Rev. Lett. **87**, 133603 (2001).

[25] H. Htoon, T. Takagahara, D. Kulik, O. Baklenov, A. L. Holmes, Jr. and C. K. Shih: Phys. Rev. Lett. **88**, 087401 (2002).

[26] A. Zrenner, E. Beham, S. Stufler, F. Findeis, M. Bichler and G. Abstreiter: Nature **418**, 612 (2002).

[27] L. Besombes, J. J. Baumberg and J. Motohisa: Phys. Rev. Lett. **90**, 257402 (2003).

[28] A. Muller, Q. Q. Wang, P. Bianucci, C. K. Shih and Q. K. Xue: Appl. Phys. Lett. **84**, 981 (2004).

[29] T. Unold, K. Mueller, C. Lienau, T. Elsaesser and A. D. Wieck: Phys. Rev. Lett. **94**, 137404 (2005).

[30] H. Kamada, H. Gotoh, J. Temmyo, T. Takagahara and H. Ando: Phys. Rev. Lett. **87**, 246401 (2001).

[31] X. Li, Y. Wu, D. Steel, D. Gammon, T. H. Stievater, D. S. Katzer, D. Park, C. Piermarocchi and L. J. Sham: Science **301**, 809 (2003).

[32] C. Santori, M. Pelton, G. Solomon, Y. Dale and Y. Yamamoto: Phys. Rev. Lett. **86**, 1502 (2001).

[33] E. Moreau, I. Robert, L. Manin, V. Thierry-Mieg, J. M. Gérard and I. Abram: Phys. Rev. Lett. 87,

183601 (2001).
[34] D. Fattal, K. Inoue, J. Vukovi, C. Santori, G. S. Solomon and Y. Yamamoto: Phys. Rev. Lett. **92**, 037903 (2004).
[35] K. Takemoto, Y. Sakuma1, S. Hirose, T. Usuki, N. Yokoyama, T. Miyazawa, M. Takatsu and Y. Arakawa: Jpn. J. Appl. Phys. **43**, L993 (2004).
[36] E. Biolatti, R. C. Iotti1, P. Zanardi and F. Ro: Phys. Rev. Lett. **85**, 5647 (2000).
[37] J. M. Villas-Bôas, A. O. Govorov and S. E. Ulloa: Phys. Rev. B **69**, 125342 (2004).
[38] H. J. Krenner, M. Sabathil, E. C. Clark, A. Kress, D. Schuh, M. Bichler, G. Abstreiter and J. J. Finley: Phys. Rev. Lett. **94**, 057402 (2005).
[39] 清水清孝: 量子力学Ⅱ (産業図書, 1996) p.66.
[40] LANDOLT-BÖRNSTEIN, *Numerical Data and Functional Relationships in Science and Technology* Vol.**17**, Semiconductors (Springer, Berlin, 1982).
[41] M. Grundmann, O. Stier and D. Bimberg: Phys. Rev. B **52**, 11969 (1995).
[42] M. Korkusiński and P. Hawrylak: Phys. Rev. B **63**, 195311 (2001).
[43] O. Stier, M. Grundmann and D. Bimberg: Phys. Rev. B **59**, 5688 (1999).
[44] W. Sheng and J.-P. Leburton: Phys. Rev. Lett. **88**, 167401 (2002).
[45] A. J. Williamson, L. W. Wang and A. Zunger: Phys. Rev. B **62**, 12963 (2000).
[46] G. Bester, S. Nair and A. Zunger: Phys. Rev. B **67**, 161306 (2003).
[47] G. Bester, A. Zunger and J. Shumway: Phys. Rev. B **71**, 075325 (2005).
[48] M. Grundmann, N. N. Ledentsov, O. Stier, D. Bimberg, V. M. Ustinov, P. S. Kop'ev and Zh. I. Alferov: Appl. Phys. Lett. **68**, 979 (1996).
[49] M. Ono, K. Matsuda, T. Saiki, K. Nishi, T. Mukaiyama and M. Kuwata-Gonokami: Jpn. J. Appl. Phys. **38,** L1460 (1999).
[50] M. Bayer, O. Stern, P. Hawrylak, S. Fafardand and A. Forchel: Nature **405**, 923 (2000).
[51] S. Sauvage, P. Boucaud, F. H. Julien, J.-M. Gérard and J.-Y. Marzin: Appl. Phys. Lett. **82**, 3396 (1997).
[52] N. Horiguchi, T. Futatsugi, Y. Nakata, N. Yokoyama, T. Mankad and P. M. Petroff: Jpn. J. Appl. Phys. **38**, 2559 (1999).
[53] R. J. Warburton, C. S. Dürr, K. Karrai, J. P. Kotthaus, G. Medeiros-Ribeiro and P. M. Petroff: Phys. Rev. Lett. **79**, 5282 (1997).
[54] E. Dekel1, D. Gershoni, E. Ehrenfreund, D. Spektor, J. M. Garcia and P. M. Petroff: Phys. Rev. Lett. **80**, 4991 (1998).
[55] J. J. Finley, A. D. Ashmore, A. Lemaître, D. J. Mowbray, M. S. Skolnick, I. E. Itskevich, P. A. Maksym, M. Hopkinson and T. F. Krauss: Phys. Rev. B **63**, 073307 (2001).
[56] M. Lomascolo, A. Vergine, T. K. Johal, R. Rinaldi, A. Passaseo, R. Cingolani, S. Patanè, M. Labardi, M. Allegrini, F. Troiani and E. Molinari: Phys. Rev. B **66**, 041302 (2002).
[57] T. Amano, S. Yamauchi, T. Sugaya and K. Komori: Appl. Phys. Lett. **88**, 261110 (2006).
[58] 小林考次郎: 計算の複雑さ, ソフトウエア講座 **33** (昭晃堂, 1988).
[59] P.W.Shor: Proceedings of the 35th Annual Symposium on the Foundations of Computer Science, 124 (1994).
[60] D. Deutsch, A. Barenco and A. Eckert: Proc. Roy. Soc. London Ser.A **474**, 969 (1995).
[61] A. Barenco, C. H. Bennett, R. Cleve, D. P. DiVincenzo, N. Margolus, P. Shor, T. Sleator, J. A. Smolin and H. Weinfurter: Phys. Rev. A **52**, 3457 (1995).
[62] C. Monroe, D. M. Meekhof, B. E. King, W. M. Itano and D. J. Wineland: Phys. Rev. Lett. **75**, 4714 (1995).
[63] J. I. Cirac and P. Zoller: Phys. Rev. Lett. **74**, 4091 (1995).
[64] I. L. Chuang, L. M. K. Vandersypen, X. Zhou, D. W. Leung and S. Lloyd: Nature **393**, 143 (1998).
[65] T. D. Ladd, J. R. Goldman, F. Yamaguchi, Y. Yamamoto, E. Abe and K. M. Itoh: Phys. Rev. Lett. **89**, 017901 (2002).
[66] T. Yamamoto, Yu. A. Pashkin, O. Astafiev, Y. Nakamura and J. S. Tsai: Nature **425**, 941 (2003).
[67] S. Saito, M. Thorwart, H. Tanaka, M. Ueda, H. Nakano, K. Semba and H. Takayanagi: Phys. Rev. Lett. **93**, 037001 (2004).
[68] T. H. Oosterkamp, T. Fujisawa, W. G. Vanderwiel, K. Ishibashi, R. V. Hijman, S. Tarucha and L. P.

Kouwenhoven: Nature **395**, 873 (1998).
[69] T. Fujisawa, D. G. Austing, Y. Tokura, Y. Hirayama and S. Tarucha: Nature **419**, 278 (2002).
[70] T. Ota, K. Ono, M. Stopa, T. Hatano, S. Tarucha, H. Z. Song, Y. Nakata, T. Miyazawa, T. Ohshima and N. Yokoyama: Phys. Rev. Lett. **93**, 066801 (2004).
[71] T. Hatano, M. Stopa, T. Yamaguchi, T. Ota, K. Yamada and S. Tarucha: Phys. Rev. Lett. **93**, 066806 (2004).
[72] M. Ikezawa, B. Pal Y. Masumoto, I. V. Ignatiev, S. Yu. Verbin and I. Ya. Gerlovin: Phys. Rev. B **72**, 153302 (2005).
[73] 霜田光一: レーザー物理入門 (岩波書店, 1983)
[74] I. Shtrichman, C. Metzner, B. D. Gerardot, W. V. Schoenfeld and P. M. Petroff: Phys. Rev. B **65**, 081303 (2002).
[75] G. Ortner, M. Bayer, Y. Lyanda-Geller, T. L. Reinecke, A. Kress, J. P. Reithmaier and A. Forchel: Phys. Rev. Lett. **94**, 157401 (2005).
[76] Toshio Ohshima: Phys. Rev. A **62**, 062316 (2000).
[77] 古澤明: 応用物理 **72**, 0157 (2003).
[78] OPTRONICS No.285 (オプトロニクス社, 2005).
[79] O.Hirota, M.Sohma, M.Fuse and K.Kato: Phys. Rev. A **72**, 022335, (2005).
[80] 広田修: 電子情報通信学会、論文誌 B, No-4, 478 (2004).
[81] P. G. Kwiat, K. Mattle, H. Weinfurter A. Zeilinger, A. V. Sergienko and Y. Shih: Phys. Rev. Lett. **75**, 4337 (1995).
[82] 松岡正浩: 量子光学 (裳華房, 2000).
[83] V. Zwiller, P. Jonsson, H. Blom, S. Jeppesen, M-E. Pistol, L. Samuelson, A. A. Katznelson, E. Yu. Kotelnikov, V. Evtikhiev and G. Björk: Phys. Rev. A **66**, 053814 (2002).
[84] A. Kiraz, S. Fälth, C. Becher, B. Gayral, W. V. Schoenfeld, P. M. Petroff, Lidong Zhang, E. Hu and A. Imamoğlu: Phys. Rev. B **65**, 161303 (2002).
[85] B. D. Gerardot, S. Strauf, M. J. A. de Dood, A. M. Bychkov, A. Badolato, K. Hennessy, E. L. Hu, D. Bouwmeester and P. M. Petroff: Phys. Rev. Lett. **95**, 137403 (2005).
[86] R. M. Stevenson, R. J. Young, P. Atkinson, K. Cooper, D. A. Ritchie and A. J. Shields: Nature **439**, 179 (2006).
[87] A. Hartmann, Y. Ducommun, E. Kapon, U. Hohenester and E. Molinari: Phys. Rev. Lett. **84**, 5648 (2000).
[88] 宮崎栄三編: 表面科学の基礎と応用, p.423 (フジテクノシステム, 1991).
[89] R. Heitz, T. R. Ramachandran, A. Kalburge, Q. Xie, I. Mukhametzhanov, P. Chen and A. Madhukar: Phys. Rev. Lett. **78**, 4071 (1997).
[90] 権田俊一: 分子線エピタキシー (培風館, 1994).
[91] 尾関雅志, 清水雄一郎: 応用物理 **72**, 1248 (2003).
[92] K. Nishi, H. Saito, S. Sugou and J.-S. Lee: Appl. Phys. Lett. **74**, 1111 (1999).
[93] L. Seravalli, P. Frigeri, M. Minelli, P. Allegri, V. Avanzini and S. Franchi: Appl. Phys. Lett. **87**, 063101 (2005)
[94] S. Raymond, X. Guo, J. L. Merz and S. Fafard: Phys. Rev. B **59**, 7624 (1999).
[95] D. S. L. Mui, D. Leonard, L. A. Coldren and P. M. Petroff: Appl. Phys. Lett. **66**, 1620 (1995).
[96] Y. Nakamura, O. G. Schmidt, N. Y. Jin-Phillipp, S. Kiravittaya, C. Müller, K. Eberl, H. Gräbeldinger and H. Schweizer: J. Cryst. Growth **242**, 339 (2002).
[97] M. Kitamura, M. Nishioka, J. Oshinowo and Y. Arakawa: Appl. Phys. Lett. **66**, 3663 (1995).
[98] K. Häusler, K. Eberl, F. Noll and A. Trampert: Phys. Rev. B **54**, 4913 (1996).
[99] S. Ohkouchi , Y. Nakamura , H. Nakamura and K. Asakawa: Physica E **21**, 597 (2004).
[100] J. Kasai and M. Kawata: Appl. Phys. Lett. **73**, 2012 (1995).
[101] L. Landin, M. Pistol, C. Pryor, M. Persson, L. Samuelson and M. Miller: Phys. Rev. B **60**, 16640 (1999).
[102] A. Lemaître, A. D. Ashmore, J. J. Finley, D. J. Mowbray, M. S. Skolnick, M. Hopkinson and T. F. Krauss: Phys. Rev. B **63**, 161309 (2001).
[103] S. Farfad, R. Leon, D. Leonard, J. L. Merz and P. M. Petroff: Phys. Rev. B **52**, 5752 (1995).

[104] Q. Xie, A. Madhukar, P. Chen and N. P. Kobayashi: Phys. Rev. Lett. **75**, 2542 (1995).
[105] F. Heinrichsdorff, A. Krost, D. Bimberg, A. O. Kosogov and P. Werner: Appl. Surf. Sci. **123/124**, 725 (1998).
[106] Z. R. Wasilewski, S. Fafard and J. P. McCaffrey: J. Crystal Growth **201/202**, 1131 (1999).
[107] G. J. Beirne, C. Hermannstädter, L. Wang, A. Rastelli, O. G. Schmidt and P. Michler: Phys. Rev. Lett. **96**, 137401 (2006).
[108] W. Sheng and J. P. Leburton: Phys. Rev. B **63**, 161301 (2001).
[109] A. Tackeuchi, T. Kuroda, K. Mase, Y. Nakata and N. Yokoyama: Phys. Rev. B **62**, 1568 (2000).
[110] S. Sauvage, P. Boucaud, F. H. Julien, J.-M. Ge´rard and J.-Y. Marzin: J. Appl. Phys. **82**, 3396 (1997).
[111] Yu. I. Mazur, Zh. M. Wang, G. G. Tarasov, Min Xiao, G. J. Salamo, J. W. Tomm, V. Talalaev and H. Kissel: Appl. Phys. Lett. **86**, 063102 (2005).
[112] S. Muto, T. Inata, A. Tackeuchi, Y. Sugiyama and T. Fujii: Appl. Phys. Lett. **58**, 2393 (1991).
[113] S. Hameau, Y. Guldner, O. Verzelen, R. Ferreira, G. Bastard, J. Zeman, A. Lemaıˆtre and J. M. Ge´rard: Phys. Rev. Lett. **83**, 4152 (1999).
[114] R. Heitz, I. Mukhametzhanov, O. Stier, A. Madhukar and D. Bimberg: Phys. Rev. Lett. **83**, 4654 (1999).
[115] T. Inoshita and H. Sakaki: Phys. Rev. B **46**, 7260 (1992).
[116] P. Borri, W. Langbein, J. M. Hvam and F. Martelli: Phys. Rev. B **59**, 2215 (1999).
[117] M. Bayer, P. Hawrylak, K. Hinzer, S. Fafard, M. Korkusinski, Z. R. Wasilewski, O. Stern and A. Forchel: Science **291**, 451 (2001).
[118] G. Ortner, M. Bayer, A. Larionov, V. B. Timofeev, A. Forchel, Y. B. Lyanda-Geller, T. L. Reinecke, P. Hawrylak, S. Fafard and Z. Wasilewski: Phys. Rev. Lett. **90**, 086404 (2003).
[119] X. Xu, D. A. Williams and J. R. A. Cleaver: Appl. Phys. Lett. **86**, 012103 (2005).
[120] G. Ortner, I. Yugova, G. Baldassarri Höger von Högersthal, A. Larionov, H. Kurtze, D. R. Yakovlev, M. Bayer, S. Fafard, Z. Wasilewski, P. Hawrylak, Y. B. Lyanda-Geller, T. L. Reinecke, A. Babinski, M. Potemski, V. B. Timofeev and A. Forchel: Phys. Rev. B **71**, 125335 (2005).
[121] See, for example, J. J. Finley, P. W. Fry, A. D. Ashmore, A. Lemaître, A. I. Tartakovskii, R. Oulton, D. J. Mowbray, M. S. Skolnick, M. Hopkinson, P. D. Buckle and P. A. Maksym: Phys. Rev. B **63**, 161305 (2001); M. Baier, F. Findeis, A. Zrenner, M. Bichler and G. Abstreiter: Phys. Rev. B **64**, 195326 (2001); M. Ediger, P. A. Dalgarno, J. M. Smith, B. D. Gerardot, and R. J. Warburton, K. Karrai and P. M. Petroff: Appl. Phys. Lett. **86**, 211909 (2005).
[122] A. S. Bracker, E. A. Stinaff, D. Gammon, M. E. Ware, J. G. Tischler, A. Shabaev, Al. L. Efros, D. Park, D. Gershoni, V. L. Korenev and I. A. Merkulov: Phys. Rev. Lett. **94**, 047402 (2005).
[123] S. Cortez, O. Krebs, S. Laurent, M. Senes, X. Marie, P. Voisin, R. Ferreira, G. Bastard, J-M. Gérard and T. Amand: Phys. Rev. Lett. **89**, 207401 (2002).
[124] T. Takagahara: Phys. Rev. B **62**, 16840 (2000).
[125] C. E. Pryor and M. E. Flatté: Phys. Rev. Lett. **91**, 257901 (2003).
[126] M. Bayer, G. Ortner, O. Stern, A. Kuther, A. A. Gorbunov, A. Forchel, P. Hawrylak, S. Fafard, K. Hinzer, T. L. Reinecke, S. N. Walck, J. P. Reithmaier, F. Klopf and F. Schäfer: Phys. Rev. B **65**, 195315 (2002).
[127] B. Urbaszek, R. J. Warburton, K. Karrai, B. D. Gerardot, P. M. Petroff and J. M. Garcia: Phys. Rev. Lett. **90**, 247403 (2003).
[128] H. Htoon, D. Kulik, O. Baklenov, A. L. Holmes, Jr., T. Takagahara and C. K. Shih: Phys. Rev. B **63**, 241303 (2001).
[129] H. Gotoh, H. Kamada, T. Saitoh, H. Ando and J. Temmyo: Phys. Rev. B **71**, 195334 (2005).
[130] Y. Kayanuma and K. Kuroda: Appl. Phys. A **53**, 475 (1991).
[131] D. L. Dexter: J. Chem. Phys. **21**, 836 (1953).
[132] T. Förster: Ann. Phys. **2**, 55 (1948).
[133] 花村榮一: 量子光学 (岩波書店, 1992).
[134] R. H. Dicke: Phys. Rev. **93**, 99 (1954).
[135] T. Itoh, M. Furumiya and T. IkeharaC. Gourdon: Solid State Commun. **73**, 271 (1990).
[136] 長澤信方(編): レーザー光学物性 (丸善, 1993).

[137] I.I. Novikov, N Yu Gordeev, M.V. Maximov, Yu M. Shernyakov, A.E. Zhukov, A.P. Vasil'ev, E.S. Semenova, V.M. Ustinov, N.N. Ledentsov, D. Bimberg, N.D. Zakharov and P. Werner: Semicond. Sci. Technol. **20**, 33 (2005).
[138] M. Gurioli, A. Vinattieri, M. Colocci, C. Deparis, J. Massies, G. Neu, A. Bosacchi and S. Franchi: Phys. Rev. B **44**, 3115 (1991).
[139] 松岡正浩: 量子光学 (東京大学出版会, 1996).
[140] R. Hanbury Brown and R. Q. Twiss: Nature **177**, 27 (1956).
[141] See for example, C. Kittel: *Introduction to Solid State Physics*, 7th ed. (wiley, New York, 1996); S. D. Lambade and G. G. Sahasrabudhe: J. Acoust. Soc. Am. **105**, 2085 (1999).
[142] T. C. Cetas, C. R. Tilford and C. A. Swenson: Phys. Rev. **174**, 835 (1968).